Railway wheel defect identification

Alemi, Alireza

DOI
10.4233/uuid:981edd2c-1674-4cba-8146-cf097b29c4f1

Publication date
2019

Document Version
Final published version

Citation (APA)
Alemi, A. (2019). *Railway wheel defect identification*. [Dissertation (TU Delft), Delft University of Technology]. https://doi.org/10.4233/uuid:981edd2c-1674-4cba-8146-cf097b29c4f1

RAILWAY WHEEL DEFECT IDENTIFICATION

RAILWAY WHEEL DEFECT IDENTIFICATION

Dissertation

for the purpose of obtaining the degree of doctor
at Delft University of Technology
by the authority of the Rector Magnificus, Prof.dr.ir. T.H.J.J. van der Hagen
chair of the Board for Doctorates
to be defended publicly on
Tuesday 22 January 2019 at 15:00 hours

by

Alireza ALEMI

Master of Science in Mechanical Engineering,
Imam Hossein University, Tehran, Iran
born in Damghan, Iran

This dissertation has been approved by the:

Promotor: Prof. dr. ir. G. Lodewijks
Copromotor: Dr. ir. Y. Pang

Composition of the doctoral committee:

Rector Magnificus,	Chairman
Prof. dr. ir. G. Lodewijks,	Delft University of Technology, promotor
Dr. ir. Y. Pang	Delft University of Technology, copromotor
Independent members:	
Prof. dr. J. Nielsen	Chalmers University of Technology, Sweden
Prof. dr. S. Dong	University of Science and Technology Beijing, China
Prof. dr. ir. R.P.B.J. Dollevoet	Delft University of Technology
Prof. dr. ir. R. Benedictus	Delft University of Technology
Other member:	
Prof. dr. F. Corman	ETH Zürich, Switzerland

This thesis was partially supported by Ministry of Science, Research and Technology (MSRT), I.R. IRAN.

ISBN 978-94-6384-010-1

An electronic version of this dissertation is available at
`http://repository.tudelft.nl/`

Printed in the Netherlands.

Dedicated to my uncles,
Ahmad, and MohammadReza Alemi,
who I never seen them...
(Martyred in Iran's Holy Defence)

To my lovely wife,
Madiheh

CONTENTS

SUMMARY

Wheels are critical components of trains, and their conditions should be therefore monitored. Wheel defects change the wheel-rail contact and cause high impact forces that are damaging for tracks and trains. Wheel defects can also cause unexpected failures that reduce the availability and reliability of the railway system. Several monitoring systems have been developed to detect and identify the wheel defects. Wheel Impact Load Detector (WILD) is commonly used to estimate the wheel condition by measuring the wheel-rail contact force.

WILDs normally measure the contact force by multiple sensors in different locations to sample from different portions of the wheel circumference. The variation in the forces measured by the multiple sensors presents the condition of the wheel. Force ratio and dynamic force are two main indicators using for detecting the defective wheels. Force ratio is the division of the peak force by the average force and the dynamic force is the subtraction of the peak force and the average force. Force ratio and dynamic force are influenced by axle load, and train velocity. In addition, these criteria fail to identify the defect types. Furthermore, these methods are not useful for monitoring the minor defects.

This thesis aims to develop a monitoring system to accurately estimate the wheel condition by detecting and identifying its defects. To achieve this purpose, this research focuses on strain-base WILDs as the widespread systems and develops required data analysis methods. WILDs usually measure the contact force by multiple sensors in discrete locations. This type of measurement just provides the magnitude of the samples and misses the pattern of the contact force. Therefore, this thesis explains the configuration of the sensors and the corresponding issue of the partial observation and proposes a fusion method to fuse the data collected by the multiple sensors. By associating the samples with their positions over the circumferential coordinate in the space domain, a new informative signal is reconstructed that represents the wheel geometry and consequently the wheel defect.

The reconstructed defect signal is influenced by different parameters such as train velocity, axle load, number of sensors, and wheel diameter. This thesis investigates the influence of these parameters by carrying out a comprehensive parametric study. To achieve this purpose, VI-Rail as a multi-body dynamics software is used to simulate the wheel-rail interaction and provide required data. Then, the developed fusion method is exploited to reconstruct defect signal from the simulated data. This study provides a detailed insight about the effects of the influential parameters by investigating the variation of the reconstructed defect signals.

The next step is identifying the wheel defect to estimate the wheel condition by attributing the reconstructed signal to the wheel defect. The influential parameters can be categorized into two groups. In the first group, the parameters influence the fusion process, and make an imperfect measurement and corrupt the signals reconstructed. Mea-

surement noise, lack of enough number of sensors, and error in estimating the wheel diameter can be mentioned as the parameters of the first group. In the second group, the operational parameters such as the train velocity, and axle load change the signals reconstructed. Variations in the second group parameters lead to variation in the signals reconstructed even when the defect is kept constant and the fusion process works perfectly. In spite of having perfect reconstruction, the variation in the operational parameters is unavoidable. This thesis tackles the challenge of variation in the signals to attribute the reconstructed signals to the defects. To achieve this purpose, the supervised pattern recognition methods are used to design the required classifiers to deal with this classification problem. As a result, a defect identification model is developed to estimate the defect type and severity by classifying the defective wheels.

In the previous parts, the fusion model and the defect identification model used the simulated data to generate the dataset and test the model. Hence, this thesis validates the defect identification model using the data generated by laboratory tests. Due to the lack of experimental facility, a new test rig is designed and constructed to model the wheel-rail interaction and to generate the real data required for the data fusion and the defect identification model. In this test rig, a rotating arm moves a wheel over a circular rail that is supported by sleepers. Then, six strain sensors are mounted under the rail with constant intervals to measure the rail bending strain. The strain sensors measure different portions of the wheel in discrete points. The fusion model reconstructs patterns from the data collected by the multiple strain sensors for different wheel defects. By reconstructing the informative patterns correlated to the wheel defects, the fusion model is validated. The results obtained present a great potential for further real field application by classifying the defects into different classes of types and severities with less than 5 % errors.

SAMENVATTING

Omdat wielen cruciale treinonderdelen zijn moet hun conditie in de gaten gehouden worden. Defecten aan wielen veranderen het contact tussen wiel en rail en veroorzaken grote slagkrachten die schadelijk zijn voor het spoor en treinen. Wielbeschadigingen kunnen ook onverwachte storingen veroorzaken die de beschikbaarheid en betrouwbaarheid van het spoorwegnet verminderen. Er zijn verscheidene controlesystemen ontwikkeld om wielgebreken te ontdekken en te onderscheiden. Vaak wordt een wielkrachtbelastingsdetector (Wheel Impact Load Detector, WILD) gebruikt om de conditie van een wiel te beoordelen; dit measurement de contactkracht tussen wiel en rail.

WILDs meten deze contactkracht normaal gesproken met meerdere sensoren op verschillende locaties om de wielomtrek steekproefsgewijs te kunnen onderzoeken. De variatie in de gemeten krachten zegt iets over de conditie van het wiel. Twee hoofdindicatoren voor het ontdekken van gebreken bij wielen zijn de krachtverhouding en de dynamische kracht. De krachtverhouding is het quotiënt van de piekkracht en de gemiddelde kracht; de dynamische kracht is het verschil van de piekkracht en de gemiddelde kracht. De krachtverhouding en de dynamische kracht worden echter beïnvloed door de asbelasting en de snelheid van de trein. Ook kunnen deze indicatoren de soort beschadiging niet vaststellen. Bovendien zijn deze methodes niet bruikbaar om kleine beschadigingen op te sporen.

Het doel in dit proefschrift is een inspectiesysteem te ontwikkelen dat de wielconditie precies bepaalt door gebreken te herkennen en te identificeren. Om dit te bereiken ontwikkelt dit onderzoek de benodigde data-analysemethoden voor de veelgebruikte op vervorming gebaseerde WILDs. WILDs meten de contactkrachten gewoonlijk met meerdere sensoren op afzonderlijke locaties. Dit type meting geeft alleen de grootte van de krachten maar mist het patroon van de contactkracht. Dit proefschrift beschouwt daarom de opstelling van de sensoren en het daaruit voortvloeiende probleem van gedeeltelijke observatie en stelt een methode voor om de data van de afzonderlijke sensoren te combineren. Door de metingen te combineren met hun positie op de cirkelomtrekcoördinaat in het ruimtedomein wordt een nieuw informatief signaal gereconstrueerd dat de geometrie van het wiel, en zodoende de beschadigingen aan het wiel, representeert.

Het gereconstrueerde beschadigingsprofiel wordt beïnvloed door verschillende parameters, waaronder treinsnelheid, asbelasting, het aantal sensoren en de diameter van het wiel. Dit proefschrift onderzoekt de invloed van deze parameters door een uitgebreid parameteronderzoek uit te voeren. Hiertoe wordt de multilichaamsdynamicasoftware VI-Rail gebruikt om de interactie tussen wiel en rail te simuleren en te zorgen voor de benodigde data. De ontwikkelde combinatiemethode wordt vervolgens gebruikt om het beschadigingsprofiel uit de gesimuleerde data te reconstrueren. Door de variatie van de gereconstrueerde beschadigingsprofielen te onderzoeken geeft deze studie een gedetailleerd inzicht in de effecten van de relevante parameters.

De volgende stap in het bepalen van de wielconditie is het identificeren van het wielgebrek op basis van het gereconstrueerde signaal. De beïnvloedende parameters kunnen in twee groepen worden ingedeeld. De parameters in de eerste groep beïnvloeden het combinatieproces; ze zorgen voor imperfecte metingen en verstoren het gereconstrueerde signaal. Meetruis, een tekort aan sensoren en fouten in het bepalen van de wieldiameter zijn parameters van deze eerste groep. De tweede groep bestaat uit operationele parameters, zoals treinsnelheid en asbelasting, die de gereconstrueerde signalen veranderen. Variaties in parameterwaarden van de tweede groep leiden tot variaties in het gereconstrueerde signaal, ook als het mankement constant is en het combinatieproces perfect werkt. Zelfs bij men een perfecte reconstructie is, de variatie in operationele parameters onvermijdelijk. Dit proefschrift pakt het probleem van variatie in de signalen aan om de gereconstrueerde signalen aan de typen gebreken te kunnen koppelen. Voor dit classificatieprobleem worden geleide patroonherkenningsmethodes gebruikt om de benodigde classificatiefuncties te ontwerpen. Dit resulteert in een model om het type en de intensiteit van het mankement te bepalen door het classificeren van de beschadigde wielen.

Het hiervoor beschreven combinatiemodel en identificatiemodel gebruikt gesimuleerde data om een dataset te genereren en het model te testen. Dit proefschrift valideert het beschadigingsidentificatiemodel op basis van data die gegenereerd zijn door laboratoriumtests. Vanwege het ontbreken van een testinrichting wordt een nieuwe testopstelling ontworpen en geconstrueerd om de wiel-railinteractie te boetseren en realistische data te genereren die nodig zijn voor het combinatie- en identificatiemodel. In deze testopstelling beweegt een roterende arm een wiel over een cirkelvormige rail op bielzen. Zes belastingssensoren zijn op regelmatige afstanden onder de rail vastgemaakt om de buigspanning te meten. De sensoren meten verschillende delen van het wiel op afzonderlijke punten. Het combinatiemodel reconstrueert, voor verschillende wielbeschadigingen, patronen uit de data die door de afzonderlijke sensoren verzameld zijn. Door de informatieve patronen, gecorreleerd aan de wielgebreken, te reconstrueren wordt het combinatiemodel gevalideerd. De resultaten laten zien dat classificeren van de gebreken in verschillende types en verschillende mates van intensiteit met minder dan 5% fouten mogelijk is, waardoor de methode zeer geschikt is voor verdere daadwerkelijke toepassing.

1

INTRODUCTION

1.1. BACKGROUND

Wheels are critical components of trains, which deteriorate over time due to wear and fatigue. Wheel defects such as corrugation, flat, spalling and shelling [1] change the contact feature between wheel and rails, and may generate a high impact force. From the safety point of view, the defects of wheelsets are the main reasons of train accidents [2]. In addition, high impact forces are detrimental to the track and train and increase the maintenance cost. Unexpected wheel failures also reduce the availability of trains and cause delay in the transport services that reduces the reliability of the railway system. Hence, the maintenance of the wheels is a vital task.

The maintenance policies can be generally classified into corrective and preventive [3]. Corrective maintenance (breakdown or run to failure maintenance) has been a common policy operated on the wheels. A wheel failure means a severe defect that has an impact force that exceeds a predetermined threshold (e.g., 290 kN in Sweden [4] and 400.3 kN in the US [5]). Furthermore, the wheel maintenance involves a re-profiling procedure by machining the tyre thickness to return the profile feature. This procedure decreases the wheel diameter to the limit where the wheel is not repairable any more and has to be replaced. For example in the Netherlands, before 2007, NedTrain, the Dutch railway maintenance company, re-profiled the wheels 5 to 6 times over their lifetime. In that period, the wheel defects were detected by visual inspections or by a condition monitoring system due to their high impact forces [6].

A preventive policy aims to avoid failure of a component by estimating its condition and doing the maintenance activities in the right time [3]. To make an effective and efficient maintenance plan, the condition of the wheels should be accurately measured or estimated. Physical and statistical modelling are two approaches to estimate the condition before the operation [3]. A physical model describes the failure mechanism using a numerical or analytical method. A statistical model represents the failure distribution based on the historical data to use for similar systems.

Currently, some maintenance companies such as NedTrain are following a usage-based preventive policy. According to this policy, the trains are sent to workshops when

approaching a predetermined threshold of usage in time or mileage. By shifting from the corrective to the usage-based preventive policy, the wheels are re-profiled more frequently (12 times on average) but in smaller cutting steps. The wheel defects have an exponential growth and removing the tiny cracks from the wheel surface reduces the degradation rate [7]. The comparison between the corrective and usage-based preventive policies proved that the usage-based policy has improved the lifetime of the wheels and increased their reliability [6].

The major challenge of the usage-based preventive policy is estimating the wheel condition. The usage-based policy makes an approximate estimate of the wheel condition using the time and mileage. As a result, this policy has failed to avoid unexpected failures and over-maintenance, and to reduce the overall maintenance cost. To estimate the wheel condition based on the physical and statistical approaches, several assumptions are made about the operational situations [3]. Trains work in various environmental and operational situations, such as train velocity and acceleration, axle load, wheel-rail adhesion, and rail profile and track pattern. Such parameters affect the wheel wear and fatigue and, accordingly, change the degradation rate. In addition, the wheel-rail interaction and consequently the degradation rate varies between the right and left wheels on an axle, from the front to back axles in a bogie as well as from the first to second bogie in a wagon [8, 9]. Therefore, physical and statistical models are not broadly applicable to assess the wheel condition properly.

A condition-based maintenance procedure significantly relies on the condition data. Detecting the existing and potential defects using a sensor or a set of sensors is generally called condition monitoring which is appropriate for systems that deteriorate over time. An effective condition monitoring system (CMS) should detect any deviations and should accurately estimate the degradation level. The information obtained by CMSs can be used to optimize maintenance activities. Accordingly, condition monitoring can be the most convenient method for estimating the wheel condition.

CMSs are currently used to detect the wheel failure for a corrective policy. In this case, the condition of the wheel with the most severe defect has the dominant role in the maintenance planning, while the condition-based maintenance policy tries to optimize the maintenance plan and to avoid unexpected failures and over maintenance, based on the conditions of all the wheels of a train. As a result, a condition-based policy can increase the effectiveness (preventing unexpected failure), efficiency (preventing over maintenance), and reliability of the maintenance.

1.2. WHEEL CONDITION MONITORING

Wheel condition monitoring has been and still is the subject of many studies. A CMS can directly measure the defect features, or indirectly the defect effects [10]. For direct monitoring, some sensors, such as ultrasonic once, are used to detect the cracks. The wheel defect produces a contact force that is transferred to the track and vehicle. Therefore, the wheel condition can be indirectly estimated by measuring the responses of the wheel or rail such as strain, vibration, and acoustic responses. Installing sensors on every wheel is challenging due to the expense, implementation and maintenance. For example, the Dutch railway company has about 3000 car bodies with around 24000 wheels [6]. For this reason, track-side measurement has been given more attention.

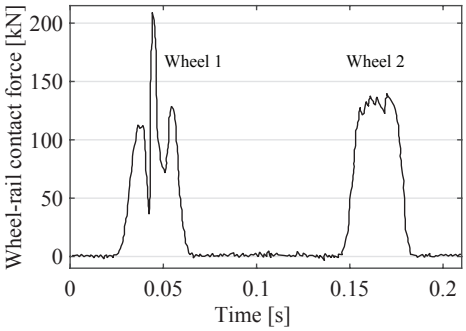

Figure 1.1: A vertical wheel-rail contact force measured by a strain-based WILD with a 100mm flat on the first wheel and for 50 km/h velocity [4].

Wheel Impact Load Detectors (WILDs) are common wayside wheel monitoring systems. They measure the rail response such as strain [5] and vibration [11], by a sensor or a set of sensors to estimate the condition of the in-service wheels. The first generation of WILDs was introduced in 1983 [12] and then rapidly became a widespread commercial system [13]. Figure 1.1 presents the vertical wheel-rail contact force signal generated by the passage of two wheels. The first wheel has a 100mm flat that caused 200kN peak force, and the second wheel has a tread with local spalling [4].

Different studies have attempted to interpret and use the data measured by WILDs to estimate the wheel condition accurately and reliably. One common criterion to quantify the wheel condition is the peak of the data acquired by a WILD. Nielsen and Johansson [1] reviewed the results of some experiments investigating the wheel defects using the peak value criterion. They used the peak acceleration and the peak force collected by accelerometers and strain gauges. The results showed a considerable fluctuation in the peaks especially when the trains had higher velocity and the wheels had more severe defects. Later [4], they investigated the effect of train velocity, axle load, and the defect types on the measured peak forces. Figure 1.2 presents the peak forces collected from two different defects for different velocities and axle loads.

The results in Figure 1.2 present an extreme variation even when the train velocity, the axle load, and the defects were kept constant in the repeated tests. They related this fluctuation to variation in the track property and to the random position of the defect with respect to the sensors. To measure more reliable data and avoid this fluctuation, the track stiffness over the measurement station can be maintained similar, but the position of the defect with respect to the sensors is out of control. Therefore, WILDs usually exploit multiple sensors to cover the whole wheel circumference.

The first drawback of this method to quantify the wheel condition is the large variation output that reduces the reliability of the method. The train velocity and the axle load have a significant effect on the measured data. Partington [12] excluded the effect of axle load by means of two methods to define two other criteria. First, by using the force ratio that is calculated by dividing the peak force by the average force collected by multiple

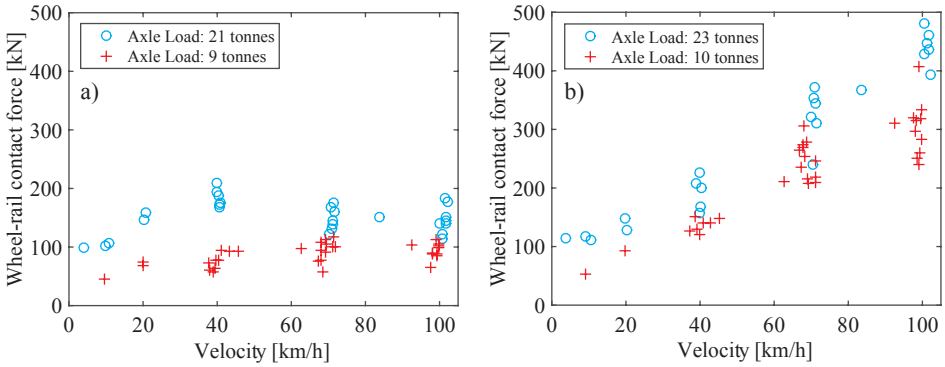

Figure 1.2: Measured peak forces for different train velocities and axle loads with a) a 100 mm flat and b) a 0.5 m long local defect [4]

sensors. The second approach is the subtraction of the peak force and the average force that is called dynamic force. In spite of excluding the effect of axle load, the train velocity is an out-of-control parameter that causes variation in the magnitude of the peak force, dynamic force or the force ratio.

The second limitation is that these criteria fail to distinguish between different defect types. The rate and mechanism of the wheel degradation are influenced by defect type. Therefore, estimating the defect type is significant to provide a comprehensive estimate of the wheel condition. The peak force, dynamic force or the force ratio somehow show the existence of a defect but are unable to identify the defect type.

In addition, a severe defect dominates the other defects of a wheel. Furthermore, the measured dynamic force and the force ratio of a wheel with multiple defects including a severe defect can be smaller than a wheel with a similar severe defect. Because the average of the contact force for the first wheel is higher than the second one. Therefore, these criteria can lead to false interpretation.

Another weakness of the current criteria is difficulty in detecting the minor defects such as spalling, periodic out-of-roundness and small shelling at an early stage. Asplund et al. [14] also used these criteria but finally concluded that they only detect the severe defects that greatly contribute to the contact force. As a result, developing an effective and reliable method for detecting and identifying the wheel defects is still an open issue.

1.3. RESEARCH OBJECTIVE AND RESEARCH QUESTIONS

This dissertation aims to answer the following main research question:

How can the extent of railway wheel defects be accurately estimated?

To achieve the main goal of this research five key research questions should be answered. The condition monitoring process includes three main steps: data acquisition, data processing and condition estimation. The major contribution of this dissertation is made

to the data processing and condition estimation. In the data acquisition step, the data collected by WILDs is used. Different researchers have proposed and exploited various methods for each step. Therefore, a comprehensive literature review is required to answer the first key question:

1. What are the state-of-the-art technologies for estimating the wheel condition?

An individual static sensor makes a partial observation of a moving wheel. A WILD normally measures the rail responses at different points (e.g., at 16 points [5]). Such a configuration collects data from different portions of the wheel circumference. This discrete measurement needs a fusion method to associate the partial data collected by the multiple sensors at different points. Generally, the fusion method can be applied at three different levels: the data level, the feature level, and the decision level [15, 16]. Hence, the second key question is emerged as follow:

2. How can the data collected by multiple sensors mounted along the rail be fused to reconstruct a new informative signal?

The results of the fusion process are influenced by several parameters such as the wheel size, number of sensors, defect type and severity, measurement noise, train velocity, axle load, and the position of the defect on the wheel surface with respect to the sensors. To evaluate the sensitivity of the fusion process, the below question should be answered:

3. How do the influential factors affect the reconstructed signal?

There is a range of variation in the reconstructed signals due to the influential factors. The reconstructed signals should be investigated to attribute to specific defects types and to estimate their severity. Hence, the next question should be responded:

4. How can the defect types and their severity be detected?

Finally, the research should be validated by answering to the following question:

5. How can the proposed method be tested and validated?

1.4. RESEARCH METHOD

This dissertation aims to associate the data collected by multiple sensors to generate a new informative signal. To determine the relation between the samples collected by the sensors a few parameters should be known such as the sensor intervals, sensor sampling frequency and the wheel diameter. According to the wheel circumference and the sensor configuration, the data are mapped over the circumferential coordinate. In this research project a theoretical method is developed. Then, the proposed method is tested using the simulated data generated by VI-Rail. Using the simulated data gives the possibility of changing the parameters and carrying out a parametric study. This study provides a

detailed insight into the method.

Moving of a defective wheel with different velocities and axle loads influence the wheel-rail interaction and the signal reconstructed. As a result, there is a range of variation in the signal reconstructed for each defect. Therefore, to classify the wheel defects the pattern recognition tools are exploited. Finally, the developed method is validated by a laboratory test. For practical implementation, a few issues are raised. This dissertation makes some assumptions and limitations that should be considered for the field operation.

1.5. OUTLINE OF THE DISSERTATION

Figure 1.3 draws the road map of the dissertation. Each chapter covers an individual stage or several stages of the condition monitoring process. In addition, each chapter aims to answer an individual key research question. Finally, the last chapter points to the main research question.

Chapter 2 gives the background, investigates the state of the art condition monitoring methods, and clarifies the scientific gaps; corresponding to the key question 1.

Chapter 3 formulates the fusion process and explains the relation between the samples collected by multiple sensors; corresponding to the key question 2.

Chapter 4 carries out a detailed parametric study to investigate the sensitivity of the fusion process and to explain the expected results; corresponding to the key question 3.

Chapter 5 uses the pattern recognition tools to detect the defect type and to estimate the defect severity using the reconstructed signal; corresponding to the key question 4.

Chapter 6 validates the fusion method using a set of lab tests to prove the applicability of the proposed method; corresponding to the key question 5.

Chapter 7 draws the main conclusions of the research, answers the research questions, and gives the final recommendations.

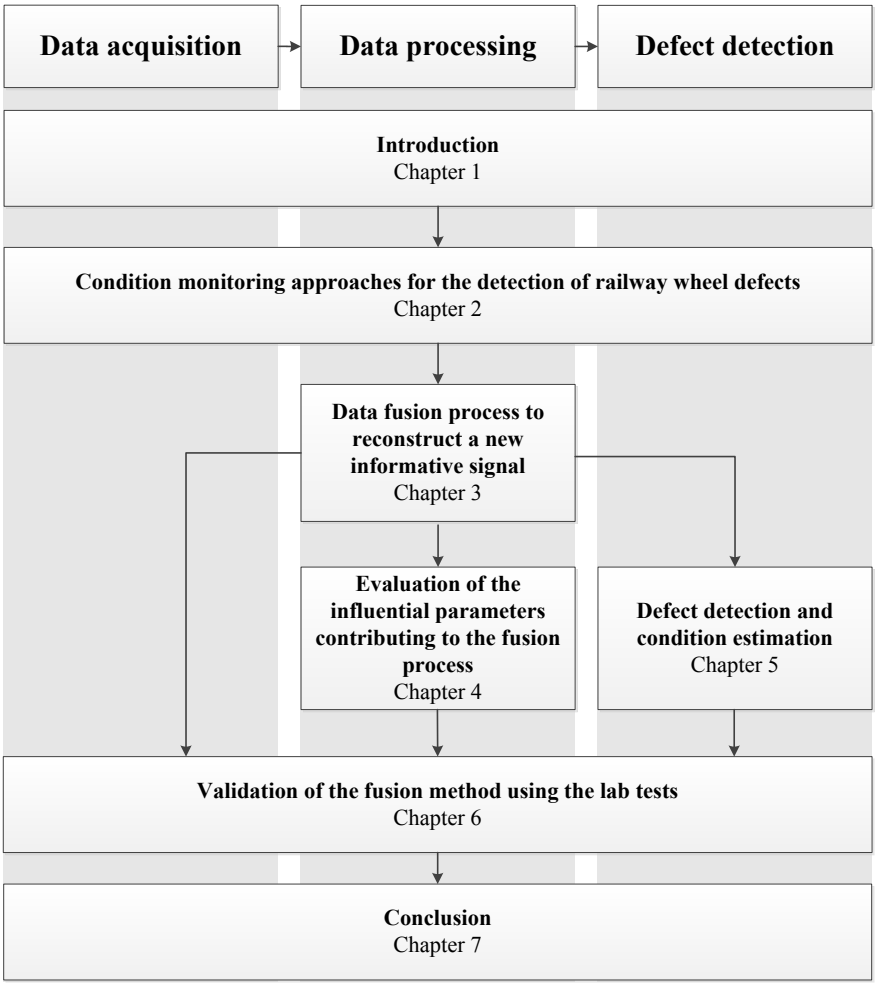

Figure 1.3: The road map of the dissertation. The position of the boxes shows the coverage of the chapter with respect to the condition monitoring process.

2

CONDITION MONITORING APPROACHES FOR DETECTION OF WHEEL DEFECTS[1]

This chapter describes the state-of-the-art approaches for in-service monitoring of wheel defects. Condition monitoring approaches in the railway industry can be generally categorized into the following four groups: track-based vehicle monitoring, track-based track monitoring, vehicle-based vehicle monitoring, and vehicle-based track monitoring [18]. The focus of this research is on the railway wheels. Section 2.1 explains the wheel defects and discusses their features. Two possible methods for the wheel monitoring are the track-based wheel monitoring (wayside) and vehicle-based wheel monitoring (on-board). As a result, the literature is divided into these two main groups, on-board methods (section 2.2), and wayside methods (section 2.3). As mentioned in Chapter 1, any condition monitoring process contains data acquisition, data processing and condition estimation. Therefore, the available approaches can be classified based on their contribution to the steps of the condition monitoring process, but the data processing, and condition estimation steps totally depend on the data acquisition step. Therefore, the literature, which are reviewed in section 2.2, and section 2.3, are categorized in subsections based on sensing technique such as strain gauges, ultrasonic, vibration, and acoustic technique. Section 2.4 discusses and compares the methods from different aspects such as objective of the monitoring, measurement specifications, and condition estimation method, to identify the state of the art.

2.1. WHEEL DEFECTS

Wheels rotate on rails and make the train movement. Figure 2.1 illustrates a schematic view of a wheelset, consisting of two wheels connected with an axle, and a track structure

[1] This Chapter is a revised version of Alemi et al. [17].

consisting of rails, rail pad, sleeper, ballast, and base. Wheel-rail interaction causes wear and fatigue defects. Nielsen and Johansson in [1] sorted the wheel defects and discussed the reasons of their occurrence. Table 2.1 categorizes the wheel defects explained in [1] based on their causes.

Wheel flat is a severe defect that accidentally happens by sliding the wheels. This defect generates high impact forces that is damaging to the vehicle and track. Therefore, numerous studies have been and are conducted to detect the wheel flat as early as possible and to investigate and reduce its detrimental effects. However, detecting the wheel flat can be used to make a corrective maintenance plan than a preventive. In addition, wheel flat rarely happens and has a small share in the re-profiling reasons [6].

Polygonal defect is a periodic radial deviation from the nominal wheel radius around the wheel circumferential coordinate. Polygonal defects are caused for a variety of reasons in different phases. The reasons can be explained by inhomogeneous properties and misaligned axle hole during the manufacturing process or by misalignment in the re-profiling and maintenance process [1], or by polygonal wear during the operation [19]. These defects can be a pure sinusoidal wave with a long wavelength that covers the wheel circumference or a combination of multiple waves with different harmonics.

According to the wavelengths of the polygonal defects, a range of excitation frequencies is generated that is changed by the train velocity. Normally, wheel–rail contact forces generated by polygonal wheels are lower than the alarm threshold. In addition, detecting these defects by visual inspection is difficult. Moreover, polygonal defects do not contribute to high impact force. Therefore, the usual methods such as measuring the dynamic force are not effective. However, due to the train velocity variation, the excitation frequency may approach to the fundamental resonance of the track and vehicle that leads to high impact force, high-frequency vibration, noise, and reducing the passenger comfort. As a result, in-service detection of these defects is an open issue.

Shelling and Spalling caused by Rolling Contact Fatigue (RCF), and are among the main reasons of the wheel re-profiling [6]. These defects initiate as a crack and evolve over a course of time. Therefore, to have a preventive maintenance policy, these defects should be detected in the early stage. Modern trains tend to move faster with higher axle loads. Hence, wear as the dominant reason of the wheel damage has been altered to fatigue [20]. This phenomenon shifts the defects from surface to sub-surface. As a result, detection of these defects is more challenging than the others.

In addition to the wheel condition, the wheel CMSs can provide some information about the train. The number of axles, train velocity, train acceleration, and derailment coefficient are some examples of the features that can be estimated by a wheel monitoring system. This information can be directly used as a criterion of the wheel condition or can be indirectly used in the data processing and condition estimation steps. Therefore, some wheel CMSs have been developed to collect these features.

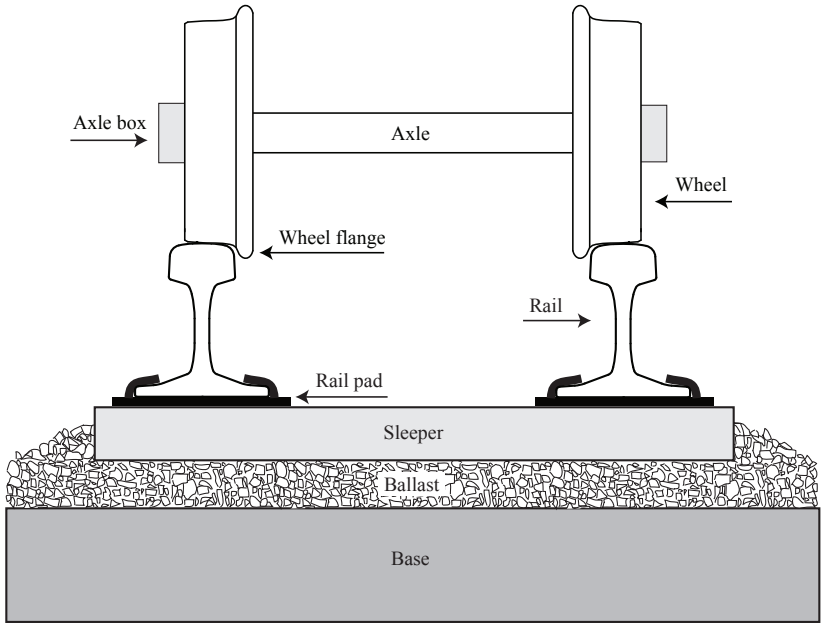

Figure 2.1: A Schematic view of wheelset and track structure.

Table 2.1: Wheel defects and the reasons of their occurrence [1].

Causes	**Defects**	**Moment of life time**
Misaligned axle hole, misaligned re-profiling, and inhomogeneous material	Periodic non-roundness, Non-periodic non-roundness, Discrete defect	Before the operation or in service and over a course of time
Wear and fatigue	Spalling, Shelling, Roughness,	In service and over a course of time
Sliding and blocked brake	Corrugation, Flat	In service but at a moment

2.2. ON-BOARD METHODS

Vehicle-based monitoring methods provide continuous and comprehensive data but they are complex in terms of mounting, implementation and maintenance. In addition, on-board sensors measure signals composed of both track irregularities and wheel defects. Ward et al. in [18] reviewed the on-board methods used for the track and vehicle monitoring. In this research, we focus on the wheel condition monitoring and in the following subsections, the on-board methods such as magnetic, ultrasonic, acoustic and vibration techniques will be discussed.

2.2.1. VIBRATION TECHNIQUE

Liang et al. in [21] simulated the wheel flat and rail surface defects. They carried out a set of analysis to detect the wheel flat. They did different time domain and time-frequency analysis of vibration and acoustic signals such as the Crest factor, Skewness, RMS and peak values as well as short-time Fourier transform, Wigner–Ville transform and the wavelet transform. They compared the simulation results to the vertical forces and accelerations measured by five accelerometers mounted on a roller rig. Displacement and velocity were computed by integrating the vertical acceleration of the axle box. When the wheel velocity increased from 3.5 km/h to 15 km/h, differences arise between the results of the simulation and experiment and the methods lose their ability of detecting the wheel flat.

Their research was extended in [22] by concentrating on the noise elimination and time-frequency analysis to improve the results. They assessed the performance of adaptive noise cancelling as a pre-processing method and looked at four time–frequency transforms as the processing methods including smoothed pseudo Wigner-Ville transform, the short time Fourier transform, the Choi-Williams transform and the wavelet transform on the raw measured acceleration signals. These tests, like prior work, were carried out at a low velocity hence using these methods for real field application is challenging.

Jia and Dhanasekar in [23] investigated two wavelet methods to detect the wheel flat. They simulated the vertical acceleration of a bogie to generate the required data. Two wavelet methods are decomposing of average signal wavelet and the wavelet local energy averaging. To select the convenient wavelet function the authors tried five different wavelets and selected the Daubechies as the best one. They carried out the simulations for a wagon moving with a constant velocity at 80 km/h that is much higher than velocity in [21], and [22].

Li et al. in [24] investigated two methods to detect the wheel flat using the simulated axle box vibration signals. They ran the simulations for velocities at 100 and 200 km/h and carried out the laboratory tests at 40 km/h. They compared empirical mode decomposition (EMD) and ensemble EMD (EEMD) and showed the effectiveness of the EMD method for flat detection. They extended their research in [25] by exploiting adaptive multiscale morphological filtering (AMMF) for flat detection at 100, 150 and 200 km/h velocities for the vibration signals simulated by a vehicle-track model, and measured in lab tests. The on-board vibration technique has been well developed for high velocities but just for severe defects such as flats. Therefore, a more comprehensive method would include all defects.

2.2.2. ULTRASONIC TECHNIQUES

Several simulations and laboratory tests were done in [26] to investigate the possibility of mounting a ultrasonic sensor on the wheels to monitor the wheel-rail flange contact. When the ultrasonic pulses encounter an identical interface by a full contact, the signal will be completely transmitted. The simulations and laboratory tests measured the proportion of the reflected and transmitted ultrasonic wave from no contact to perfect contacts. By simulation modelling, they determined the proper position for the ultrasonic transducer on the wheel. In the experimental tests, they loaded a section of wheel and rail by a bi-axial frame to produce different wheel-rail contact conditions. This method can be used for monitoring the wheel wear by considering the fact that the wheel wear changes the contact features and consequently changes the reflected wave. This method also needs extra analysis to exclude the effect of the rail irregularities.

2.2.3. ACOUSTIC TECHNIQUE

Frankenstein et al. in [27] designed an on-board monitoring system by putting an acoustic sensor inside the wheelset Axle. They carried out a simulation and a laboratory test based on the acoustic sounds produced by the wheel defects. Different artificial cracks were tested for the laboratory test by bearing in mind that the crack size affects the intensity and length of the signal. They used the elastodynamic finite integration technique to simulate the propagation of an ultrasonic sound. This method can detect minor defects such as small cracks but the difficulties of the on-board monitoring systems are still remained.

2.2.4. MAGNETIC TECHNIQUE

The derailment coefficient is the ratio of the lateral to the vertical wheel-rail contact forces. This coefficient is usually measured by strain gauges mounted on a particular wheelset. Since the wheelset is a rotating component, Matsumoto et al. in [28] used non-contact gap sensors to remove the rotating sensors by measuring the lateral contact force from the lateral bending of the wheel. Figure 2.2, shows the configuration of such non-contact gap sensors. They extended their research in [29] by implementing the method suggested in [28] at different commercial lines using the in-service trains. They assessed the influential parameters such as friction and track irregularity that alter the derailment coefficient. This method can also be used for monitoring the wheel wear through monitoring the derailment coefficient.

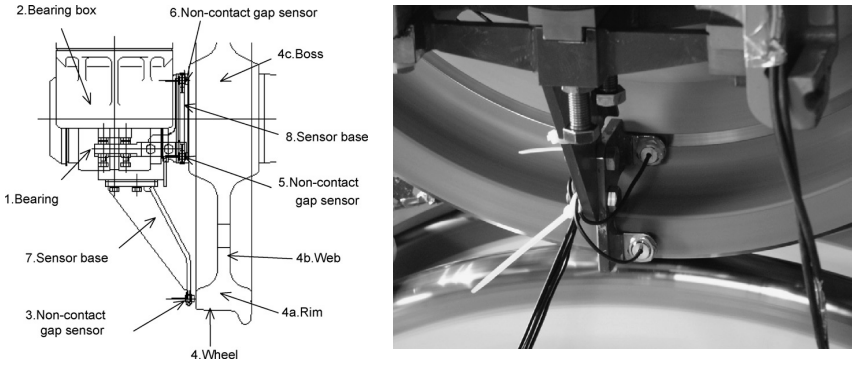

Figure 2.2: The configuration of the gap sensors for measuring the lateral force [28].

2.3. WAYSIDE METHODS

Wayside measurement is the monitoring of train equipment by sensors mounted on the rail or along it. The preliminary model of the wayside wheel defect detector was built in 1983 and attached to the North East Corridor between New York and Washington to measure the wheel impact load to detect the defective wheels [12]. The wayside method rapidly became a popular method for the wheel monitoring. For example, in Sweden the first wayside detector was installed in 1996, while in 2016 more than 190 wayside systems were working [14].

Some wayside detectors investigate the wheels to directly find cracks and defects. Other wayside systems measure the signals generated by the wheel-rail interaction such as acoustics, vibration and strain. The wheel and rail characteristics create the features of the wheel-rail contact. By knowing the current condition of the rail, the wheel condition can be indirectly estimated by extracting the defect features. This section reviews the wayside monitoring systems according to their measurement approaches.

2.3.1. ULTRASONIC TECHNIQUE

Salzburger et al. in [30] proposed a wayside and in-service monitoring system to detect the surface cracks, based on ultrasonic inspections. This system contains two probes per rail and a particular track for installing the probes. Every sensor is able to completely assess the circumference of the wheel and the second sensor was only used for double inspection. Similar other typical ultrasonic inspections, this system relies on pulse-echo, and pulse transmission, but this system does not need liquid couplings during the measurements. In addition, it emits waves in circumferential orientation to observe the surface and sub-surface cracks. The amplitudes of the emitted and reflected impulse, caused by cracks, are assessed in an A-scan plot as function of time. The CMS needs a dramatic change in the track and is therefore limited to specific stations. In addition, the trains velocity is restricted to 15 km/h.

Brizuela et al. in [31] carried out a simulation and a laboratory test to evaluate the ability of Doppler effect in the wheel defect detection. As illustrated in Figure 2.3, two

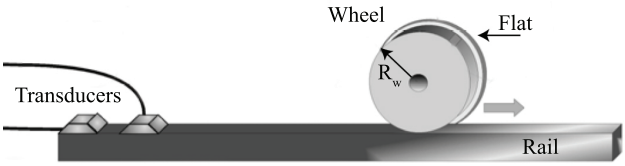

Figure 2.3: The configuration of a wheel-flat detector [31].

piezoelectric transducers were mounted on a rail. The wheel-rail contact point reflects the monochromatic wave propagated in the rail. Relating to the train velocity, the wheel-rail contact point is moving and the frequency of the propagated wave is shifted that is calculated according to:

$$f_{U_d} = \frac{2\omega R_w}{V_U} \times f_U \tag{2.1}$$

where f_{U_d} is the shifted frequency, f_U is the frequency of the signal propagated, R_w is the wheel radius, ω is the angular velocity, and V_U is the velocity of the ultrasonic wave. Surface wheel defects change the frequency shift that is used for the defect detection. The authors applied a time-frequency analysis and a high pass filter to process the data acquired.

In spite of the capability for in-service application and monitoring the whole circumference, this method needs special rails, and constant and low velocity movement. In addition, this method just detects the existence of the defects and could not provide more information about the defect type and size. Hence, they developed a method to evaluate the wheel flat features [32]. The length and depth of flats are obtained via a theoretical calculation that was fed by the period of ultrasound wave, which travels to the rail-wheel contact point. They assessed their method through a simulation and a laboratory investigation, but its limitation for real field application is maintained. Kenderian et al. in [33] assessed the capability of the combination of ultrasonic technique with Laser and capacitive air-coupled transducer for monitoring wheel defects. They used this method for detecting surface and sub-surface defects in the wheel tread and flange.

2.3.2. ACOUSTIC TECHNIQUE

Thakkar et al. in [34] carried out laboratory and field tests to measure the velocity of the acoustic wave and the attenuation coefficient. Then, an analytical acoustic emission model was built using these factors. To detect the defects in the wheel-rail interaction area, they used the envelope of the root mean square of the signal as a comparison parameter between the emitted wheel-rail acoustic wave and the model. They extended their research to wheel flat detection in [35]. They assessed the frequency and harmony of the acoustic wave propagated by defective wheel to detect the wheel flat. This is built on the fact that the quantity, quality and position of the wheel flat change the features of the normal signal. Figure 2.4 displays the structure of the test rig.

Wheel defects emit periodic acoustic impulses regarding to the train velocity. Based

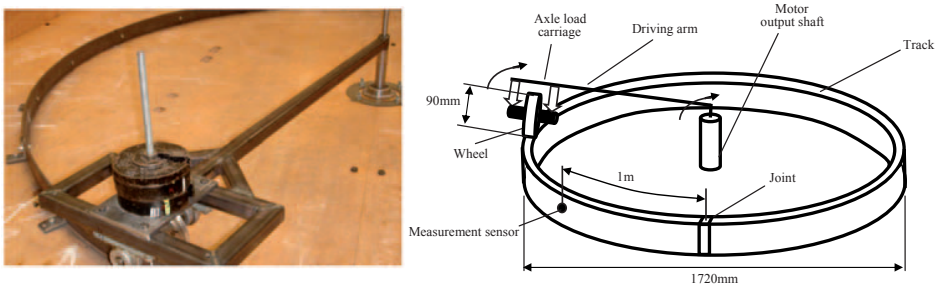

Figure 2.4: The structure of the acoustic test rig [35].

on this consideration, recognition of a repetitive pattern in acoustic signals was discussed in [36]. For this purpose, Bollas et al. firstly applied a low pass filter on the acoustic waveform measured by the sensors attached on the rail. Then the root mean square of the signal was calculated by considering 40 ms as the time window. The frequency spectrum of the signal acquired was obtained using a Fourier Transform. In the last stage, the Harmonic Product Spectrum method determined the fundamental frequency that explains the existence of a repeated impact caused by a defect. In addition, they used Time Driven Data method to find the wheel defect. They obtained the features of the acoustic signals of a normal train and compared them with the measured signals from the defective train. The trend of these signals detect the presence of defects. In their assessments, the train velocity was around 8-16 km/h. The ability of this method should be checked further for higher velocities and lower signal to noise ratio. Furthermore, these methods only indicate the existence of a wheel defect in the train and cannot detect the defective wheel and its severity.

2.3.3. LASERS AND HIGH-SPEED CAMERAS

In [37] Yang et al. exploited lasers to emit light on the wheel surface and used a high speed camera to catch the features of the wheel profile. This system can be mounted on normal rails and can be used for high-speed train up to 160 km/h. The comparison between the obtained and the reference profile leads to defect diagnosis. The main challenges in that research were noise cancellation and accurate recognition of wheel profile. Hence, the authors developed an image-tracking algorithm to capture the wheel profile.

2.3.4. VIBRATION TECHNIQUE

Bracciali and Cascini in [38] used an acceleration sensor to detect flats and corrugations in wheel tread using the energy comparison and the cepstrum analysis. Based on the repetitive trace of wheel flats, the power cepstrum is a practical approach to find the echoes of the wheel flat in a noisy signal. This method just detects the existence of the wheel flat in a bogie, and could not identify the exact defective wheel. The exerted energy from a wheel to the rail depends on the train velocity, so the tests were carried out with constant velocity. Different positions and directions for six piezoelectric accelerometers

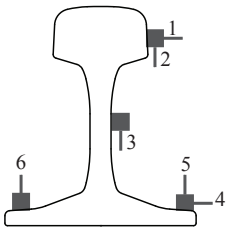

Figure 2.5: Different positions and directions for installing an accelerometer on the rail [38].

were experienced and the best location was obtained (position and direction 2 in Figure 2.5).

Skarlatos et al. in [39] applied a fuzzy-logic method to diagnose the wheel condition such as good, low damaged, faulty and dangerous. To achieve this purpose, they used the vibration magnitude, the centre frequency band and the train velocity as three inputs, while the output was the condition of the train. In their field tests, the accelerometers were mounted on position 5 according to Figure 2.5. In addition, they investigated the relation of the vibration magnitude to the train velocity and frequency. The vibration signals were measured at different train velocities and statistically analysed. As a result, it was concluded that the train velocity and frequency have considerable effect on the vibration signal.

Belotti et al. in [11] exploited acceleration signals to detect wheel flats. In the second step, they quantified the defect severity using the Wavelet Transform as a time–frequency processing approach. The train velocity is calculated using the distance between the axles. Furthermore, they counted the train axles using the measured data. Figure 2.6, presents the acceleration signal measured and the top plot presents the result of the axle counter. It is noticeable that the acceleration signal could not directly refer to the number of axles passing the measurement point, therefore, a supplementary process is required. From the practical aspect, the wagons with defective wheels are separated and planned for corrective maintenance. Therefore, they concentrated on detecting the bogies containing the wheel flat, instead of detecting individual defective wheel. In their field measurements, the acceleration signals were collected by one sensor at different train velocities from 10-100 km/h, with 10 km/h interval.

The typical examples of the signals measured by a shear bridge and an accelerometer are given in Figure 2.7. Shear-bridges, which are constructed by strain gauges, have a limited effective zone. Therefore, full interaction of the defective area of the wheels with sensors is crucial. To overcome this drawback, Lee and Chiu in [40] proposed a method to convert the measured acceleration signal to the vertical force. They presented the relation between the input force $F_t(t)$, and the output acceleration $a_t(t)$ by

$$a_t(t) = \int_{-\infty}^{\infty} h_t(t-\tau).F_t(\tau).d\tau \tag{2.2}$$

where $h_t(t)$ is the system response. The conversion of Equation 2.2 into the frequency

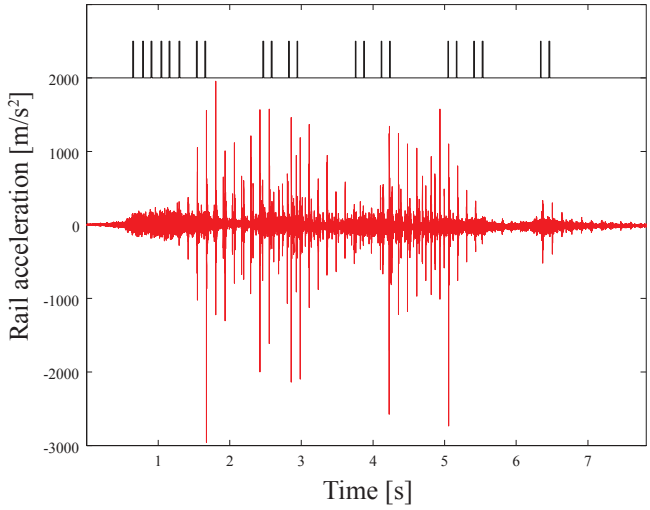

Figure 2.6: An example of the measured acceleration signal [11].

domain changes the convolution integral to a multiplicative relationship between $F_t(t)$ and $a(t)$ in the frequency domain:

$$A_\omega(\omega) = H_\omega(\omega).F_\omega(\omega) \tag{2.3}$$

The transfer function $H_\omega(\omega)$ can be acquired using a set of known impact forces and rail acceleration responses and averaging at different points. This method can be inversely used to calculate the unknown forces from the acceleration and transfer function. They compared two methods, inverse analysis method as a deconvolution technique, and root mean square method, to discover the relation between track acceleration response and the magnitude of the force. Besides accelerometers, shear bridges were also used for evaluating the results obtained in their field measurements. Inverse analysis method delivered good performance to convert the measured acceleration signal to the force especially beyond the effective zone of the strain gauge. Figure 2.8 presents two examples of the force signals reconstructed by the inverse analysis method. In these examples, the defective area on the wheel contacted the rail outside the effective zone of the shear bridge. Therefore, the shear bridge could not sense the wheel defect perfectly, while the signals reconstructed from the acceleration data fully covered the wheel defect.

Looking at the standard deviation of the force obtained by the shear bridges in the calibration process, authors concluded that shear bridge measurements are not dependent on the train velocity and load within their operational condition (79-109 km/h and 24-141 tonnes of wagon load).

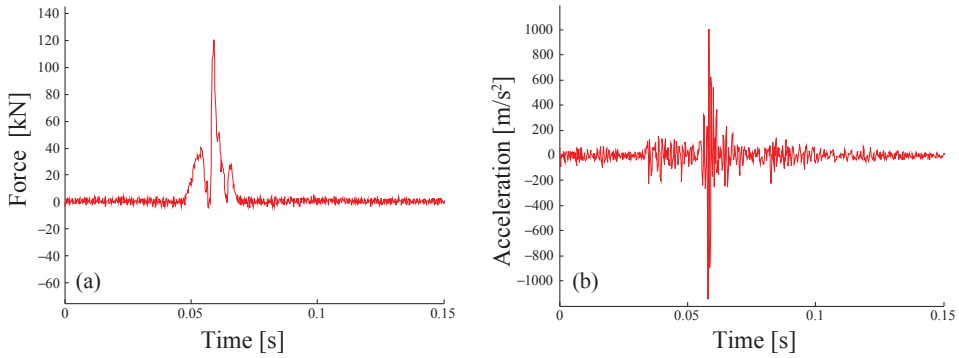

Figure 2.7: a) A force signal measured by a shear bridge and b) an acceleration signal measured by an accelerometer [40].

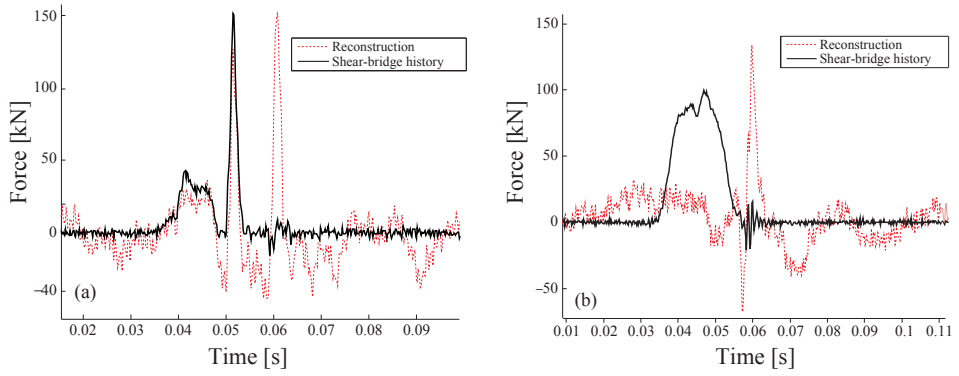

Figure 2.8: The force signals measured by a shear bridge and the signals reconstructed from the data measured by an accelerometer [40].

2.3.5. STRAIN GAUGES

Measuring the surface defects by means of strain gauges is a conventional and commercial technique for the wheel condition monitoring. This CMS is called Wheel Impact Load Detector (WILD) and some examples of the present commercial products were mentioned in [13]. Wheels impose strain on the rail and alter the resistance of the strain sensors mounted on the rail. Through this method, the strain gauges measure the impact forces caused by the wheel defects. The position, number, and arrangement of these sensors are determined according to the purpose and condition of the measurements.

Nielsen and Johansson in [1] and [4] investigated the effect of train velocity, axle load, and the defect types on the peak of the data measured by strain gauges and accelerometers (see Figure 1.2). The results demonstrate that these three parameters changed the measured peaks. In addition, the repeated tests obtained scattered results, even when all the parameters were kept constant. Furthermore, this fluctuation increases for the higher velocities and the more severe defects. As a result, using the peak value of the strain and acceleration signals is not a reliable method.

Stratman et al. in [5] exploited the data acquired from a WILD to indicate the defective wheels. The vertical force at each point was measured by two strain gauges and the lateral force was measured by two others. The WILD was equipped with 128 welded strain gauges to gather the vertical and lateral forces at 16 points from two rails. For a reliable and accurate monitoring, the sensors should measure entire the wheel circumference for the wheels with different diameters. The authors claimed that the collected data in [5] covered 90% of the wheel circumference for the most cases.

Commonly, the measured strain is converted to the force that is directly used as an indicator of the wheel condition. For instance, the Association of American Railroads defined 400 kN [5] and the Swedish National Rail Administration defined 290 kN [4] as a threshold to detect the defective wheels. According to [4] the train velocity and the axle load influence the measurement. Stratman et al. in [5] used two methods to eliminate the effect of the train weight using the forces measured at 16 points. First, they calculated the differences between the maximum value and the average of the measured forces, which is called the dynamic force. In the second method, the ratio of the maximum force (F_{max}) to the average force ($\bar{F}$) was calculated as follow:

$$F_D = F_{max} - \bar{F} \tag{2.4}$$

$$R_F = \frac{F_{max}}{\bar{F}} \tag{2.5}$$

where F_D is the dynamic force, and R_F is the force ratio. These values are called "semi-normalized impact forces", because they eliminate the influence of the train weight on the measured force, and leave the effect of the train velocity.

The authors in [5] suggested two indicators based on the trends of the dynamic force, in order to detect the wheels with high probability of failure. These indicators assess the trends of rapid increase in the dynamic force during a particular period (within 50 and 20 days) for two groups of wheels. First, wheels with high dynamic impact force (this high impact load is lower than the threshold) and second, wheels that are running at a normal impact. Based on these methods, 15.8% of the wheels in North America were eliminated

because of their high probability of failure while their impact forces were lower than the threshold limit.

Palo et al. in [9] measured the lateral wheel-rail forces by strain gauges to assess the effect of wheel position in a bogie on the lateral forces. The assessment was carried out in a 484 m radius curvature at a specific research station. The trains operated within a speed range up to 100 km/h, and with severe weather such as snow, and temperature variation between -40°C to +25 °C. In [41] they exploited high-speed cameras and lasers for the wheel profile features monitoring and used the wheel-rail forces to decide for the wheel maintenance. The fusion of these two pieces of data about the wheel condition, gives valuable information for maintenance decision making.

2.3.6. FIBRE OPTIC SENSING TECHNOLOGY

A Fibre Bragg Grating (FBG) sensor is created by exposing a short section (around 1 cm [42]) of an optical fibre to ultra-violet radiation over a phase mask in a way that the mask pattern creates a periodic refractive index [43]. The light in an optical fibre travels freely while the FBG sensor reflects back a specific wavelength of the light spectrum relating to the features of the Bragg [42]. Mechanical and thermal stresses change the refractive index of the FBG sensor and consequently change the wavelength of the reflected light spectrum which is detected by an optical interrogator. The reflected back wavelength (λ_B) is calculated according to

$$\lambda_B = 2n_e\Lambda \tag{2.6}$$

In this Equation, n_e is the refractive index of the core and Λ is the grating period of the FBG sensor. The alteration of the reflected wavelength ($\Delta\lambda_B$) shows a nearly linear relation to the alteration of the strain and temperature, which are respectively ~1pm/$\mu\varepsilon$ and ~11pm/°C. The wavelength shift can be measured by two common methods: wavelength-division multiplexing and time-division multiplexing, which are used in the interrogating system [44].

Lee et al. in [45] used FBG sensors to assess the derailment probability. The weight of the train is used for assessing the off-loading ratio that estimates the probability of the train derailment:

$$R_l = \frac{\Delta F_w}{F_w} = \frac{(F_{w_r} - F_{w_l})}{(F_{w_r} + F_{w_l})} < 0.6 \tag{2.7}$$

F_{w_r} and F_{w_l} are the vertical forces of the wheels in a wheelset. This means that the transferred load in one axle should be limited to 60%. In addition, they remarked the ability of FBG sensors for axle counting, train identification, and velocity estimation.

Figure 2.9 illustrates a typical strain signal measured by a FBG sensor showing the passage of two wheels. In this Figure, e_{max} and e_{min} are respectively the maximums and minimums of the signal. In [42] FBG sensors were used to measure the weight of trains in a commercial railway line. They evaluated four methods to correlate the measured data to the weight of two consecutive wheels, F_{w_1} and F_{w_2}, passed the sensor by the following

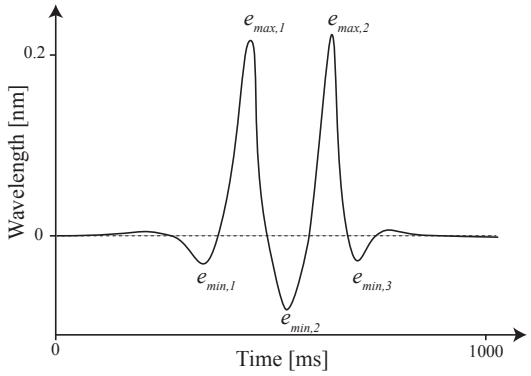

Figure 2.9: A typical output of a FBG sensor which shows strain changes during the passage of a train with 2 axles.

relations:

$$\begin{cases} F_{w_1} = e_{max,1} - e_{min,1} & \text{(2.8a)} \\ F_{w_2} = e_{max,2} - e_{min,2} & \text{(2.8b)} \end{cases}$$

$$\begin{cases} F_{w_1} = e_{max,1} - e_{min,2} & \text{(2.9a)} \\ F_{w_2} = e_{max,2} - e_{min,3} & \text{(2.9b)} \end{cases}$$

$$\begin{cases} F_{w_1} = e_{max,1} - \dfrac{e_{min,1} + e_{min,2}}{2} & \text{(2.10a)} \\ F_{w_2} = e_{max,2} - \dfrac{e_{min,2} + e_{min,3}}{2} & \text{(2.10b)} \end{cases}$$

$$\begin{cases} F_{w_1} = e_{max,1} & \text{(2.11a)} \\ F_{w_2} = e_{max,2} & \text{(2.11b)} \end{cases}$$

The authors concluded that the most accurate methods are the Equations 2.11a and 2.11b with the smallest amount of error [42].

As mentioned earlier, the train velocity and the axle load influence the measurement [4]. Tam et al. in [44] used FBG sensors to measure the train velocity. They considered the distance between the axles as a known value and used the time taken for passing two axles over the sensors (two peaks) to estimate the train velocity.

The main difficulty of counting the axles is dealing with the noisy signals. The defective wheels create an impact on the rails and make some extra peaks in the strain signals. Wei et al. in [46] used FBG sensors to count the axles and proposed two approaches to solve this problem, named X-crossing and D-crossing. Combination of these two methods presented 100% successful rate of the axle detection.

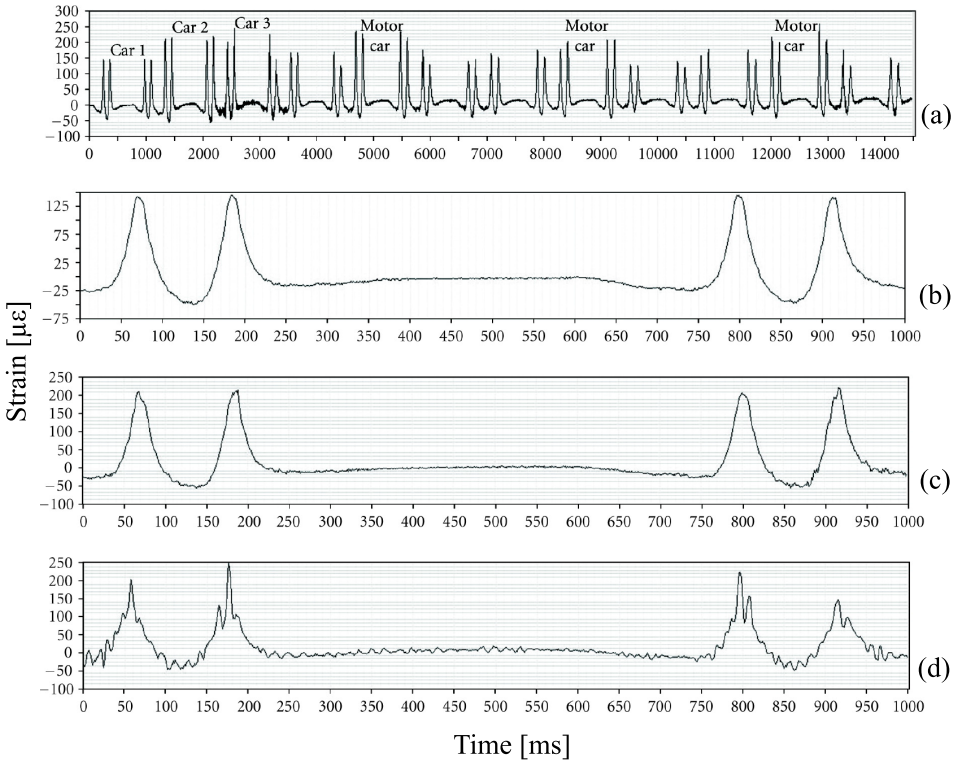

Figure 2.10: The strain signal generated by means of (a) a train, (b) the magnified view of the first car that is healthy, (c) the second car that is somehow defective, (d) the third car that is quite out of round [43].

Wei et al. in [43] fabricated and packaged FBG sensors and proposed a condition index to quantify the wheel condition. The condition index (C_I) is based on the average of the strain changes ($\bar{\varepsilon}$), the train velocity (V) and a scaling factor (α_c). This index estimates the overall condition of four consecutive wheels of a wagon as follow:

$$C_I = \frac{\bar{\varepsilon}}{V} \times \alpha_c \tag{2.12}$$

They validated the proposed index by investigating 29 passenger trains. For the field examination, the FBG sensors were mounted neighbouring the rail foot. These sensors were linked through optical cables in series. Figure 2.10a illustrates the strain signal obtained from one FBG sensor induced by a train with 12 wagons (cars) and 48 axles, with the velocity between 50-90 km/h. Figures 2.10b, 2.10c, and 2.10d present the magnified view of the three first wagons. The wheels of the third wagon were defective and produced high impact forces and high frequency components in the signal.

Filograno et al. in [47] installed several FBG sensors on a straight part of a rail in var-

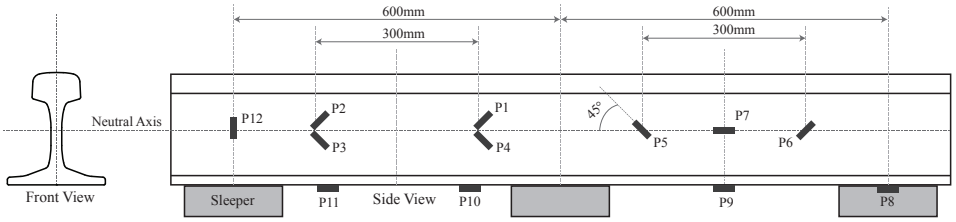

Figure 2.11: The configuration of strain sensors.

ious positions to determine the train velocity, train acceleration, number of axles, train type, dynamic load, and the wheel defects. The train velocity in that sector is usually between 200–300 km/h. They also investigated the effect of variation in the environment temperature on the measured data. For the axle counting, they measured the rapid change in the signal to find the number of peaks. For the train type identification, they matched the number of axles with the prior information from the trains, like the axle distance for different types. By using the time intervals between the peaks in the signal of a wagon, instantaneous velocity was calculated. For estimating the average velocity of a train, the first and the final wheels of a train are used. For measuring the acceleration of a train, the velocity estimated for the first and the last wagons are exploited. They estimated the vertical load using the shear strains to eliminate the sleeper response. They used the sensors positioned at $P5$ and $P6$ in Figure 2.11 that illustrates different positions of the sensors. The rail characteristics and the shear strains give the vertical force as follow:

$$F_{xz} = (\frac{2\varepsilon_{xz} G b_G I_y)}{S_y} \tag{2.13}$$

It means that the vertical force (F_{xz}) is proportional to the differential shear strain (ε_{xz}), the tangential elasticity module (G), the width of the section in the rail neutral line (b_G), and the inertial momentum of the section (I_y), and inversely proportional to the static momentum of the lower part of the rail (S_y). In some cases the calculated vertical force based on this method were higher than the static force (train weight), and in some cases equal or even lower than the static force. They explained this result with difference in the epoxy adherence and imbalance axles and proposed a calibration coefficient k_c multiple to Equation 2.13, which is equal 1.34 [48].

Filograno et al. in [48] used the FBG sensors as [47] to detect the wheel flat. First, they defined a cut off frequency to filter the measured signal. Then, they calculated the energy of the high-pass filtered signal to compare with a threshold to detect the defective wheels. Therefore, this method uses a single sensor to detect the defective wheel. The difficulty of this method is the influence of the adjacent defective wheels on each other. The high-pass filtered signal presents the high frequency components related to the defects. In order to distinguish between the defective wheels they assessed three different scenarios based on phase matching between close-flatted wheels.

In Equation 2.13, the vertical force is estimated, but sometimes the static force (train

weight) is required. The vertical force equals the sum of the dynamic and the static forces. To estimate the static force they supposed the static force as a fraction of the vertical force and as a function of the wheel velocity. Therefore, they carried out some tests and concluded that for 200 and 300 km/h velocities, the dynamic force are around 14% and 21% of the static force respectively. To estimate these values, they measured the vertical force a few times and calculated the average of them. They found a large variation in the measured forces and explained it as a stochastic value.

Pan et al. in [49] designed a structure to install FBG sensors to increase the sensitivity of the vertical force measurement. To achieve this purpose, they positioned the FBG sensor in the centre of a thin steel gauge and suspended the fibre from its two ends. It means that the glue does not cover the whole fibre. This scheme prevents FBG chirping and increases its sensitivity in a ratio of 1.7 with respect to the direct installation. They used an array of 24 sensors, covered 6.6m, to monitor the whole circumference of the wheel. For calculating the sensitivity, they used a standard weight locomotive. This sensitive coefficient is valuable for calibrating the measured FBG wavelength which is used for detecting the dynamic wheel load [49].

2.4. DISCUSSION

The wheel condition monitoring systems pursue different objectives. Therefore, the first part of this section discusses the objectives of the literature reviewed. The CMSs operated in a range of situations such as the condition of rails, trains and the configuration of the sensors that are explained in the second part. Finally, the last subsection discusses the literature based on their method for estimating the wheel condition.

2.4.1. OBJECTIVE OF THE MONITORING

The maintenance policy determines the objective of the condition monitoring system. Some wheel CMSs have been developed to protect the tracks from the high impact forces generated by severe wheel defects. In this case, the objective of the wheel CMS is detecting the trains having wheels with severe defects such as wheel flat. According to the corrective maintenance policy, a threshold is defined to detect the detrimental forces. Therefore, the exact location of the defective wheels in a wagon, and their number are not an issue for this policy. To have a preventive maintenance policy, the wheel CMS should be able to detect the minor defects, and to identify the defect types and their severity for all wheels. As a result, the objective of the wheel CMS can be categorized into these levels:

1. Detecting the train has one or more defective wheels with severe defects;
2. Detecting the wagons with one or more defective wheels with severe defects;
3. Detecting the exact defective wheels with severe defects;
4. Quantifying the condition of all wheels;
5. Identifying the defect type and severity for all defective wheels including the minor defects;

Table 2.2: The objectives of the on-board monitoring systems

Objective of monitoring	Technique or sensor	Assessment level
Flange contact	Ultrasonic technique	Test rig - full scale [26]
		Simulation [26]
Surface defects	Acoustic technique	Test rig - full scale [27]
		Simulation [27], [21]
	Vibration technique	Test rig - scale test [21], [22]
		Simulation [23], [24], [25]
		Field measurement [25]
Derailment coefficient	Magnetic technique	Test rig - full scale [28]
		Simulation [28], [29]
		Field measurement [28], [29]

6. Prognosis the condition of the wheels.

The measurement objective determines the required data acquisition system and the processing method for each level. Therefore, the quality of the condition monitoring system should be assessed according to its objective. Hence, a general comparison between different techniques is not beneficial.

ON-BOARD METHODS

Table 2.2 presents the objectives of on-board monitoring systems that covers the flange contact, surface defects, and derailment coefficient. Adopting the on-board monitoring methods is challenging due to the cost and difficulty of the sensor installation, implementation and maintenance of the sensors, and variety of trains and wheels. In addition, excluding the effect of rail defects from the measured data is a tough task. Furthermore, many research has been conducted in the simulation and/or test rigs level and field measurements were scarce. As a result, on-board monitoring as an aspect of wheel condition monitoring has had, and still has, many complications waiting to be overcome.

WAYSIDE METHODS

In-service wayside methods are the most common wheel monitoring systems. According to Table 2.3, the objectives of the wayside methods can be divided into two main groups: the wheel defect monitoring, and the train monitoring. The wheel defect data is directly used for estimating the wheel condition. The train monitoring extracts some features of the train that can be indirectly used in the further processing steps such as the number of axles, train velocity, and ambient Temperature.

In recent years, wheel-rail interaction and consequently wheel-rail deterioration have changed due to the increase of train velocities and axle loads. Hence, wear of the wheels as a dominant reason of their damage has been altered to fatigue [20]. This phenomenon shifts the defects from surface to sub-surface. Therefore, the wayside methods should be

adapted to this situation. According to Table 2.3, despite sufficient growth in surface defect detection using various techniques, sub-surface defect detection is still immature. Hence, developing wayside systems for monitoring sub-surface defects is an open issue. In addition, most of the methods deal with the severe defects and just a few methods investigate the minor defects.

According to Table 2.3, the strain-based WILDs have been considerably used for the wheel and train monitoring. The FBG strain sensors are wildly used in the commercial strain-based WILDs [13]. As mentioned in Subsection 2.3.4, the strain sensors have limited effective zone. Therefore, using multiple strain sensors for more coverage is common (see Subsections 2.3.5, and 2.3.6). The strain-based WILDs is mostly used for detection of the severe defects. Stratman et al. in [5] used this system to detect the sub-surface defects. As a results, the strain-based WILDs have considerable potential to be developed for the minor defect detection and identification. Tam et al. in [44] mentioned several advantages of FBG sensors for railway applications:

- Electromagnetic immunity; conventional strain gauges are affected by electromagnetic fields induced by high voltage power lines.
- Possiblity of fabricating numerous sensors inside a fibre;
- Long transmission distance due to less conduction loss;
- Innate ability for self-referencing; FBG interrogator measures the wavelength change, therefore the measured value is an absolute parameter;
- Resolving the recalibration or re-initialization problem
- Ability of using only one end of the fibre for interrogating the data.

Adding to these benefits, there are other factors cited in other literature such as:

- Immediate time response, reliability, durability [42];
- Small size, and independence from electric power in the measurement point [43];
- Low cost, easy installation [48];
- Great accuracy and sensitivity, stability in spite of ambient temperature change, corrosion resistance [49].

2.4.2. MEASUREMENT SPECIFICATIONS

For an accurate and reliable measurement, considering some settings during the measurement stage is necessary. The objective of the monitoring determines the measurement specifications. Most of the wheel CMSs are based on the wheel-rail interaction. The specifications of the rail, train and sensors influence the measurements. Some of these parameters are out of control such as train velocity, and axle load that also have significant effects on the measurement but most of the others can be set. Some examples of these specifications are listed below:

Table 2.3: The objectives of the wayside monitoring systems

Objective of monitoring	Technique or sensor	Assessment level
Surface defect detection	Strain gauges	Simulation [4]
		Field measurement [4], [5]
	Fibre Bragg Grating sensor	Field measurement [42], [43], [47], [48], [50]
	Ultrasonic technique	Simulation [31]
		Test rig [30], [31]
		Field measurement [30]
	Laser-Air Hybrid Ultrasonic Technique	Test rig [33]
	Vibration technique	Field measurement [11], [13], [38], [39]
	Acoustic technique	Simulation [34]
		Test rig [34], [35]
		Field measurement [34], [36]
Surface defect identification	Ultrasonic technique	Simulation [32]
		Test rig [32]
	Vibration technique	Field measurement [11]
Sub-surface defects	Strain gauges	Field measurement [5]
	Laser-Air Hybrid Ultrasonic Technique	Test rig [33]
Steering ability	Strain gauges	Field measurement [9], [41]
Derailment coefficient	Fibre Bragg Grating sensor	Field measurement [42], [45], [49]
	Piezoelectric Sensing Technology	Field measurement [51]
Wheel profile parameters	laser and high speed camera	Field measurement [41], [37]
Train velocity	Fibre Bragg Grating sensor	Field measurement [44], [47]
	Vibration technique	Field measurement [11]
Train acceleration	Fibre Bragg Grating sensor	Field measurement [47]
Number of axles	Fibre Bragg Grating sensor	Field measurement [46], [47]
	Vibration technique	Field measurement [11]
Dynamic load	Fibre Bragg Grating sensor	Field measurement [47], [48]
Static load (Weight of train)	Fibre Bragg Grating sensor	Field measurement [42], [48]
Train type identification	Fibre Bragg Grating sensor	Field measurement [47]
Ambient Temperature	Fibre Bragg Grating sensor	Field measurement [47]

- Rail: different properties and structures of tracks, including the types and profiles of rails, sleepers and ballast;
- Train: type, velocity, acceleration, deceleration, axle load, moving direction and wheel sizes;
- Sensor: the methods of installation, calibration factor, the measurement range of sensors, temperature change, sampling frequency, and the signal to noise ratio.

The on-board methods have several challenges such as sensor installation on the wheelset, and removing the traces of the rail defects from the measured data. In addition, the track properties such as vertical track stiffness have wide variation along the track [52] that is beyond the control.

For the wayside CMSs, different specifications were considered. For example, in [46] and [47] different positions were assessed to find the best one for installing the sensors. Their results showed that the maximum deflection would be on the head and foot of the rail in case of longitudinal sensor. The specifications of the wayside CMSs may be listed as follow:

- Uniform track structure with constant properties over the measurement section.
- Healthy track with no defect on the rail, sleeper, etc. over the measurement section.
- a straight and horizontal track for vertical force
- a curved track for measuring the flange contact and lateral force
- Constant train velocity over the sensors on each measurement. It can be changed from one measurement to another one.
- The wheel has a rotating movement without any sliding.
- The neighbor wheels have no influence of each other. It means just a single wheel is considered or just one wheel is defective.
- The sensors measure with high enough sampling frequency and high enough signal-to-noise ratio (SNR).

2.4.3. CONDITION ESTIMATION

A corrective maintenance policy needs to detect the severe defects to avoid further defects while for a preventive policy the minor defects should be detected and identified. Most of the wheel CMSs focused on the severe defects to eliminate their detrimental effects and the condition estimation stage has not been developed well.

Salzburger et al. in [30] exploited the ultrasonic technique to detect the surface and sub-surface cracks. Despite the good results, this method has a major difficulty in installing the sensors on the rail. In addition, the train velocity is restricted to 15 km/h. Brizuela et al. in [32] proposed an ultrasonic technique to estimate the length and depth of wheel flats. Belotti et al. in [11] applied the Wavelet Transform to quantify the flat size

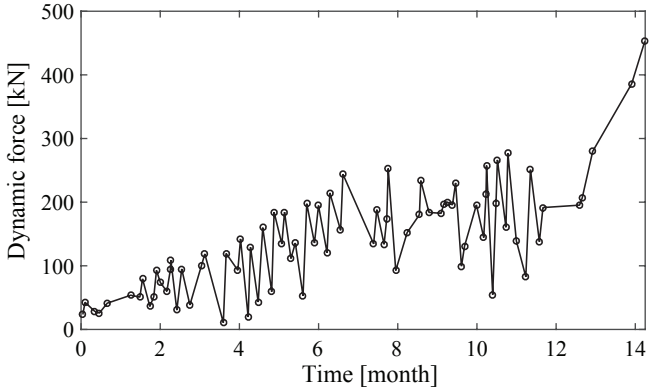

Figure 2.12: The evolution of the dynamic force of a defective wheel [5].

using the acceleration signals. Bracciali and Cascini in [38] quantified the defect severity by calculating the energy of the acceleration signal to detect flats and corrugations. Skarlatos et al. in [39] estimated the wheel condition as good, low damaged, faulty, and dangerous through a fuzzy-logic method using the the vibration magnitude, the centre frequency band, and the train velocity. They also applied this method for the wheel flats.

The contact force is a common method to quantify the wheel condition. WILDs use acceleration sensors or strain gauges to measure the contact force. The strain and acceleration signals need a transfer function and a calibration process to be converted to the force. The strain gauges have a limited effective zone that measures a small portion of the wheels, while the forces reconstructed from the acceleration signal have more coverage [40]. Therefore, the strain-base WILDs exploit multiple sensors and measure the contact force at several points to cover entire the wheels. In addition, the train velocity and axle load change the contact force measured [1], [4]. Therefore, the contact force could not be directly used as a wheel condition indicator. As a result, Stratman et al. in [5] defined two indicators, the dynamic force and the force ratio, to eliminate the effect of the axle loads (see section 2.3.5). Figure 2.12 presents the evolution of the dynamic force of a defective wheel. The contact force, the dynamic force, and the force ratio are usually used to classify the wheels into healthy and defective classes and have difficulty in detecting the minor defects and identifying the defect type [14].

Wei et al. in [43] proposed a condition index (C_I) based on the average of the strain changes ($\bar{\varepsilon}$) to estimate the overall condition of four wheels of a wagon. Figure 2.13 presents the progress of the condition index during ten months. The considerable decrease in condition index after 60th day is due to the wheel re-profiling. In [36] and [15] the train velocity, vibration frequency, and vibration magnitude are mentioned as the parameters of the condition index. The authors only compared the condition index obtained without discussing the relation between the parameters.

Diagnosis and prognosis are two key concepts in condition-based maintenance [15]. In the diagnostic aspect, the current condition is considered for maintenance decision

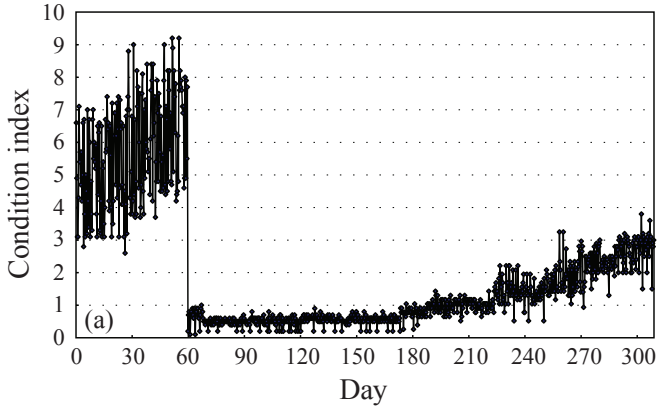

Figure 2.13: The evolution of the condition index obtained for the wheels of one side of a wagon over time. The reduction of the condition index is due to the maintenance [43].

making. When the condition exceeds a predetermined threshold, corrective activities are required. The prognostic approach detects deviations from the normal condition to predict the future condition and calculate the remaining useful life. In general, diagnosis is more common than prognosis, and this is also the case in the railway industry. All the papers reviewed here had the diagnostic aspect to defects, with the exception of [1], [5], and [43] that showed the evolution of wheel defects over time. To prevent the failure, developing a model to predict the future condition is also required.

2.5. CONCLUSION

To answer the first key question of "*What are the state-of-the-art technologies for estimating the wheel condition?*", this chapter has described the state-of-the-art methods for the wheel defect monitoring. The main conclusions of the literature analysis are reported here.

The defective wheels have detrimental effects on the components of tracks and vehicles. For this reason, the researchers have mostly focused on the severe defects such as wheel flats. The CMSs are useful when the defects grow over time. Therefore, from the wheel point of view, monitoring the wheel flat as an abrupt defect is just a corrective activity. To move from a corrective to a preventive policy, it is vital to detect the minor defects and identify the defect types.

The signals measured by the on-board sensors composed of wheel defects and track irregularities. Therefore, detecting and identifying the minor defects by means of the on-board methods are difficult. In addition, installing the sensors on every wheel is challenging and raises other issues such as cost and maintenance.

The wayside methods have wider applications and several commercial products have been developed. They can be installed on a healthy rail to only reflect the wheel condition. Despite the proper results of the WILDs, they have difficulty in detecting minor

defects and identifying the defect types. In addition, the train velocity and axle load influence the measurements. Moreover, the results have considerable variations and are not reliable and repeatable. As a result, in this dissertation we concentrate on the WILDs and aiming to develop an effective method for detecting and identifying the wheel defects by overcoming the drawbacks of the WILDs.

3

DATA FUSION PROCESS TO RECONSTRUCT WHEEL DEFECT SIGNAL[1]

Chapter 2 reviewed the state-of-the-art methods for the wheel condition monitoring. The strain-base WILDs are widespread systems currently used for the wheel defect detection. The strain sensors have a limited effective zone that leads to partial observation from the wheels. As a result, the WILDs usually use multiple sensors to collect multiple samples from different portions of the wheel. The discrete measurement misses the order and the pattern, and just provides the magnitude of the samples. Therefore, the much richer variation pattern of the samples is neglected. Therefore, this Chapter proposes a fusion method to associate the data collected by the multiple sensors. By associating the samples with their positions over the circumferential coordinate, a new informative signal is reconstructed that represents the wheel geometry and consequently the wheel defect. The fusion method can be applied at three different levels: data level, feature level, and at decision level [16]. This Chapter develops the fusion method at the data level to map the collected data over the circumferential coordinate.

Section 3.1 explains the configuration of the sensors and the corresponding issue of the partial observation. The space between the sensors causes a specific time lag between the signals measured. When the sensors have the same reference time to start the measurement, the time lag in the signals and space lag between the sensors can be related to each other. Therefore, Section 3.2 estimates the time lags to define the time and space relation between the collected data. Then, Section 3.3 proposes the sampling methods to determine the samples that should be selected from each signal as the output of each sensor. In Section 3.4, the fusion method is developed to reconstruct a signal over the circumferential coordinate using the collected samples. Consequently, the Section 3.5 estimates the train velocity to define the sampling frequency of the collected

[1] This Chapter is a revised version of Alemi et al. [53].

data in the space domain. Finally, Section 3.6 proposed a method to estimate the wheel circumference as the fundamental period of the defect signal.

3.1. SENSORS CONFIGURATION AND THE PARTIAL OBSERVATION PROBLEM

The wheel defects are not uniformly distributed along the wheel circumference. The non-uniform deterioration can be due to the material inhomogeneity [1], different operational conditions such as braking [54], [55], or environmental conditions such as humidity [56]. The wheel defects alter the contact patch that sometimes lead to multiple contact patches or loss of contact [57]. In addition, the degradation level of the wheels depend on their position on bogie and axle [8]. Hence, every wheel has its own degradation level that causes an individual wheel-rail contact force.

A wheel-rail contact force represents the geometric pattern of the wheel defect. The generated contact force is transferred to the track and vehicle. This force can be measured in both sides by installing a sensor on the wheel or on the rail. When a sensor is installed on the wheel, it can move with the wheel to continuously measure the wheel response to the contact force. Figure 3.1a presents the contact force signal measured by a strain gauge mounted on the wheel disc in a field experiment [58]. They measured the strain and converted that into the force. The signal shows three periods of the vertical contact force generated by three turns of a defective wheel with 40 mm flat. The distance between the highest peaks shows the wheel circumference. They did not report the diameter in that article but as stated by them in another paper [59], the wheel diameter was around 950 mm (2984 mm circumference). According to Figure 3.1a as a typical example, the 40 mm flat influenced around 20% of the contact force signal (around 600 mm) that we call the defective area. The rest of the signal is called the healthy area that covers 80% of the signal.

The sensor has three measurement zones with respect to the wheel. First, the inactive zone in which the wheel is away from the sensor, producing a zero output. Second, the transient zone in which the wheel approaches or leaves the sensor, with increasing or decreasing in the sensor output. Third, the effective zone in which the wheel is on top of the sensor. The sensors collect data in these measurement zones but only the data from the effective zone is used.

When the effective zone is smaller than the wheel circumference, the sensor makes a partial observation and only senses a limited portion of the wheel. Figure 3.1b, presents the track response for the same experiment measured by a sensor mounted on the sleeper (the rail support that is normally made from wood or concrete). In Figure 3.1a, the sensor sensed the defective area in three periods but the wayside sensor just sensed a portion of the second period and missed the others. In this example, the sensor properly sensed the defective area but it is not always the case. The position of the defective area with respect to the effective zone of the sensor is out of control and the length of the effective zone is smaller than the wheel circumference. Therefore, multiple sensors are commonly used to cover the wheel circumference [5].

The measured outputs of the multiple sensors are usable when they sample in identical situations to have an identical transfer function. Therefore, the sensors should be

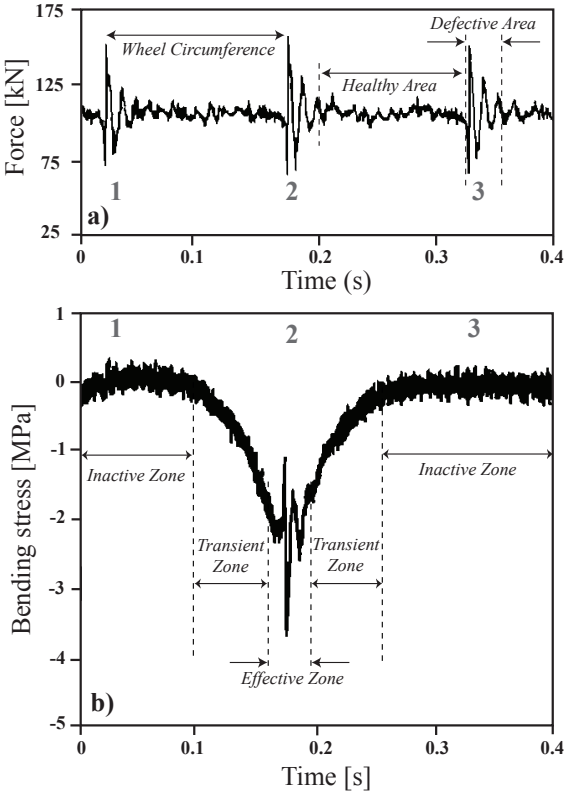

Figure 3.1: The vertical contact force measured by a sensor mounted on the wheel with 70 km/h velocity in a field test. Three rotations of a defective wheel with 40 mm flat shows a pattern with three periods b) Corresponding bending stress of sleeper measured in the effective zone of the sensor mounted on the sleeper [58].

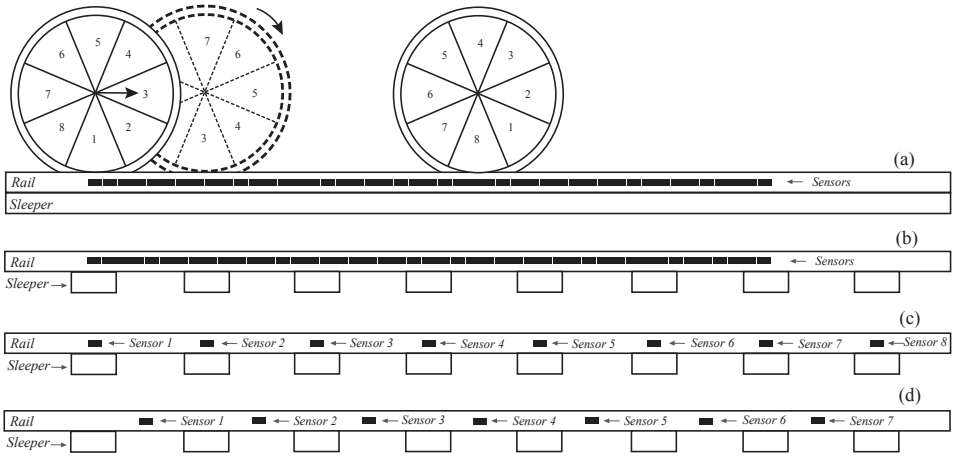

Figure 3.2: The configuration of the wheel, rail, sleepers, and sensors for a) a uniform track structure with joined sensors, b) the typical rail-sleeper structure with joined sensors, c) the typical structure with discrete sensors on the sleepers, d) the typical structure with discrete sensors between the sleepers.

mounted on a uniform track with a continuous structure. A schematic view of the sensors and the uniform track structure are illustrated in Figure 3.2a. This structure consists of a continuous sleeper that provides identical transfer function for the joined sensors. Integration of the discrete samples collected by different sensors gives the required contact signal over the circumferential coordinate.

Tracks with continuous sleepers are not common. In addition, creating a uniform track structure needs a dramatic change in the rail and sleeper structure. Therefore, a typical rail-sleeper structure is considered. The typical rail-sleeper structure (Figure 3.2b) causes dissimilar rail responses in different points along the rail. In this case, the outputs of the joined sensors have to be calibrated with respect to the sensor position in the longitudinal direction. To avoid this complexity, a symmetric structure of the sensors can be used. To configure this structure, the sensors should be mounted on the positions with an identical situation such as displayed in Figure 3.2c. This configuration assures that every measurement refers to a comparable rail and sleeper condition, and the only variable is the wheel condition. Figure 3.2d illustrates the sensor configuration in which the sensors are mounted between the sleepers.

Figure 3.3 shows the results of a field measurement [60] presenting the passage of four wheels by variation in the signals with four peaks. In this example, the third wheel had a 60 mm flat and the other wheels were healthy. Figure 3.3a shows the strain signal converted to the contact force. This signal was measured by strain sensors mounted in a sleeper bay like Figure 3.2d. Figure 3.3b shows the rail bending moment above the sleeper. The variation in the measured signal in Figure 3.3b is not as sharp as the signal in Figure 3.3a but clearly shows the passage of four wheels and the existence of the flat in the third wheel in 2.98 s. In Figures 3.3a and 3.3b, the third wheel exactly faced the sen-

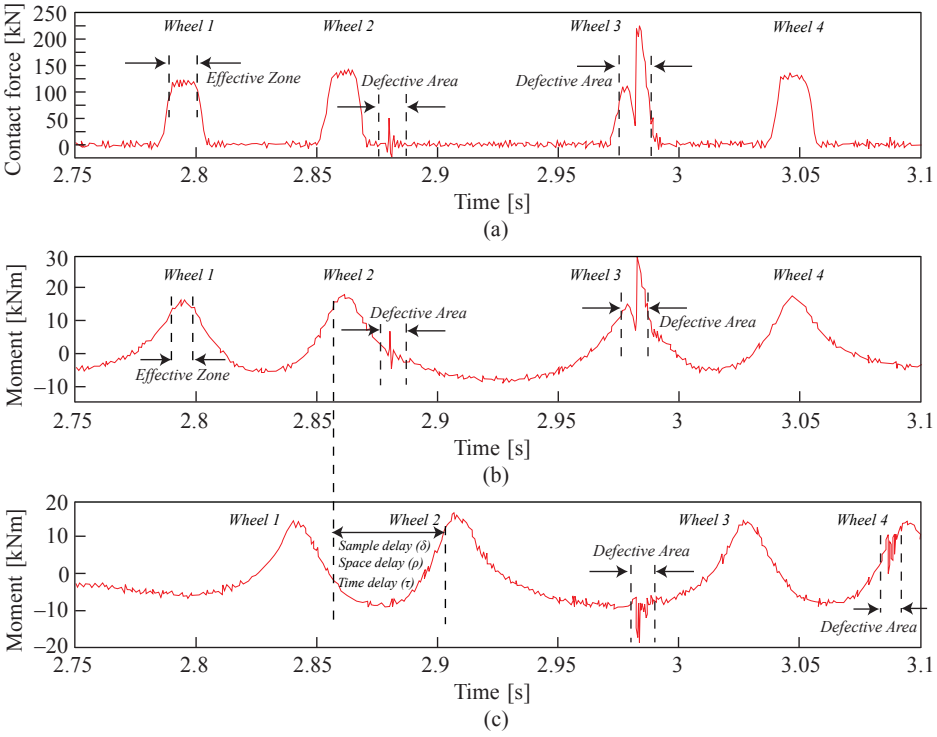

Figure 3.3: a) The vertical wheel–rail contact forces measured in a sleeper bay; b) rail bending moment above the sleeper; c) rail bending moment above a sleeper that was located two sleepers away [60].

sors with the flat part. Figure 3.3c shows the same wheels measured by another sensor, which was mounted on two sleepers away from the prior sensor in Figure 3.3b.

The defect of the third wheel obviously influenced the measured signal and generated a specific pattern with a downward and an upward deflection in the defective area. Regardless of the sensor type, the pattern of the defective area of the third wheel can be seen in both Figures 3.3a and 3.3b. This pattern was also sensed near the second wheel in 2.88 s in the inactive zone due to the previous turn of the wheel. In Figure 3.3c, the defective area of the third wheel was not sensed by the effective zone and appeared in the inactive zone in 2.98 s, and in the transfer zones in 3.09 s. The effective zone in Figure 3.3b gives 30 kNm for the third wheel, and the sensor in Figure 3.3c gives 15 kNm. By selecting only the magnitude of the signal as the representative output of the sensor, the pattern of the signal related to the wheel flat is neglected.

To reconstruct a signal over the circumferential coordinate, two sampling frequency should be considered carefully. First, the sensor sampling frequency (f_t) that is defined in the time domain. For example, 10 kHz sampling frequency means the sensor collects 10000 samples per each second. Second, the space sampling frequency (f_s) that is de-

fined in the space domain and determines the sampling frequency in the unit of space. Increasing the train velocity increases the distance between the collected samples and decreases the space sampling frequency. To have a signal over the circumferential coordinate, the sensors should sample from the wheel to the extent that the signal can be reconstructed using the data sampled. In Figure 3.2c, the distance between the sensors leads to discrete sampling from the wheel circumference. Therefore, in spite of the sufficient sensor sampling frequency (f_t), it is not possible to reconstruct a signal from the samples collected in this way.

According to the Nyquist sampling criterion, reconstructing the actual signal is perfectly possible when the sampling frequency (f_s) is at least twice the highest frequency contained in the signal (f_{max}), otherwise, it leads to aliasing [61]:

$$f_s > 2f_{max} \tag{3.1}$$

In accordance with the sensor configuration, the sleeper interval is a determining factor that defines the sensor intervals. In fact, only a limited number of samples from the wheel circumference can be collected on every wheel revolution. This sampling method leads to signal distortion (aliasing). The space sampling frequency is definitely far from the Nyquist frequency and therefore presents a new challenge for the sampling in the space domain.

3.2. LAG ESTIMATION BETWEEN THE SIGNALS

The patterns of the rail bending moment signal in Figures 3.3b and 3.3c are generally similar except only having a delay and some variations due to the wheel defect. The delay can be presented in three different ways: time delay (τ), space delay (ρ), and sample delay (δ). The time delay indicates the wheel travel time between two sensors (time dimension [s]). The space delay indicates the spatial turn of the wheel with respect to the prior sensor, which is equal to the sensor intervals (space dimension [m]). Finally, the sample delay shows the number of samples in the second signal that lagged behind the first signal (a number without dimension).

In this research, the measured signals in Figures 3.3b and 3.3c are modelled in the time domain as follow:

$$\begin{cases} z_1(t) = w(t) + g_1(t) + n_1(t), & \{t | t \in \mathbb{R}, 0 \le t \le T\} \quad (3.2a) \\ g_1(t) = w(t) \cdot g(t) & (3.2b) \end{cases}$$

$$\begin{cases} z_2(t) = w(t-\tau) + g_2(t) + n_2(t), & \{t | t \in \mathbb{R}, 0 \le t \le T\} \quad (3.3a) \\ g_2(t) = w(t-\tau) \cdot g(t) & (3.3b) \end{cases}$$

$z_1(t)$ and $z_2(t)$ are the signals measured by two consecutive sensors in the time domain. $w(t)$ is the signal generated by the wheel movement and contains low frequency components. This signal is a function of the axle load, and the train velocity, that we call it the wheel signal. Due to the sensor distance, and the wheel movement, the wheel signal $w(t)$ shifts over time and space. τ is the time delay between the signals $z_1(t)$ and $z_2(t)$, and the $n_1(t)$ and $n_2(t)$ are the uncorrelated noises. The signals are defined in the

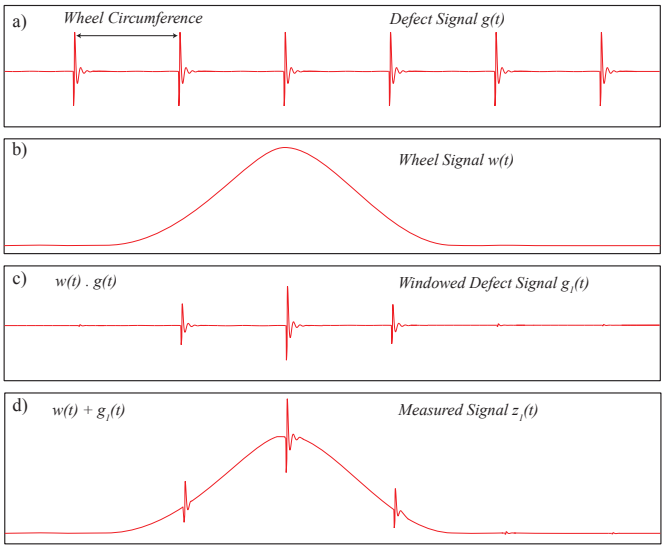

Figure 3.4: The schematic view of a) the defect signal $g(t)$; b) the wheel signal $w(t)$; c) the windowed defect signal $g_1(t)$, and d) the measured signal $z_1(t)$.

closed interval between zero reference time and T that is the measurement time. The time interval between each sample is $\frac{1}{f_t}$ second and the time delay between two signals is τ second.

$g(t)$ is the signal generated by the wheel defect and is a function of the defect geometry. The defect signal $g(t)$ is a periodic signal that is repeated on every wheel revolution. The sensors have a limited effective zone, therefore, they observe a limited portion of the defect signal. The wheel signal $w(t)$ operates as a window function that has almost a zero value outside the effective zone. Therefore, the product of the wheel signal $w(t)$ and the defect signal $g(t)$ generates a partial view of the defect signal. $g_1(t)$ is the partial view of the defect signal measured by the first sensor. This signal superimposes on the $w(t)$ and mostly contains high frequency components. As a result, $g_1(t)$ is also a function of the wheel signal. $g_2(t)$ is the partial view of the defect signal measured by the second sensor and is superimposed on $w(t-\tau)$. Figure 3.4 illustrates a schematic view of the wheel signal $w(t)$, the defect signal $g(t)$, the windowed defect signal $g_1(t)$, and the measured signal $z_1(t)$. Bear in mind that, this Chapter aims to reconstruct the defect signal $g(t)$, from the measured signals $z(t)$.

The measured signals can be also presented in the space domain as

$$\begin{cases} z_1(x) = w(x) + g_1(x) + n_1(x), & \{x | x \in \mathbb{R}, 0 \le x \le X\} \quad (3.4a) \\ g_1(x) = w(x) \cdot g(x) & (3.4b) \end{cases}$$

$$\begin{cases} z_2(x) = w(x-\rho) + g_2(x) + n_2(x), & \{x | x \in \mathbb{R}, 0 \le x \le X\} \quad (3.5a) \\ g_2(x) = w(x-\rho) \cdot g(x) & (3.5b) \end{cases}$$

$z_1(x)$, $z_2(x)$, $w(x)$, $g(x)$, $g_1(x)$,$g_2(x)$, $n_1(x)$, and $n_2(x)$ are the signals in the space domain. The signals are defined in the closed interval between zero reference place and X that is the length passed by the wheel over the sensors. The space interval between each sample is $\frac{1}{f_s}$ meter and the space delay between two signals is ρ meter.

The measured signals can be also presented without dimension as

$$\begin{cases} z_1(i) = w(i) + g_1(i) + n_1(i), & \{i | i \in \mathbb{Z}^+, 0 \le i \le I\} \quad (3.6a) \\ g_1(i) = w(i) \cdot g(i) & (3.6b) \end{cases}$$

$$\begin{cases} z_2(i) = w(i-\delta) + g_2(i) + n_2(i), & \{i | i \in \mathbb{Z}^+, 0 \le i \le I\} \quad (3.7a) \\ g_2(i) = w(i-\delta) \cdot g(i) & (3.7b) \end{cases}$$

The dimensionless signals are defined in the closed interval between first sample and I that is the length of signal. In this case, the delay between two signals is δ samples.

The delay between two signals such as $z_1(i)$ and $z_2(i)$ displayed in Figure 3.3, can be estimated by looking for the maximum cross-correlation between the signals [62]. The cross-correlation function can be calculated as follow:

$$R_{z_1 z_2}(\gamma) = \sum_{i=1}^{I-\gamma} z_1(i+\gamma) z_2(i), \qquad \gamma = 0, 1, 2, \ldots \quad (3.8)$$

The cross-correlation between the signals $R_{z_1 z_2}(\gamma)$ involves shifting one of the signals, and summing the multiplication of the two signals. Therefore, the cross-correlation is a function of the lag between the signals (γ). The lag γ that maximizes the cross-correlation value, presents the sample delay δ.

$$\delta = \arg\max_{\gamma} R_{z_1 z_2}(\gamma) \quad (3.9)$$

The space delay (ρ) is equal the space distance between two consecutive sensors that is a known value, but the time delay (τ), which is the time difference between the signals, should be estimated. The time delay (τ) can be calculated using the time interval between each sample ($\frac{1}{f_t}$), and the sample delay δ as follow:

$$\tau = \frac{1}{f_t} \times \delta \quad (3.10)$$

where τ is the time delay between two signals, f_t is the sampling frequency of the sensors in the time domain, and δ is the sample delay between two signals.

3.3. SAMPLING METHODS

The multiple sensors (M sensors) start sampling at the same time with an identical sampling frequency f_t. Therefore, each sensor measures $I = T \times f_t$ samples over T second. As a result, M sensors measure M signals that have equal length (I samples). These signals include the samples from inactive, transient and effective zones and generate a dataset as follow:

$$Z_{m,i} = \begin{pmatrix} z_{1,1} & z_{1,2} & \cdots & z_{1,I-1} & z_{1,I} \\ z_{2,1} & z_{2,2} & \cdots & z_{2,I-1} & z_{2,I} \\ \vdots & \vdots & \ddots & \vdots & \vdots \\ z_{M-1,1} & z_{M-1,2} & \cdots & z_{M-1,I-1} & z_{M-1,I} \\ z_{M,1} & z_{M,2} & \cdots & z_{M,I-1} & z_{M,I} \end{pmatrix} \begin{matrix} \{i | i \in \mathbb{Z}^+, 0 \leq i \leq I\} \\ \{m | m \in \mathbb{Z}^+, 0 \leq m \leq M\} \end{matrix} \tag{3.11}$$

Figure 3.5 illustrates a schematic view of the sensors configuration proposed in section 3.1, to explain the measurement zones and the required parameters. Figure 3.5a demonstrations the configuration of the wheel, rail, and the sensors that measure the rail response at different places. Figure 3.5b shows a schematic pattern of a defect signal $g(t)$. Figure 3.5c shows the inactive, transient and effective zones of the first sensor. In Figure 3.5d, the multiple sensors measure the rail response at different places. Each sensor makes a partial observation, like presented in Figure 3.1b. The sensors provide different outputs in their effective zone due to the defect signal. Every sensor collects multiple samples in the effective zone that is coming from a specific portion of the wheel circumference. These samples are the combination of the wheel signal $w(t)$ and the defect signal $g(t)$. The number of samples collected in the effective zone is identical in every sensor if the train passes the sensors with a constant velocity, and the sensors sample with an identical sampling frequency f_t. In Figure 3.5d, the sensors collect N samples in their effective zone.

The signals have similar patterns but with the δ delay. Therefore, the corresponding points of the signals in two consecutive sensors have the following relation:

$$z_{1,i} \mapsto z_{2,(i+\delta)} \tag{3.12}$$

It means that the sample i in the signal z_1 measured by the first sensor maps to sample $i+\delta$ in the second signal z_2. For example, when the i^{th} sample of the signal in Figure 3.3b is the representative sample of the second wheel, the $(i+\delta)^{th}$ sample will be the corresponding sample of the second wheel in Figure 3.3c. In general, when the sensors have equal space delay (ρ), and the wheel moves with the constant velocity, the relation between the corresponding points of the first signal to any other signal (measured by the sensor m) will be as follow:

$$z_{1,i} \mapsto z_{m,(i+(m-1)\times\delta)} \tag{3.13}$$

We use the samples of the effective zone. Therefore, when the multiple sensors (M sensors) collect multiple samples (N samples) from the passage of a wheel, we can gen-

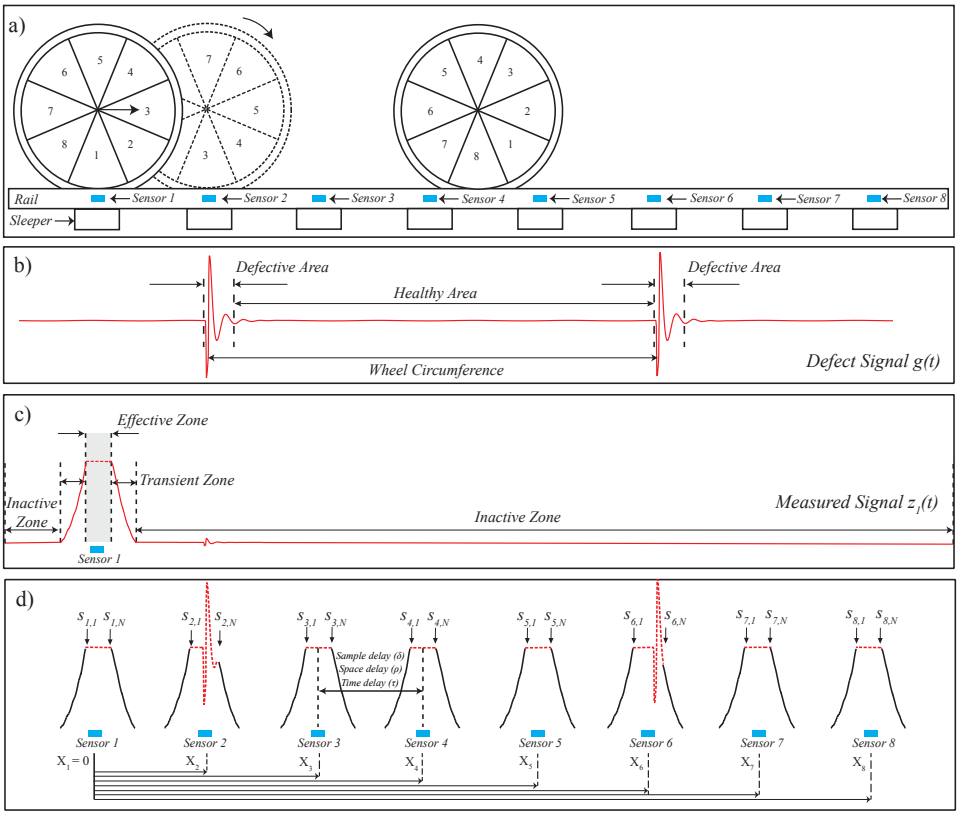

Figure 3.5: a) The configuration of the wheel, rail, sleepers and sensors, b) the defect signal, c) inactive, transient and effective zones of a sensor, and d) the multiple sensors that collect multiple samples in their effective zone.

erate the following dataset from the collected samples:

$$S_{m,n} = \begin{pmatrix} s_{1,1} & s_{1,2} & \cdots & s_{1,N-1} & s_{1,N} \\ s_{2,1} & s_{2,2} & \cdots & s_{2,N-1} & s_{2,N} \\ \vdots & \vdots & \ddots & \vdots & \vdots \\ s_{M-1,1} & s_{M-1,2} & \cdots & s_{M-1,N-1} & s_{M-1,N} \\ s_{M,1} & s_{M,2} & \cdots & s_{M,N-1} & s_{M,N} \end{pmatrix} \begin{cases} \{n | n \in \mathbb{Z}^+, 1 \leq n \leq N\} \\ \{m | m \in \mathbb{Z}^+, 1 \leq m \leq M\} \\ S_{m,n} \subseteq Z_{m,i} \end{cases} \tag{3.14}$$

In this dataset, each row presents the samples of the effective zone collected by each sensor. The space distance between the samples of each column (distance between the identical samples collected by two consecutive sensors e.g., $s_{1,1}$ and $s_{2,1}$), is equal the space distance between the sensors (ρ) that is a known value. Therefore, the space distance of the sensors defines the space distance between the samples of each column.

3.4. DATA FUSION AND SIGNAL RECONSTRUCTION

The sensors collect a few samples on every wheel revolution (as presented in Figure 3.5). The sampling frequency in the space domain f_s obviously violates the Nyquist criterion by subsampling lower than the fundamental frequency of the signal in the space domain. To respond to the Nyquist sampling challenge, the nature of the defect signal gives a hint. As can be observed from Figure 3.1a, the defect signal is a periodic signal that is replicated in every wheel revolution. The distances between the main peaks in Figure3.1a indicate the wheel circumference that is the fundamental period of the signal. The samples selected from different sensors can be mapped over the circumferential coordinate using the wheel circumference and the sensors configuration. Figure 3.6 presents a schematic illustration of the mapping process, in which X_m is the space position of the sensors, L_w is the wheel circumference length, and Y_m is the corresponding position of the sensors over the circumferential coordinate.

In Figure 3.6, sensors 1-5 sample from the first revolution, and the sensors 6-8 sample from the second revolution. Y_m determines the position of the sensors 6-8 over the wheel circumference. The samples collected by sensors 6-8 fill the gaps between the sensors 1-5 and improve the quality of the signal. By extending the sampling procedure to the other turns, more samples from different portions of the wheel are collected to fill the missing data. When the sample/cycle ratio is not an integer quantity, other replications of the wheel revolution collect supplementary samples. Instead, this method will sample multiple times the same points when the circumference is 3000 mm (954.9 mm diameter) with 600 mm sensor interval. In this case increasing the number of sensors is not useful for collecting the missing data. By bearing in mind the range of the wheel diameter between 840-920 mm [63], and assuming the 600 mm sensor interval, the number of sampling from the wheel revolution, will be 4.39-4.81 times per wheel revolution. Hence, increasing the number of sensors improves the signal quality.

3.4.1. DATA FUSION FOR SINGLE SAMPLING METHOD

In this subsection, only a single sample is used as the output of each sensor that is called Single Sampling Method (*SSM*). By selecting the sample $s_{1,1}$ as the output of the first sensor for the wheel, the sample $s_{2,1}$ will be the output of the second sensor for the wheel

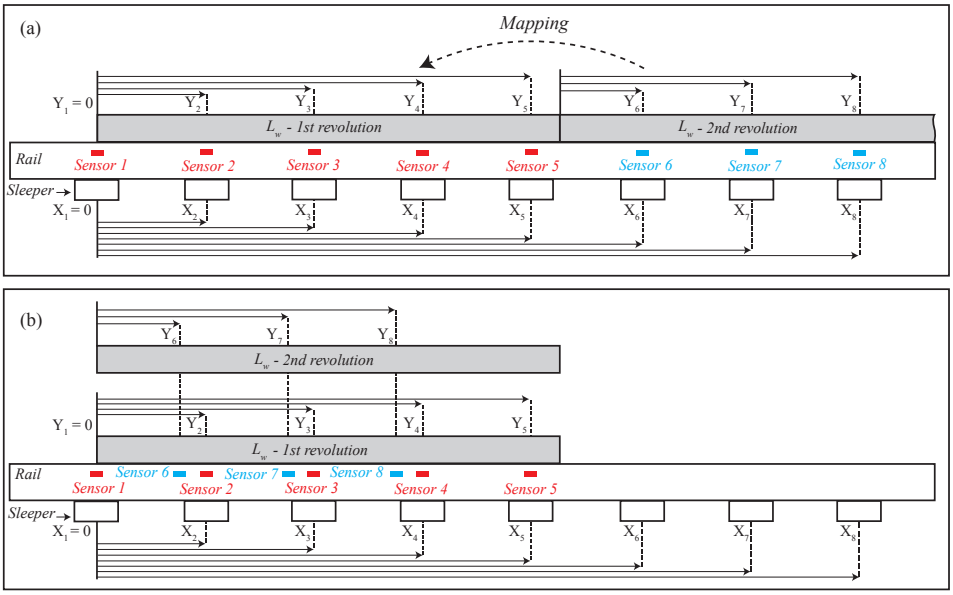

Figure 3.6: The illustration of the fusion process.

that measures another point of the wheel with ρ distance in the space domain. As a result, a set of samples as the output of different sensors for the wheel are acquired as follow:

$$S_{m,1} = \begin{bmatrix} s_{1,1} \\ s_{2,1} \\ \vdots \\ s_{M-1,1} \\ s_{M,1} \end{bmatrix} \qquad \begin{cases} \{n = 1\} \\ \{m | m \in \mathbb{Z}^+, 1 \leq m \leq M\} \end{cases} \tag{3.15}$$

The samples of the sub-dataset ($S_{m,1}$) can be fused over the circumferential coordinate to generate a signal for the wheel using the following Equation:

$$Y_{m,n} = X_m - (L_w \times \lfloor \frac{X_m}{L_w} \rfloor) \qquad \begin{cases} \{n = 1\} \\ \{m | m \in \mathbb{Z}^+, 1 \leq m \leq M\} \end{cases} \tag{3.16}$$

where Y_m is the corresponding position of the samples over the circumferential coordinate, X_m is the space position of the sensors, L_w is the wheel circumference length, and $\lfloor \, \rfloor$ is the round operator toward the nearest integer less than or equal to the element. The remainder after division of the sensor position by the circumference length determines the sensor position on the circumferential coordinate. A new signal (ψ_s) is generated using the magnitude ($S_{m,1}$) and the position ($Y_{m,1}$) of the samples as follow:

$$\psi_s = [Y_{m,1}, S_{m,1}] \tag{3.17}$$

The signal (ψ_s) reconstructed by SSM has M samples over the circumferential coordinate.

3.4.2. DATA FUSION FOR MULTIPLE SAMPLING METHOD

In this subsection, Multiple Sampling Method (MSM) uses all the data collected in the effective zone. To do this the space distance between the samples of each row (λ) should be estimated. For example the space distance between $s_{1,1}$ and $s_{1,2}$ is required. When the first sample of a sensor is positioned over the circumferential coordinate, the other samples collected by the sensor in the effective zone have the following positions:

$$Y_{m,n} = Y_{m,1} + ((n-1) \times \lambda) \qquad \begin{cases} \{n | n \in \mathbb{Z}^+, 1 \leq n \leq N\} \\ \{m | n \in \mathbb{Z}^+, 1 \leq m \leq M\} \end{cases} \tag{3.18}$$

Then the multiple samples (N samples) measured by the sensors are positioned using the space distance between the samples (λ). As a result, the reconstructed signal (ψ_s) is generated using the magnitude ($S_{m,n}$) and the position ($Y_{m,n}$) of the samples:

$$\psi_s = [Y_{m,n}, S_{m,n}] \tag{3.19}$$

The MSM reconstructs the signal (ψ_s) by $M \times N$ samples. Intuitively, these samples are not uniformly distributed over the circumferential coordinate.

The sampling frequency of a sensor determines the time interval between the samples collected by the sensors. By considering the constant sampling frequency in the time domain, the train velocity determines the space frequency (space distance) of the samples collected by the sensor. The space interval between the samples can be defined using the space delay ρ and the samples delay δ as follow:

$$\lambda = \frac{\rho}{\delta} \tag{3.20}$$

This relation can be rewritten based on the train velocity V, and the sensor sampling frequency f_t as the influential factors as

$$\lambda = \frac{V}{f_t} \tag{3.21}$$

The space distance between the samples (λ) determines the space resolution of the measurement in the space domain. For example, when a sensor is sensing by 10 kHz sampling frequency, for a train with 10 m/s velocity, the space distance between the samples is 1 mm. In addition, the sensors have a limited effective zone. Therefore, the number of samples that can be used as the outputs of the sensors, is determined by the space distance between the samples (λ), and the length of the effective zone (L_e) as presented below:

$$N = \frac{L_e}{\lambda} \tag{3.22}$$

To determine the space distance between the samples (λ), the space delay (ρ) and the samples delay (δ) can be directly used as presented in Equation 3.20. Moreover, the train velocity can be indirectly used in 3.21 that is estimated in the next section.

3.5. TRAIN VELOCITY ESTIMATION

Filograno et al. in [47] and Tam et al. in [44] estimated the train velocity using the passage time between two axles. To find the axle distance, they counted the axle numbers and compared with the known information of different trains to identify the train type, and the matching axle distance. This method uses only one sensor but relies on the other information about the trains that should be provided from other sources. Here, we estimate the train velocity using the multiple sensors that not requires identifying the train type. The velocity is the space passed over the unit of time. Accordingly, the train velocity can be estimated using the space delay and the time delay as

$$V = \frac{\rho}{\delta} \times f_t \tag{3.23}$$

where ρ and f_t are the known values and the sample delay (δ) is estimated by the cross-correlation in Equations 3.8 and 3.9.

3.6. WHEEL CIRCUMFERENCE ESTIMATION

In Equation 3.16, the sensor position (X_m) is a known value, but the wheel circumference length (L_w) should be determined from other sources or should be estimated directly from the collected data. The circumference estimation method is based on an assumption that the defect signal has a single defective area that contains high frequency components. The defective area is sampled by different sensors with delay. The fusion process should reconstruct the defect signal and put the samples of the defective area in the right order.

The process for estimating the length of the wheel circumference (L_w) for Multiple Sampling Method (MSM) and Single Sampling Method (SSM) is the same. This process can be carried out for each set of data. First, the samples of defective area are selected by assessing the deviation of the collected samples from their average. Second, the possible range of the circumferences is swept to determine the order of the defective area samples over the circumferential coordinate. The actual circumference arranges the defective area samples in the sequence.

Here, we consider the first column of the dataset 3.14, $S_{m,1}$, $m = 1,2,3,\ldots,M$. The samples of this subset can be separated into two groups: the samples from the defective area and the samples from the healthy area. The samples show a major variation with respect to the average (μ_s) that are the samples from the defective area ($S^1_{m,n}$), and the other samples that are approximately equal to the average of the samples that are the samples from the healthy area ($S^2_{m,n}$). The deviation from the average value is due to the defect or the measurement noise. The average and the standard deviation of the samples are calculated as

$$\mu_s = \frac{1}{M}\sum_{m=1}^{M} S_{m,n} \qquad \begin{cases} \{n | n \in \mathbb{Z}^+, 1 \le n \le N\} \\ \{m | m \in \mathbb{Z}^+, 1 \le m \le M\} \end{cases} \tag{3.24}$$

$$\sigma_s = \sqrt{\frac{1}{M}\sum_{m=1}^{M} (S_{m,n} - \mu_s)^2)} \qquad \begin{cases} \{n | n \in \mathbb{Z}^+, 1 \le n \le N\} \\ \{m | m \in \mathbb{Z}^+, 1 \le m \le M\} \end{cases} \tag{3.25}$$

The samples can be separated by defining a threshold as follow:

$$T_U = \mu_s + (C_f \times \sigma_s) \tag{3.26a}$$

$$T_L = \mu_s - (C_f \times \sigma_s) \tag{3.26b}$$

where T_U is the upper threshold and T_L is the lower threshold. C_f is the filter coefficient that is an absolute number between [2,2.8].

$$S_{m,1} \in S^1_{m,n} \quad if: \begin{cases} S_{m,1} > T_U \\ \quad or \\ S_{m,1} < T_L \end{cases} \quad \{m|m \in \mathbb{Z}^+, 1 \le m \le M\} \tag{3.27a}$$

$$S_{m,1} \in S^2_{m,n} \quad if: \begin{cases} S_{m,1} \le T_U \\ \quad and \\ S_{m,1} \ge T_L \end{cases} \quad \{m|m \in \mathbb{Z}^+, 1 \le m \le M\} \tag{3.27b}$$

$$S^1_{m,n} \cup S^2_{m,n} = S_{m,1} \tag{3.27c}$$

According to the definition of the standard deviation, 99.7% of the collected samples are distributed in [-3σ_s + 3σ_s]. When the filter coefficient is a very small, the noisy samples in the healthy area will not be filtered out. However, a very large filter coefficient filters out the samples from the defective area.

Figure 3.7 illustrates a schematic example of the samples collected by 150 sensors with the measurement noise. This figure presents the collected samples, marks the sample from the defective area, and draws the filter threshold of $2\sigma_s$ as the minimum threshold, and the filter threshold $2.8\sigma_s$ as the maximum threshold.

Intuitively, the samples from the defective area should be in a sequence and close to each other over the circumferential coordinate, but the proposed sensor configuration collects the samples in the different wheel revolutions and with a space between the samples. According to the range of the wheel diameter that is between 840-920 mm [63], the collected samples can be differently mapped over the wheel circumference. By sweeping the wheel range, the collected samples can be mapped differently to reconstruct signals.

In this research, the filter coefficient (C_f) has a range between [2,2.8] that can be optimized later. Depending on the interval between the filter coefficients (for example 0.1), several filter coefficients are determined (in this case $C = 9$ values). By sweeping the range of the filter coefficient, different number of samples are selected as the defective area for each coefficient (N^t). For example in Figure 3.7, $C_f = 2.8$ gives 3 samples as the defective area samples and $C_f = 2$ gives 8 samples. Then, by sweeping the range of the wheel circumference, the defective area samples are mapped over the circumferential coordinate with different sequence. To find the most probable wheel circumference, the ratio of the number of defective area samples that mapped in the sequential order (N^s) to the total number of the defective area samples (N^t) in that set is calculated:

$$r_{k,c} = \frac{N^s_{k,c}}{N^t_{k,c}} \qquad \begin{cases} \{c|c \in \mathbb{Z}^+, 1 \le c \le C\} \\ \{k|k \in \mathbb{R}, 840 \le k \le 920\} \end{cases} \tag{3.28}$$

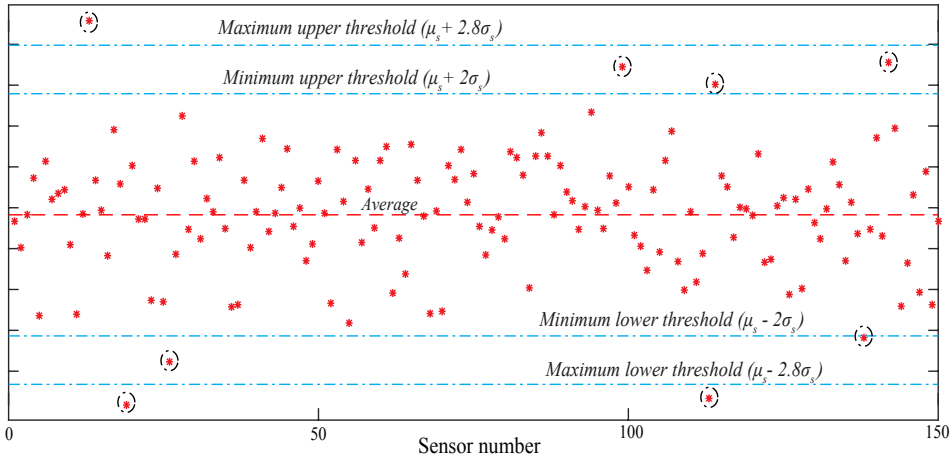

Figure 3.7: The relation of the thresholds and the samples to assign the samples to the defective area and the healthy area.

The wheel circumference which provides the maximum value for $r_{k,c}$ is considered as the most probable answer. When the most likely circumferences are in a continuous range, the average of this range is selected as the wheel circumference. For example, when the output of the algorithm is three estimates for the wheel circumference, 2980, 2981, 2982 mm, the average of these values (2981 mm) is selected. However, when multiple circumferences are possible in a series of non-continuous ranges, then the average of each range is considered as a possible circumference. When the sensors sense no samples or only one sample from the defective area, this method is not applicable.

3.7. CONCLUSION

The magnitude of the contact force contains a limited piece of information about the wheel defect. Therefore, this Chapter proposed a fusion method to reconstruct a signal containing the pattern of the contact force. To answer the key question of "*How can the data collected by multiple sensors mounted along the rail be fused to reconstruct a new informative signal?*", this chapter has developed the required fusion method and filled the gap. The multiple sensors collect multiple samples from different portions of the wheel. The fusion method associates these samples to reconstruct a signal over the circumferential coordinate in the space domain. The fusion method needs the train velocity and the wheel circumference, so two methods were developed to provide the required data. The next Chapter investigates the influential parameters contributing to fusion process and the effectiveness of using the reconstructed signals to estimate the wheel condition will be investigated in Chapter 5.

4

EVALUATION OF INFLUENTIAL PARAMETERS CONTRIBUTING TO FUSION PROCESS[1]

Chapter 3 has developed the fundamental theory of the fusion method and explained the required steps with their corresponding inputs and outputs. This process should handle the operational range of each variable. Therefore, this chapter evaluates the variation of the reconstructed signals as the outputs of the fusion process to the variation of the influential parameters. The output of the fusion process is influenced by several parameters that can be categorized into two main groups. Some of the parameters affect the contact force signal and consequently the input of the fusion process, such as the train velocity, axle load, and defect type. Few other parameters change the performance of the fusion method, such as the number of sensors, length of the effective zone, and the wheel circumference as the fundamental period of the defect signal.

To evaluate the effect of the influential parameters, a detailed parametric study is carried out. Figure 4.1 presents the procedure of the parametric study. The fusion model has been explained in Chapter 3. The input of the fusion process is the data modelled by VI-Rail, which is a multi-body dynamics software. VI-Rail simulates the data that will be provided in practice by multiple sensors. Then, the generated data is exported to MATLAB as the input of the fusion process. Section 4.1 explains the procedure of the data generation using VI-Rail. Section 4.2 defines some indicators to assess the variation of the reconstructed signals. Section 4.3 presents and discusses the results of the parametric study. To have a detailed insight about the effects of the parameters, this research investigates the trends of the indicators than the exact value obtained.

[1] This Chapter is a partially based on Alemi et al. [64].

Figure 4.1: The procedure of the parametric study.

4.1. SIMULATION PROCEDURE TO GENERATE DATA BY VI-RAIL

VI-Rail is an ad-hoc railway simulation software that has been built upon MSC Adams. Since VI-Rail is a commercial multi-body dynamics software and TU Delft has a licence, this software is used to model the dynamic behaviour of the rail and the defective wheel to generate the required data. This software models the interaction of the track and vehicle by considering their subsystems such as car body, sleepers, rail pads, wheelsets, primary and secondary suspensions, dampers, and anti-roll bars.

Figure 4.2 illustrates the procedure of the data generation using VI-Rail. In the first step, the defect model generates the defect on the wheel. Then, using the required parameters, VI-Rail models the wheel-rail interaction and generates some outputs. In the subsection 4.1.1, the defect model is presented. Subsection 4.1.2 explains the wheel-rail dynamics model, and subsection 4.1.3 describes the output of the data generation process.

4.1.1. DEFECT MODEL

A precise defect model defines the size, shape, and the position of the defect on the wheel profile and on the wheel circumference. Nielsen and Johansson in [1] classified and reviewed the wheel defects and discussed the reasons of their development. Table 4.1 presents the features and the positions of the common defects measured or simulated in literature.

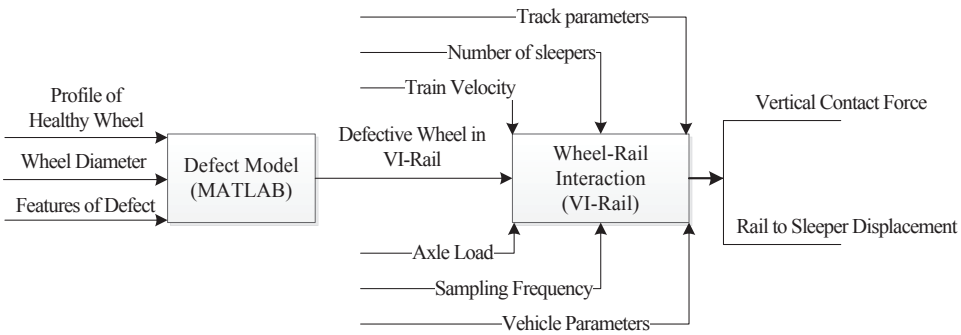

Figure 4.2: The procedure of the data generation by VI-Rail.

Table 4.1: Descriptions of the common wheel defects.

Defect	**Position on profile**	**Position on circumference**	**Features**
Eccentricities	Entire	Entire	One harmonics around wheel circumference, 0.1-0.3 mm amplitude [1]
Periodic non-roundness (polygonal)	Entire	Entire	Wavelength from 140 mm to one wheel circumference, (one to ten harmonics around the wheel circumference) with 1 mm amplitude [1] 0.3 mm amplitude [65] 1–5 harmonics around the wheel circumference with 1 mm amplitude [60]
Non-periodic (stochastic)	Entire	Entire	The stochastic shape contains several different harmonics with 0.3 mm amplitude [1]
Corrugation	over a part	Entire	Wavelength from 30-60 mm with the amplitude smaller than 0.01 mm [1] Wavelengths from 30–70 mm with 0.4 mm amplitude [65]
Roughness	over a part	Entire	Wavelength around 1 mm with 0.01 mm amplitude [1] Wavelengths from 10 mm to 200 mm with amplitude varies from 0.001 mm to 0.1 mm respectively [66] Wavelength from 50-70 mm with 0.01 mm amplitude [60]
Flat	over a part	over a part	15-45 mm length [11] 40 mm length and 0.25-0.35 mm depth [58] 40-100 mm length and 0.3-1.4 mm depth [4] 150 mm length and 2.15 mm depth [67] 100 mm length and 0.9 mm depth [68] Up to 60 mm length and 40 mm width [69]
Spalling	over a part	over a part	To 25 mm in length and width [70] Flaws and pitting up to 12 mm diameter up to 10% wheel coverage. Up to 25 mm diameter, up to 20% wheel coverage. Up to 25 mm diameter, up to 50% wheel coverage. Up to 25 mm diameter, 3 mm or more depth, greater than 50% wheel coverage [71]
Shelling	over a part	over a part	4–5 mm depth [72] Greater than 5 mm length [73] Combination of crack size with 2.7-5.6 mm width, 2.1-10.2 mm length, and 0.1-0.6 mm depth [74]
Discrete defect	Entire	over a part	A deviation of the wheel radius over a part of the circumference [1]

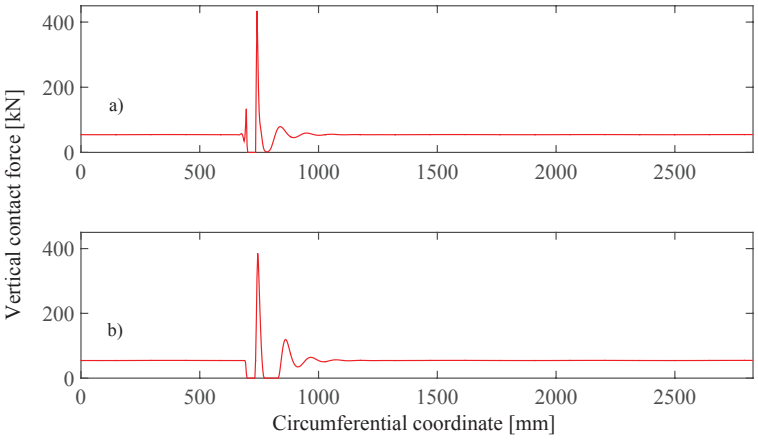

Figure 4.3: The vertical contact force generated for a 40 mm flat and 30 m/s velocity by a) radius reduction entire the wheel profile, and b) radius reduction in the contact area.

Wheel flats are the severe defects that cause high impact forces. The impact loads have positive correlation with the length and depth of the wheel flat [60]. The impact load and the flat length are common criteria for detecting the defective wheels. According to the Swedish criterion the wheels with 40-60 mm flat length should be re-profiled as detected during visual inspections [4]. Furthermore, a 60 mm flat triggers the high impact load alarm [14]. Hence, in this research 60 mm is the maximum length of a flat.

Spalling is the most common defect [14] [6] caused by Rolling Contact Fatigue (RCF). According to [71], the maximum spalling size is around 25 mm hence, for modelling the spalling, squares with 30 mm side length and smaller are considered. Spalling and flat are the defects that influence a part of the wheel profile. Unfortunately, the positions of the defects on the wheel profile have not been reported. A set of ultrasonic inspections in [75] shows that the RCF defects are usually between 75-105 mm from the back side of the wheel. These points are the nominal contact region. For this reason, the defects are implemented there.

To model a flat, the first approach is the constant radius reduction entire the wheel profile. The second approach is the radius reduction in the contact area and leaving the flange. Figure 4.3 presents the vertical contact force generated by these two models for a 40 mm flat and 30 m/s velocity. Generally, these models give similar outputs. In these two models, the length and depth (the radius variation) of the flat is identical in the nominal contact point, and the difference is the depth of the other points in the width direction. According to the purpose of this parametric study, each of these models can be used to represent a wheel flat. In this study, we model the flat using the second approach.

In VI-Rail, a wheel is defined by a set of profiles in different rotation angles. It means that an identical profile along the circumference $(0-2\pi)$ creates a healthy wheel that has a uniform and smooth surface. Hence, for defining a defect on the wheel surface,

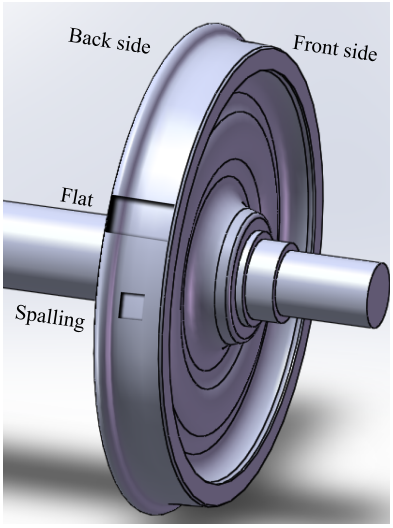

Figure 4.4: The illustration of a S1002 wheel with a spalling and a flat defect.

depending on the defect feature, several profiles should be used to construct the defect. Figure 4.4 illustrates a schematic view of a flat and a spalling defect on the wheel surface.

In order to have the same number of points over the wheel profile, VI-Rail interpolates each profile. Then it creates one spline from each point on the profile to the corresponding points on other profiles. This spline will have $0-2\pi$ radians rotation as an independent variable over the wheel circumference. During the simulation for a given rotation step, it generates a slice between two profiles while each point obtained from interpolating one spline at the given rotation [76].

A periodic out of roundness (OOR) covers entire the wheel profile and the circumference. Therefore, to model an OOR, the wheel diameter is varied according to the defect shape. Figure 4.5 presents the radius variation of the wheel over the wheel circumference for a 3rd order OOR. In the course of time, the primary shapes of spalling [55] and flat [60] fade away and alter to a long non-roundness. Therefore, modelling the discrete long non-roundness as a potential defect can be useful but for simplification, the discrete long non-roundness and other defects are not taken into account.

4.1.2. WHEEL-RAIL DYNAMICS MODEL

The simulations are carried out for a passenger vehicle based on the Manchester Benchmarks [77]. The assembly model consists of a vehicle and a flexible track. The vehicle is one wagon composed of a car body and two bogies that each of them has four S1002 wheels. The main parameters of the vehicle model in the Manchester Benchmarks are presented in Table 4.2.

The flexible track contains a straight UIC60 rail. The schematic view of the flexible track structure is displayed in Figure 4.6. In this model the rail mass and the inertia prop-

Table 4.2: The vehicle parameters based on the Manchester Benchmarks

Subsystem	Parameter	Value	Unit
Wheelsets	Mass	1813	kg
	Roll inertia (I_{xx})	1120	kgm^2
	Pitch inertia (I_{yy})	112	kgm^2
	Yaw inertia (I_{zz})	1120	kgm^2
Bogies	Mass	2615	kg
	Roll inertia (I_{xx})	1722	kgm^2
	Pitch inertia (I_{yy})	1476	kgm^2
	Yaw inertia (I_{zz})	3067	kgm^2
Body	Mass	32000	kg
	Roll inertia (I_{xx})	56800	kgm^2
	Pitch inertia (I_{yy})	1970000	kgm^2
	Yaw inertia (I_{zz})	1970000	kgm^2
Primary suspension	Longitudinal stiffness	31391	kN/m
	Nominal damping in parallel	15	kNs/m
	Damping series stiffness	60000	kN/m
	Lateral stiffness	3884	kN/m
	Nominal damping in parallel	2	kNs/m
	Damping series stiffness	7500	kN/m
	Vertical stiffness	1220	kN/m
Secondary suspension	Longitudinal shear stiffness	160	kN/m
	Lateral shear stiffness	160	kN/m
	Vertical stiffness	430	kN/m
Primary vertical dampers	Damping rate	4	kNs/m
	Series stiffness	1000	kN/m
Secondary lateral dampers	Damping rate	32	kNs/m
	Series stiffness	6000	kN/m
Secondary vertical dampers	Damping rate	20	kNs/m
	Series stiffness	6000	kN/m

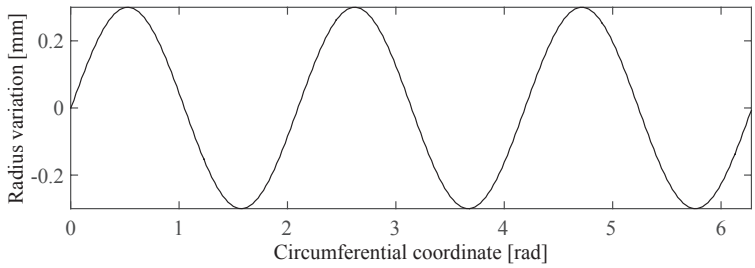

Figure 4.5: The radius variation over the wheel circumference for a third order OOR with 0.3 mm amplitude.

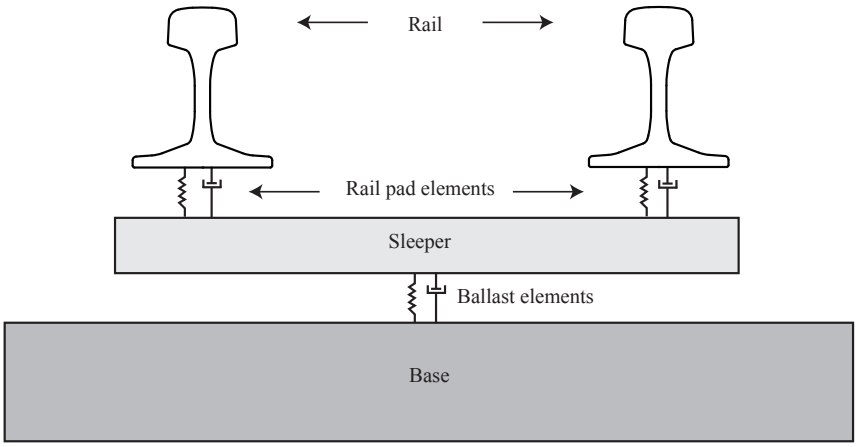

Figure 4.6: The schematic front view of the flexible track structure.

erties are concentrated on each rail sleeper [78]. Table 4.3 presents the track parameters used in the simulations. The detailed explanation of the track and vehicle structure falls outside the scope of this manuscript.

4.1.3. OUTPUT OF THE DATA GENERATION PROCESS

VI-Rail provides a range of outputs such as the contact force, rail and sleeper acceleration, and rail and sleeper displacement. The primary desired output is the rail strain that is commercially used in practice, but VI-Rail could not provide the rail strain signal. One approach is coupling the outputs of VI-Rail to a Finite Element Model to calculate the corresponding rail strain. The second approach is using the available data. By considering the rail as a transducer, the contact force signal is transformed into the rail response such as strain, acceleration and displacement. In this research due to lack of strain sig-

Table 4.3: The track parameters based on the Manchester Benchmarks

Subsystem	Parameter	Value	Unit
Rail pad right	Vertical stiffness	50	MN/m
	Lateral stiffness	43	MN/m
	Roll Stiffness	10	MN/rad
	Vertical damping	200	kNs/m
	Lateral damping	240	kNs/m
	Roll damping	10	kNs/rad
Rail pad left	Vertical stiffness	50	MN/m
	Lateral stiffness	43	MN/m
	Roll Stiffness	10	MN/rad
	Vertical damping	200	kNs/m
	Lateral damping	240	kNs/m
	Roll damping	10	kNs/rad
Ballast	Vertical stiffness	1000	MN/m
	Lateral stiffness	37	MN/m
	Roll Stiffness	10	MN/rad
	Vertical damping	1000	kNs/m
	Lateral damping	240	kNs/m
	Roll damping	10	kNs/rad

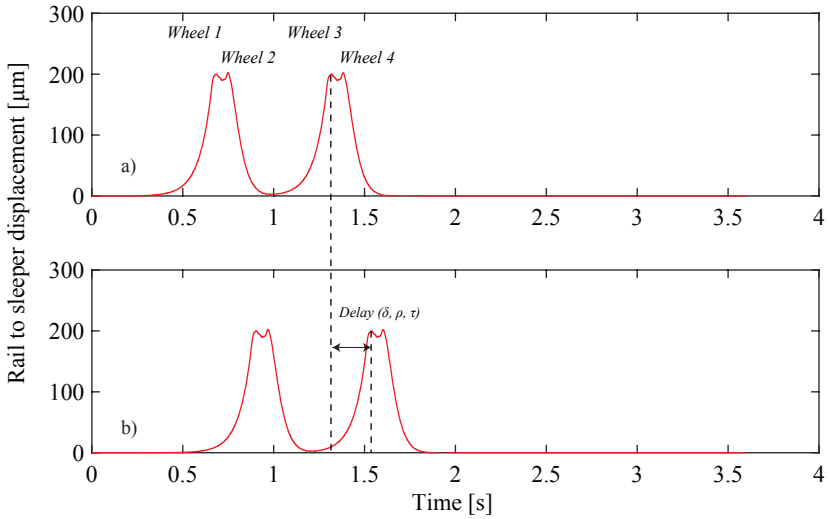

Figure 4.7: The typical simulated rail to sleeper displacement signals for two consecutive sleepers.

nal, the vertical rail to sleeper displacement is used as the output of the data generation process that is the input of the fusion model. Every sleeper is considered as a sensor that measures the rail to sleeper displacement signal. The sleepers have a discrete and periodic configuration like the sensors configuration.

Figure 4.7 displays typical rail to sleeper displacement signals for two consecutive sleepers simulated by VI-Rail. These signals show the variation in the vertical rail to sleeper position sensed in one side of the sleeper. They have four peaks representing the passage of a wagon with four healthy wheels in that side of track. Figure 4.7b shows a delay due to the distance between the sleepers.

Figure 4.8 displays the displacement signals while the first wheel has 40 mm flat. The wheel flat produced the defect signal containing high frequency components. The defect signal is superimposed on the displacement signals.

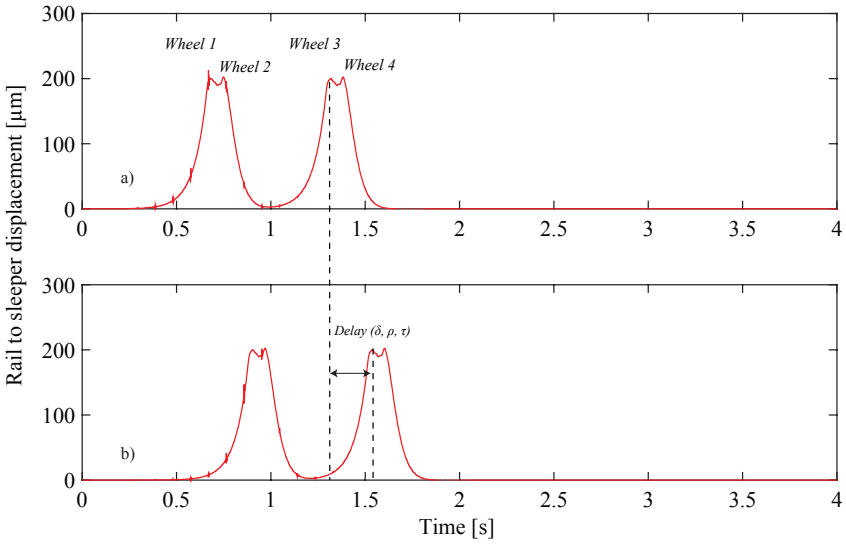

Figure 4.8: The rail to sleeper displacement signals for two consecutive sleepers while the first wheel is defective.

4.2. RESULT INDICATORS

The fusion process reconstructs a new signal using the signals measured by multiple sensors. The output of the fusion process is influenced by several parameters such as the train velocity, axle load, defect type, number of sensors, length of the effective zone, and the wheel size. To evaluate the effect of the influential parameters, a reference signal (ψ_r) is used to make a comparison with the reconstructed signal (ψ_s). The reference signal is produced when the number of sensors increases to the extent that the samples completely cover the wheel circumference (e.g., 200 sensors). In addition, the reference signal is generated with no measurement noise, and with the actual diameter that is used in the data generation step. In the next section for the parametric study, the number of sensors is less than the number of sensors used for the reference signal and the measurement noise is considered. In addition, the error of estimating the velocity and diameter influences the reconstructed signal. Therefore, the comparison between the reference signal and the reconstructed signal with these errors gives a sense about the results obtained.

The similarity comparison is carried out using the cross-correlation between the normalized signals. For this purpose, the reference and the reconstructed signals are normalized with respect to their average, and their standard deviation as presented below:

$$\hat{\psi}_r = \frac{\psi_r - \mu_r}{\sigma_r} \tag{4.1}$$

$$\hat{\psi}_s = \frac{\psi_s - \mu_s}{\sigma_s} \tag{4.2}$$

where $\hat{\psi}_r$ is the normalized reference signal, $\hat{\psi}_s$ is the normalized reconstructed signal, μ_r and σ_r are the average and the standard deviation of the reference signal, and μ_s and σ_s are the average and the standard deviation of the reconstructed signal.

The samples of the reference signal and the reconstructed signal have non-uniform intervals. Therefore, the signals are interpolated with similar intervals (for example 1mm) to generate the interpolated signals. $\hat{\psi}_r^*$ is the interpolated normalized reference signal and $\hat{\psi}_s^*$ is the interpolated normalized reconstructed signal. These signals have K samples with identical intervals.

To calculate the similarity between two signals, the cross-correlation and the auto-correlation of the signals are used. The auto-correlation is based on the Equation 3.8 while put the same signal as the input. The cross-correlation and the auto-correlation are calculated as follow:

$$R_{\hat{\psi}_r^*,\hat{\psi}_s^*}(\zeta) = \sum_{k=1}^{K-\zeta} \hat{\psi}_r^*(k+\zeta)\hat{\psi}_s^*(k), \qquad \zeta = 0,1,2,\ldots \tag{4.3}$$

$$R_{\hat{\psi}_r^*,\hat{\psi}_r^*}(\zeta) = \sum_{k=1}^{K-\zeta} \hat{\psi}_r^*(k+\zeta)\hat{\psi}_r^*(k), \qquad \zeta = 0,1,2,\ldots \tag{4.4}$$

Using the Equations 4.3 and 4.4 the similarity between the reference signal and the reconstructed signal ($\tilde{S}_{\psi_r,\psi_s}$) is calculated as

$$\tilde{S}_{\psi_r,\psi_s} = \frac{\arg\max_\zeta R_{\hat{\psi}_r^*,\hat{\psi}_s^*}(\zeta)}{\arg\max_\zeta R_{\hat{\psi}_r^*,\hat{\psi}_r^*}(\zeta)} \tag{4.5}$$

According to this Equation, the similarity will be between zero and one, where one indicates 100% similarity and zero indicates no similarity.

To evaluate the performance of the proposed method for estimating the wheel diameter and the train velocity, we make a comparison between the estimated diameter and velocity to the actual values used in the data generation step. This comparison presents the absolute errors of the wheel diameter and the train velocity estimation using the proposed methods in [mm] and [m/s] respectively.

Furthermore, some parameters have a random nature such as the noises and the position of the defective wheel with respect to the sensors. Therefore, the test is repeated several times and the results are presented as an average of the repetitions with their corresponding standard deviations. In some cases, due to the noise or lack of samples, the diameter estimation process leads to nothing and cannot estimate any diameter. Therefore, the reliability of the diameter estimation method is also presented by the percentage of the tests that gives any value as the estimated diameter to the total number of tests.

4.3. RESULTS OF THE PARAMETRIC STUDY AND DISCUSSION

The general overview of the parametric study and the detailed flowchart of the steps are presented in Figure 4.9. VI-Rail generates the required data as the input of the fusion model. In Figure4.9b, the position of the wheel (effective zone of the sensor) is estimated using a low-pass filter. The delay between the signals and the train velocity are used to

select the required samples and make the dataset $S_{m,n}$ explained in Equation 3.14. In Figure 4.9d, the data collected in dataset is fused to reconstruct a new signal, using the wheel circumference estimated in Figure 4.9c, and using the sensor configuration.

Figure 4.10 presents an example of the data collected by 59 sleepers (sensors) for a wheel with a 40 mm flat. In this Figure, the samples were collected using the Single Sampling Method (SSM) explained by Equation 3.15. The samples represent the first column of the dataset $S_{m,n}$ (See Equation 3.14). According to the SSM, each sensor collects one sample. Therefore, the distance between the samples is equal to the sensor interval that is 600 mm. Figure 4.11 presents the samples collected from the identical signals but using the Multiple Sampling Method (MSM). In this Figure, the samples represent all samples measured by the effective zones collected in the dataset $S_{m,n}$. As is clear from these Figures, the collected samples provide a limited piece of information.

Figure 4.12 makes a comparison between the signals reconstructed with the SSM and MSM based on Equations 3.16 and 3.18. In this example, the samples collected in Figures 4.10 and 4.11 are fused to reconstruct new informative signals. Figure 4.12a shows the contact force that is provided by VI-Rail. The contact force is transferred to the wheel and rail and makes the dynamic response of the wheel and rail. In this example, the rail to sleeper displacement signal is used as the response of the rail to the contact force. In Figure 4.12b, the SSM used 59 sensors to collect data and reconstruct a signal. In Figure 4.12c, the MSM used the same sensors but exploited more samples. In Figure 4.12b, the first downward of the defective area was not sensed completely, while in Figure 4.12c, the MSM overcame this problem.

Using the Equation 3.18, the multiple samples collected by the multiple sensors are fused to reconstruct a new signal. Figure 4.13 presents several examples of the signals reconstructed by the proposed method. The input signals have been the vertical rail to sleeper displacement signals simulated by VI-Rail. The signals have been normalized by subtracting the average of the signals. The difference between the signals is due to the wheel defects.

4.3.1. RESULTS OF THE BASE VALUES

Several parameters influence the output of the fusion process. To evaluate the effect of each parameter a set of base values is defined. In this subsection, the results of fusion process using the base values are presented. In this study, the trends of the results are more important than the exact value. Some parameters should be changed over the data generation process and a few others should be changed over the fusion process. Table 4.4 presents the base values with their variation ranges. These parameters are explained and investigated in the following subsections. In every simulation, the base values remain constant except one parameter.

The outputs of the parametric study are the estimated values for the wheel diameter and the train velocity, and the similarity of the signal reconstructed. Table 4.5 compares the absolute error, standard deviation, and the reliability of the diameter estimated by the SSM and MSM using the base values. As explained earlier, multiple sets of samples (different columns in dataset 3.14) can be used in the SSM. In Table 4.5, the single sample-single set indicator presents the results of the diameter estimated by SSM using the first set of the samples (first column in 3.14 that has been presented in 3.15). The SSM

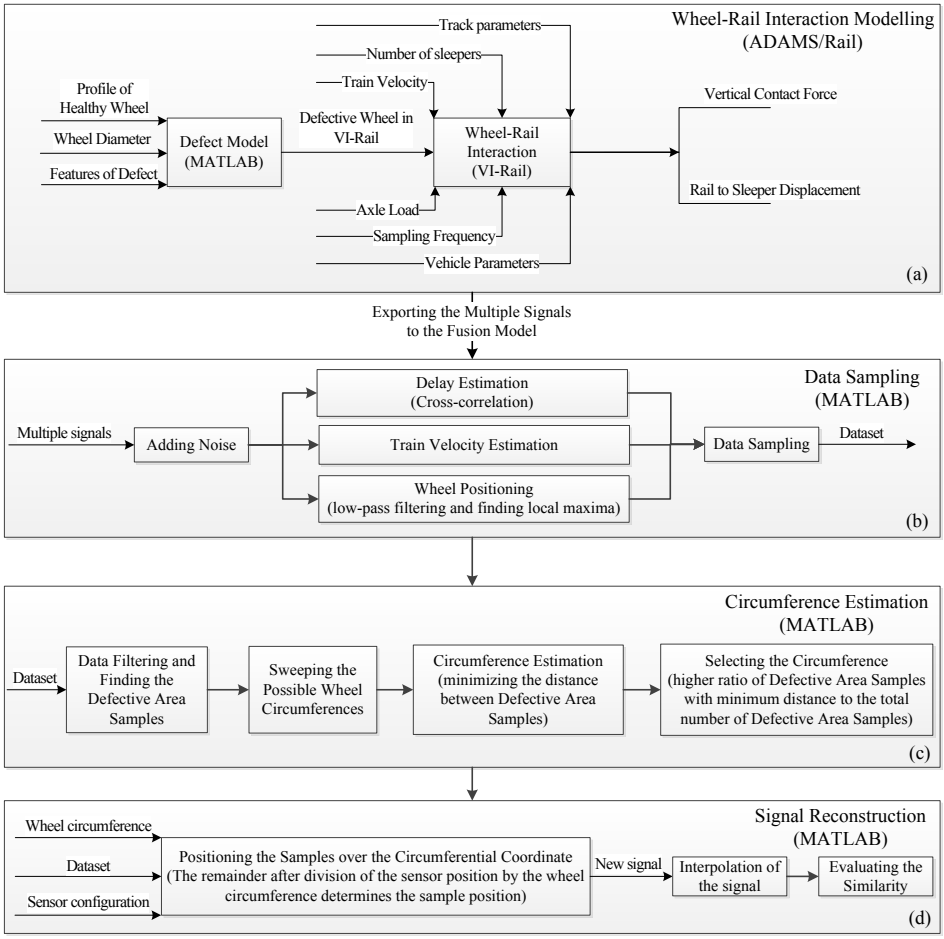

Figure 4.9: The process of the parametric study.

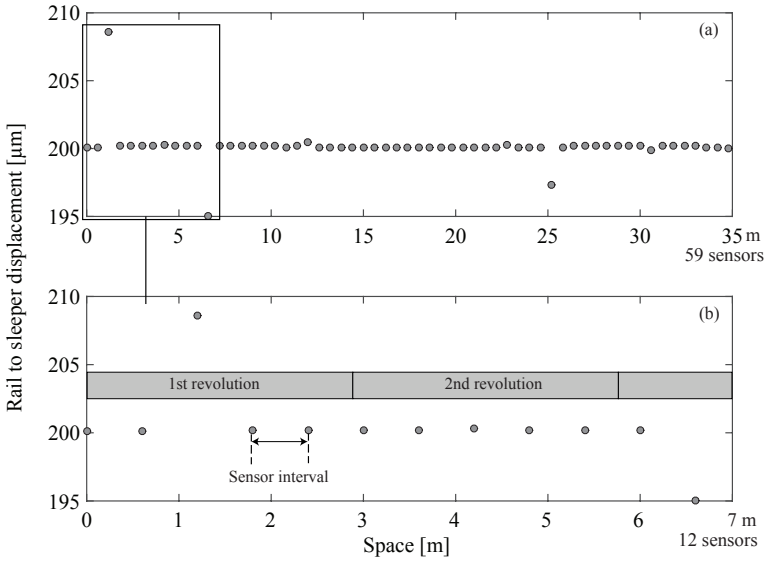

Figure 4.10: a) The simulated data sampled by 59 sensors using the SSM b) the magnified view of the plot (a).

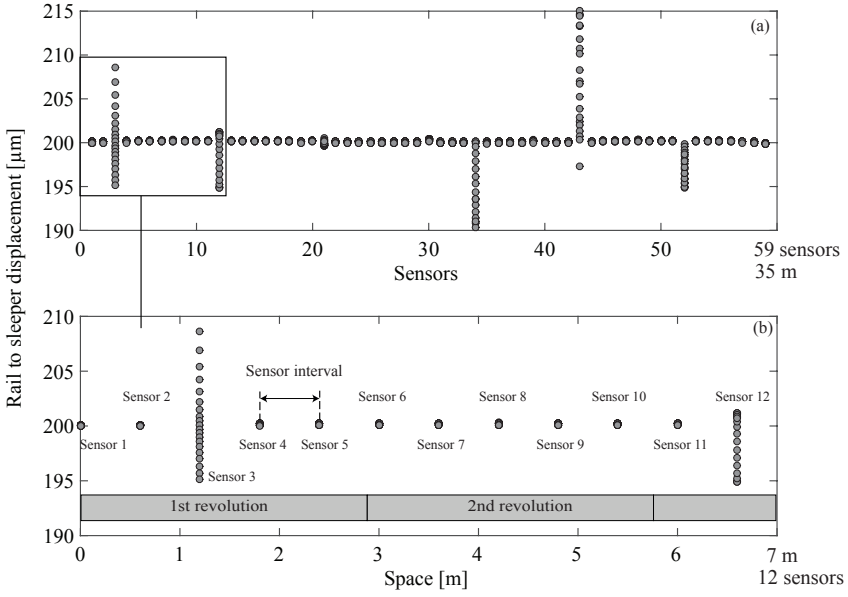

Figure 4.11: a) The simulated data sampled by 59 sensors using the MSM b) the magnified view of the plot (a).

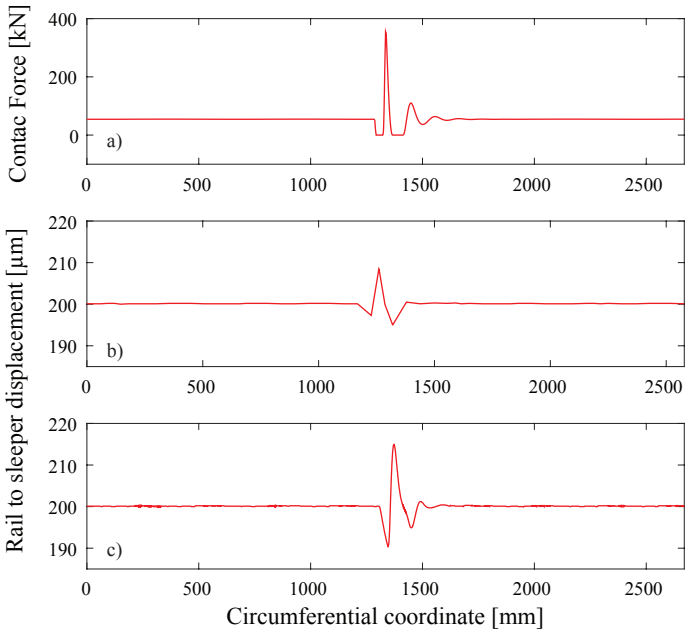

Figure 4.12: a) The simulation result of a wheel-rail contact force for a wheel with 40 mm flat and 30 m/s velocity. The signals reconstructed from the rail to sleeper displacement signal collected by 59 sensors using b) the SSM, and c) the MSM.

Table 4.4: The base value and the variation range of the parameters

Parameter	**Base value**	**Range**
Wheel diameter	900 mm	840 – 920 mm
Defect type	40 mm Wheel flat	Wheel flat 20-60 mm Spalling 15-30 mm
Number of sensors	50	10-60
Sensor interval	600 mm	-
Sensor measurement noise	4%	1-5%
Position of defects	Random	Wheel circumference
Train velocity	30 m/s	10-30 m/s
Train axle load	11120 kg	16500, 22000 kg
Sensor sampling frequency	10 kHz	-
Length of effective zone	60 mm	10-60 mm

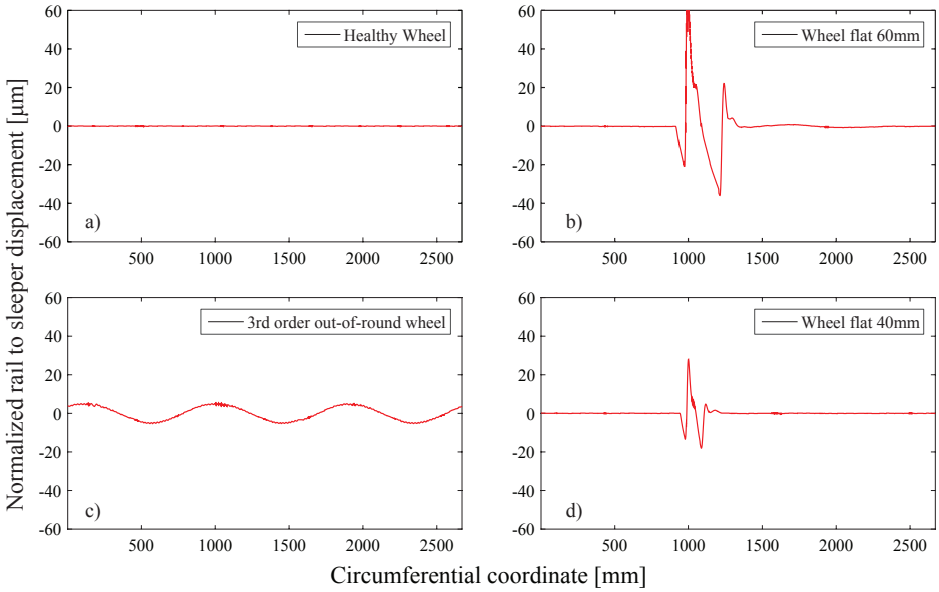

Figure 4.13: The signals reconstructed for the wheels with different defects: a) healthy wheel, b) 60 mm wheel flat, c) 3rd order out-of-round wheel, and d) 40 mm wheel flat.

can use different sets to estimate the diameter. Using all sets of the samples improves the results of SSM that is presented by single sample–multiple sets indicator. Hereafter, single sampling indicator refers to the single sample–multiple sets. According to Table 4.5, using the multiple samples improves the diameter estimated and its reliability.

The MSM uses the train velocity to estimate the distance between the samples collected in the effective zone. To estimate the train velocity, the time delay between the signals measured by two sensors is used. To achieve this purpose, any pair of sensors can be used. In this research, the consecutive pairs of sensors, (e.g., sensor 1 and 2), are used. The train velocity is the average of the velocities estimated by different pairs. For example, for a test with 50 sensors, the average of the velocity estimated by 49 pairs of sensors gives the output. Therefore, the result provides a reasonable estimate of the train velocity that is presented in Table 4.6. Using the acquired velocities in the Table 4.6, and based on the Equation 3.21, the space distances between the samples of each sensor (λ) will be 3.0001 and 3.0018 mm respectively for the noise free and the noisy measurements that is satisfactory for the data fusion process.

Table 4.7 presents the results of the similarity evaluation. For the noise free measurement, the MSM improves the similarity from around 49% to 98%. The diameter error changes the similarity of SSM from 49% to 40%. The MSM improves the similarity from 40% to 97% and its standard deviation from 7% to around 4%. This improvement is achieved, directly by using more samples to reconstruct the signal, and indirectly by decreasing the diameter estimation error. The measurement noise has a significant effect

Table 4.5: The results of the diameter estimation process calculated by the SSM and MSM using the base values

	Indicator	Error [mm]	Standard deviation [mm]	Reliability [%]
Noise free	SSM – Single set	2.72	0.58	6.4
	SSM – Multiple sets	2.40	0	0.8
	MSM	0.05	2.89	100
Noisy	SSM – Single set	0.61	3.79	3.2
	SSM – Multiple sets	0.77	0	0.8
	MSM	1.96	9.12	98.4

Table 4.6: The results of the velocity estimation for the base values.

Indicator	Error [m/s]	Standard deviation [m/s]
Noise free	0.000639	0.000312
Noisy signal	0.0179	0.0119

on the results. Therefore, exploiting the sensors with high signal to noise ratio is vital. The next subsections assess the influential parameters on the reconstruction process and present the sensitivity of the results to the variation of the parameters.

4.3.2. MEASUREMENT NOISE

VI-Rail generates pure data while the real measurements will be noisy. Therefore, evaluating the effect of the measurement noise on the fusion process is vital. To make a realistic assumption about the signal to noise ratio, the results of a field test is considered [79] that used FBG strain sensors. That measurement shows at least 120 $\mu\varepsilon$ variation in the strain signal due to the wheel passage, while the noise was less than 5 $\mu\varepsilon$ (4%). In this study, the minimum variation in the rail to sleeper displacement signal is 200 μm. Therefore, the maximum magnitude of the noise should be less than 8 μm (4%). To simulate the noisy measurement, a set of White Gaussian Noises is added to all signals generated by VI-Rail. The average of the noises is zero and three times of the standard deviation (3σ) is 8 μm.

Figure 4.14 presents the absolute error and the reliability of the diameter estimation process for different measurement noises. The measurement noise has several negative effects on the fusion process. First, the measurement noise makes an error on the sample delay (δ) between the measured signals. This error leads to errors in the sample distance (λ) and in the wheel positioning. Another negative effect of the measurement noise is variation of the sensor output. The variation in the magnitude of the samples collected makes an error in the diameter estimated. According to Figure 4.14, the measurement noise increases the standard deviation of the errors for both sampling methods, but the MSM ensures much higher reliability than the SSM.

Table 4.7: The comparison between the similarity of the SSM and MSM for the base values.

Indicator			Similarity [%]	Standard deviation [%]
Noise free	SSM	Without diameter error	49.95	5.32
	MSM	Without diameter error	98.58	1.46
	SSM	With diameter error	40.28	7.53
	MSM	With diameter error	97.52	4.22
Noisy	SSM	Without diameter error	28.78	7.13
	MSM	Without diameter error	52.91	10.52
	SSM	With diameter error	28.90	4.61
	MSM	With diameter error	50.40	11.16

Figure 4.15 presents the absolute error of the velocities estimated for different measurement noises. As we expected, increasing the measurement noise increases the magnitude and the standard deviation of the error of the velocity estimation process. The errors of the velocities estimated by the filtered signal are also presented in Figure 4.15. By filtering the measured signals, the error of the velocity estimation process and its corresponding errors, the error of the sample distance (λ) and the error of the wheel positioning (sampling error), can be reduced, while the negative effect on the diameter estimation process and the variation of the sensor output are remaining.

Figure 4.16 shows the results of the similarity assessment for different measurement noises. The MSM improves the similarity of the reconstructed signals when the noise is not high. By increasing the measurement noise, the similarity significantly decreases and the MSM loses its ability. The measurement noise varies the magnitude of the sensor output. By considering the maximum of the signal as the output of the sensor, the measurement noise has limited effect. For example, 5% noise variates 5% of the magnitude of the sensor output. Instead, the fusion method considers the position and the magnitude of different samples to generate a pattern. Therefore, the small measurement noise can influence the signals reconstructed. According to Figure 4.16, the 5% noise decreased the similarity of the reconstructed signals from around 100% to less than 50%. As a result, using sensors with high Signal-to-Noise Ratio (SNR) is critical to produce informative signals.

4.3.3. NUMBER OF SENSORS

The fusion method exploits the data collected by multiple sensors. The signal reconstruction with a few number of samples leads to signal distortion. Intuitively, more sensors collect more samples and give better results. The sensors should be mounted on an identical situation that is challenging for a measurement with high number of sensors. Therefore, providing similar results with lower number of sensors is essential. A commercial interrogator with four measurement channels, can interrogate around 160-320 FBG sensors, fulfilling practical requirements by providing high number of sensors and

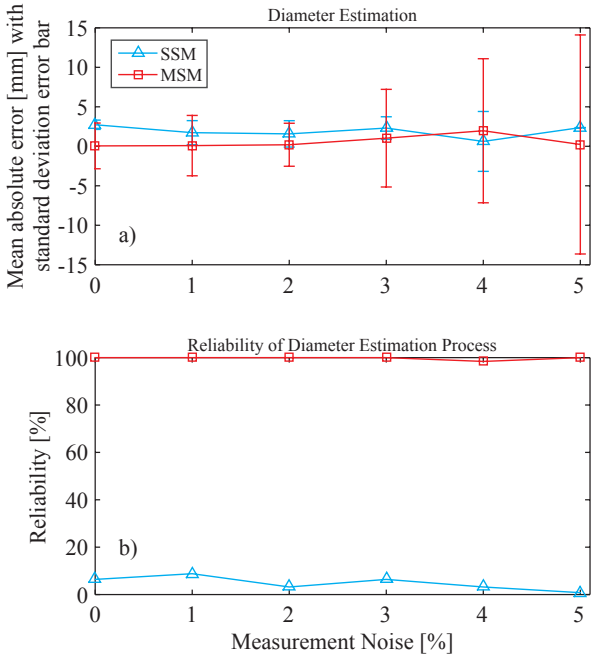

Figure 4.14: The results of the diameter estimation process using the SSM and MSM for different measurement noises. a) Mean absolute error with standard deviation error bar, b) reliability.

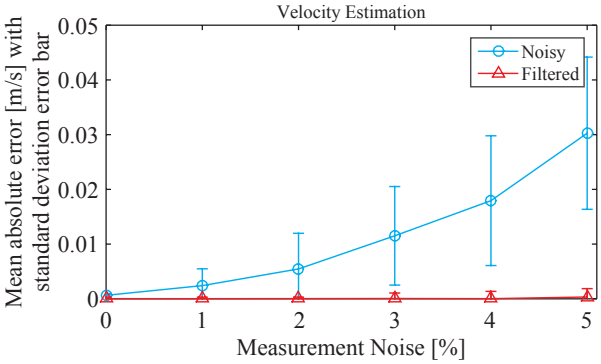

Figure 4.15: The results of the velocity estimation process for different measurement noises and for the filtered signals.

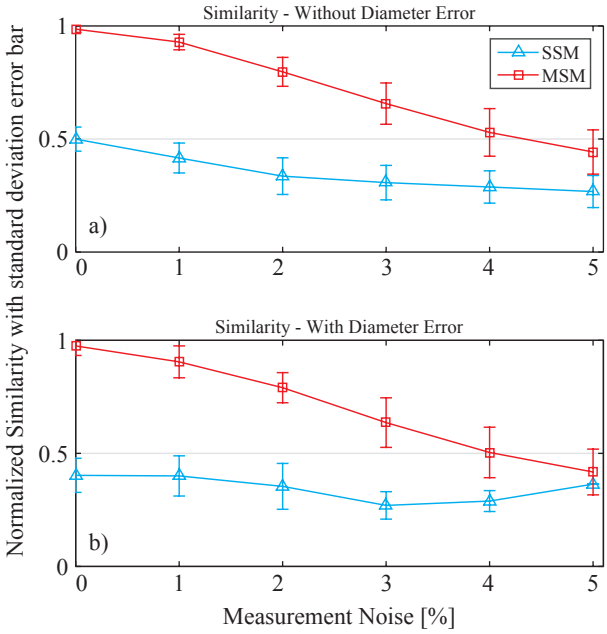

Figure 4.16: The results of the similarity assessment for different measurement noises. a) Normalized similarity with standard deviation error bar without diameter error, b) with diameter error.

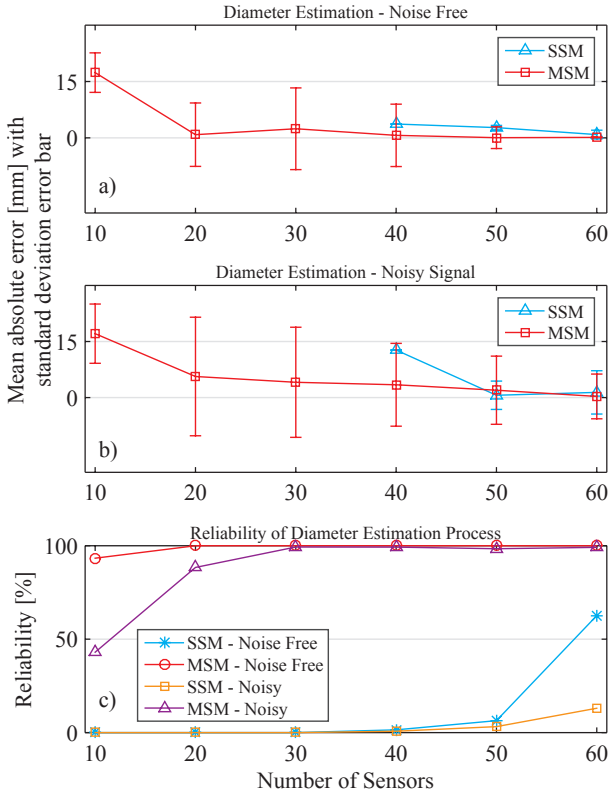

Figure 4.17: The results of the diameter estimation process using the SSM and MSM for different number of sensors. a) Mean absolute error with standard deviation error bar for noise free signals, b) mean absolute error for noisy signals, and c) reliability.

high SNR [46].

Figure 4.17 presents the results of the diameter estimation process for different number of sensors, noise free and noisy signals and using the SSM and MSM. The reliability of the SSM for lower than 40 sensors is almost zero. Therefore, the SSM did not give any estimate for the wheel diameters when the number of sensors is lower than 40 sensors. The MSM ensures very high reliability especially for small number of sensors. When the reliability of the MSM reached to around 100%, increasing the number of sensors decreases the error and its standard deviation. As a general result, increasing the number of sensors improves the results of the diameter estimated.

Figure 4.18 presents the results of the velocities estimated. In general, the noise free signal gives lower error than the noisy signal. Increasing the number of sensors influences the average of the errors and decreases their standard deviations. In Figure 4.18, there is an outlier in the noise free signals at 20 sensors. To understand the reason of this strange behaviour, the study is repeated with higher resolution. Figure 4.19 depicts the

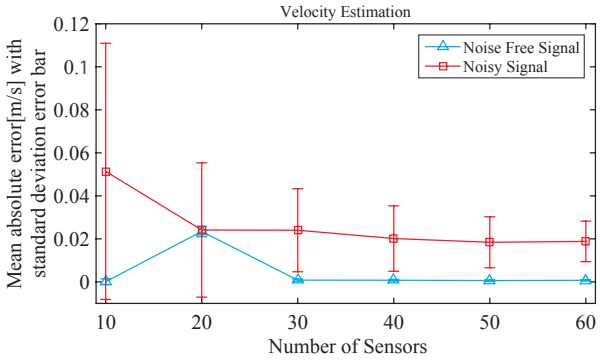

Figure 4.18: The results of the velocity estimation process for different number of sensors.

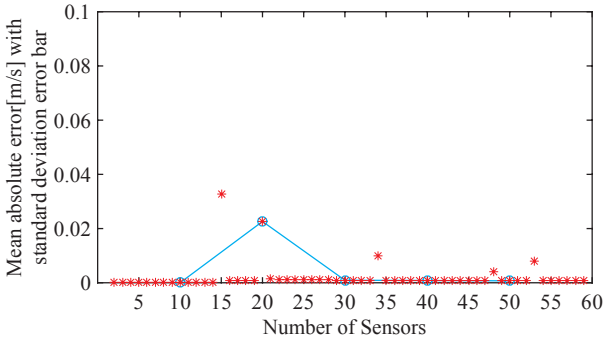

Figure 4.19: The results of the velocity estimated for different number of sensors with higher resolution.

results of the velocity errors for the noise free measurement with higher resolution.

According to Equation 3.23, the velocity is a function of the sample delay (δ) that is estimated using the cross-correlation between the signals measured by different sensors (See the Equations 3.8 and 3.9). Based on Equations 3.6 and 3.7, the measured signals can be modelled as the combination of the signal generated by the wheel movement, the signal generated by the wheel defect, and the uncorrelated noises. For the noise free measured signal, the defect signal influences the output of the cross-correlation function. As explained before, the velocity is calculated by averaging the velocities estimated by multiple pairs of sensors. Most of the time, the averaging excludes the effect of the defect signal, but it is not always the case. Therefore, the outlier is generated for the noise free signals at 20 sensors.

The low pass filter used in the prior subsection can cancel out the negative effect of the defect signal and the measurement noise. Figure 4.20 presents the results of the velocity estimation process for different number of sensors for the filtered signals.

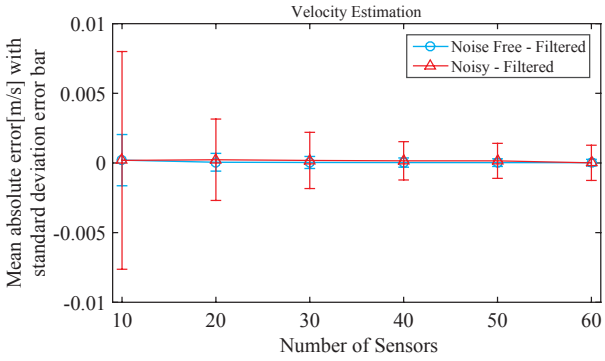

Figure 4.20: The results of the velocity estimation process using the filtered signals for different number of sensors.

Figure 4.21 compares the results of the similarity between the SSM and MSM while the number of sensors increases. The MSM collects multiple samples to fill the gaps between the data collected by the SSM and improves the similarity. The effect of the noise and the diameter error when they occur simultaneously is significant to the extent that even an increasing sensor number could not improve the similarity. As a general result, increasing the number of sensors increases the similarity.

4.3.4. LENGTH OF EFFECTIVE ZONE

The comparison between the lengths of the effective zone and the wheel circumference (around 3000 mm) in Figure 3.1 shows that the sensor had a long effective zone around 600 mm. FBG strain sensors have smaller effective zone [42], [43] but can be altered using the special gauges [49]. The data generated by VI-Rail is the rail to sleeper displacement signal. The effective zone for this signal is around 60 mm that is constant in all simulations. Therefore, to evaluate the effect of the effective zone variations, different lengths from the effective zone are used.

Figure 4.22 makes a comparison between the errors and the reliabilities of the diameters estimated by the SSM and MSM for different lengths of the effective zone. Generally, by increasing the length of the effective zone, the error of the diameter estimation process decreases. To use all samples of the effective zone, accurately positioning of the effective zone on the signal is necessary. To estimate the train velocity entire the measured signals are used. Therefore, the length of the effective zone is not the influential factor for estimating the train velocity.

Figure 4.23 compares the similarity of the signals reconstructed using the SSM and MSM with different lengths of the effective zone. Increasing the length increases the similarity. Therefore, using a sensor with longer effective zone can reduce the number of sensors required.

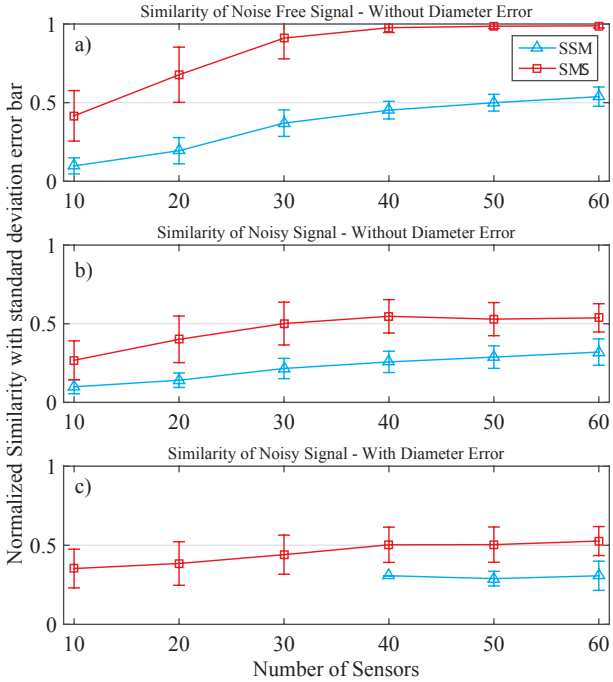

Figure 4.21: The results of the similarity assessment for different number of sensors for a) noise free signals without diameter error, b) noisy signals without diameter error, and c) noisy signals with diameter error.

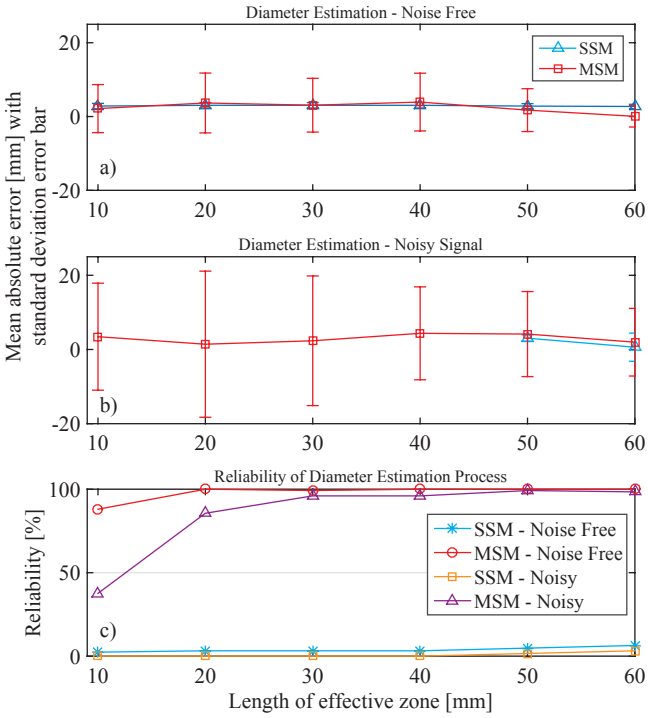

Figure 4.22: The results of the diameter estimation process using the SSM and MSM for different lengths of the effective zone. a) Mean absolute error with standard deviation error bar for noise free signals, b) mean absolute error for noisy signals, and c) reliability.

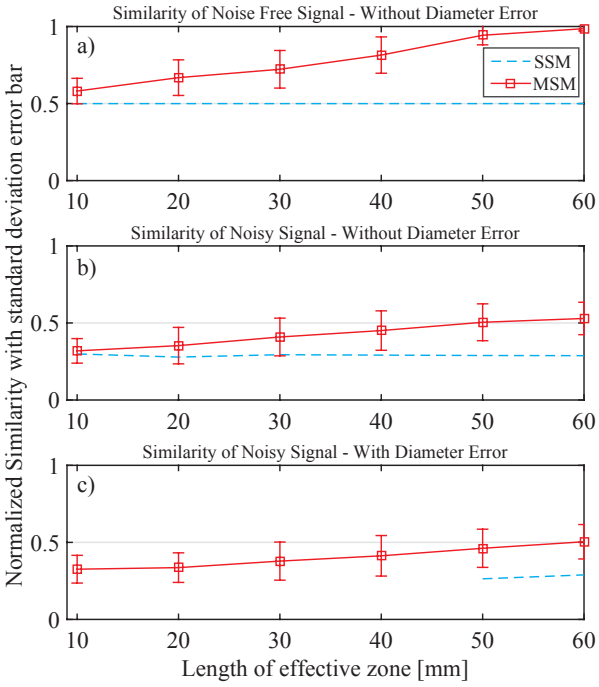

Figure 4.23: The similarity comparison between the signals reconstructed by the SSM and MSM for different lengths of effective zone. a) Normalized similarity with standard deviation error bar for noise free signals without diameter error, b) for noisy signals without diameter error, and c) for noisy signals with diameter error.

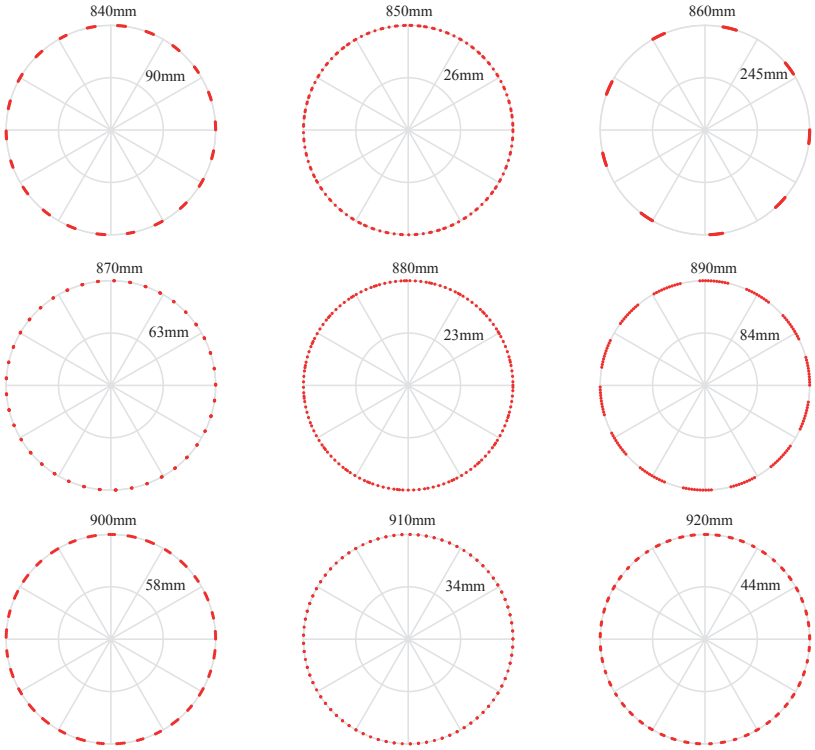

Figure 4.24: The distribution of the samples over the circumferential coordinate for different diameters.

4.3.5. WHEEL DIAMETER

For a certain sensor configuration, the wheel diameter determines the frequency of the measurement from the wheel circumference in the space domain. The measurement frequency for the range of wheel diameters (840–920 mm) will be 4.39-4.81 measurements per cycle for 600 mm sensor interval. This variation determines the distribution of the samples over the circumferential coordinate. Figure 4.24 presents an example of the distribution of the samples over the circumferential coordinate for different wheel diameters. In this example the simulated samples collected by 150 sensors using the SSM with 600 mm sensor interval. The numbers on top of the circles present the wheel diameter and the numbers inside the circles indicate the maximum distance between the samples mapped over the circumferential coordinate.

Several parameters influence the distribution of the samples such as the sensor interval, wheel diameter, length of the effective zone, number of sensors, and the train velocity. These parameters with the exception of the number of sensors are the out-of-control parameters. The samples should cover entire the wheel circumference to reconstruct the

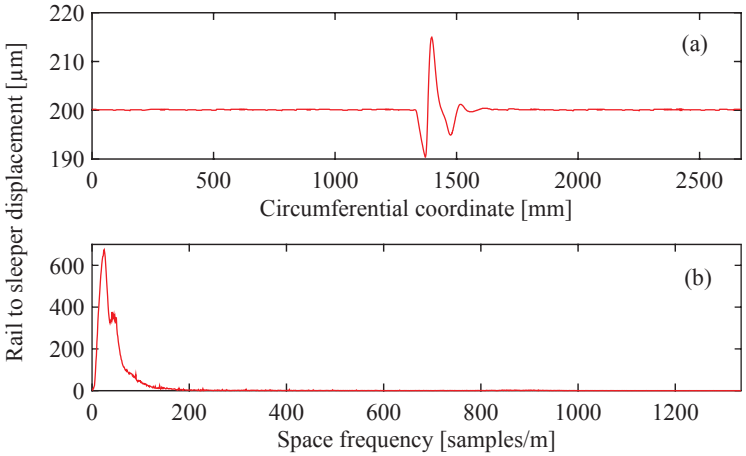

Figure 4.25: a) The signal reconstructed by 59 sensors using the MSM for a wheel with 850 mm diameter, 40 mm flat, and 30 m/s velocity, b) frequency spectrum of the signal.

signal properly. According to Figure 4.24, wheel diameter changes the distribution and the frequency of the samples. The monitoring system should be able to cover the whole range of the wheel diameter. Therefore, the minimum number of sensors should be determined based on the range of the wheel diameter. Figure 4.25 represents the defect signal presented in Figure 4.12c in the frequency domain using the Fast Fourier transform (FFT). The defect signal after reconstruction is interpolated to have 1000 samples per meter in the space domain. Figure 4.25b shows that the frequency of the signal is limited to the frequency lower than 100 Hz. It means the Nyquist frequency in the space domain is 200 samples per meter (twice the highest frequency contained in the signal). Therefore, the defect signal can be reconstructed without any distortion, if the maximum distance between the consecutive samples is smaller than 5 mm.

Using the criteria defined for the sampling frequency, the minimum number of sensors required for monitoring the whole range of the wheel diameter is determined. Figure 4.26 presents the maximum distance between the consecutive samples (λ_{max}) obtained after the signal reconstruction, for different number of sensors. In this example, the sensor interval is 600 mm and the length of the effective zone is 60 mm. Intuitively, changing the length of the effective zone changes the trends of the plot. Figure 4.27 presents this distance for different number of sensors when the length of the effective zone increased to 300 mm. In this case, with 19 sensors the λ_{max} is decreased to less than 5 mm for all wheel diameters. The comparison between the Figures 4.26 and 4.27 shows that considering the number of sensors and the length of the effective zone at the same time is important.

The monitoring system should be able to deal with the whole range of the wheel diameters because the wheel diameter is an out-of-control parameter. Therefore, the number of sensors and the length of the effective zone should be determined with re-

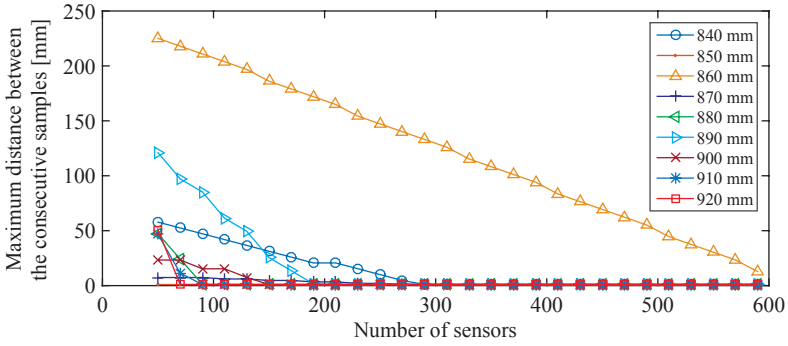

Figure 4.26: The maximum distance between the consecutive samples for different number of sensors with 600 mm sensor interval and 60 mm length of the effective zone.

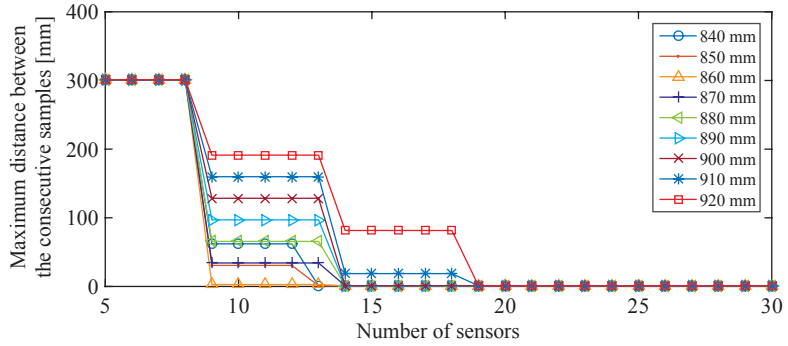

Figure 4.27: The maximum distance between the consecutive samples for different number of sensors with 600 mm sensor interval and 300 mm length of the effective zone.

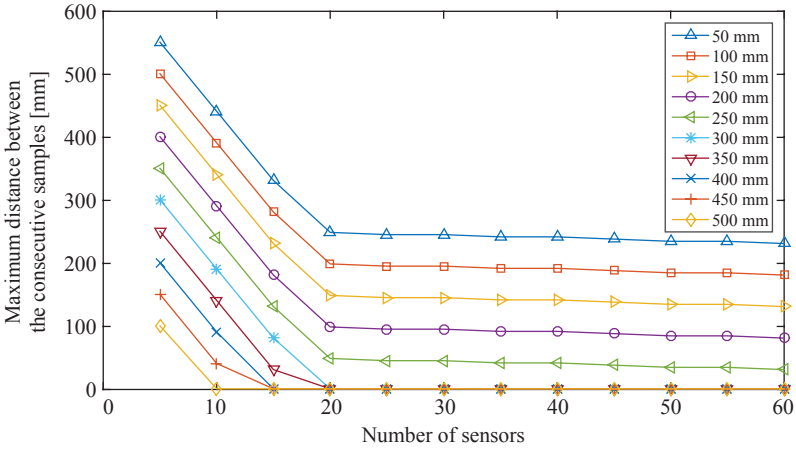

Figure 4.28: The maximum distance between the consecutive samples for different number of sensors and different lengths of the effective zone with 600 mm sensor interval.

spect to the wheel diameter. As a result, the highest λ_{max} for different wheel diameters is considered as the representative of the whole range of the wheel diameters. Figure, 4.28 shows the variation of the highest λ_{max} for different number of sensors and the different lengths of the effective zone. According to this figure, with 20 sensors, increasing the length of the effective zone is more helpful than increasing the number of sensors.

Figure 4.29 presents the results of the diameter estimation process for different diameters. The reliability of the process using the SSM significantly varied for different wheel diameters while the MSM constantly gives reliable outputs. The results of the similarity assessment are presented in Figure 4.30. The comparison between the results obtained from Figures 4.24 and 4.30 shows that the wheel with large distance between the samples has low similarity and the wheel with small distance between the samples has high similarity. The MSM by filling the gaps between the samples using more multiple samples improves the similarity. In addition, the wheel condition can be considered constant over a few days. Therefore, multiple measurements can be used to improve the similarity by fusing the signals reconstructed by each measurement.

4.3.6. TRAIN VELOCITY

Train velocity influences the fusion process by changing the contact force, and the space sampling frequency. A wheel with different velocities exerts different contact forces, which influences the rail responses and the results obtained. Figure 4.31 depicts the ratio of the maximum and the average of the contact force for different train velocities that have been calculated based on Equation 2.5. This ratio shows the deviation of the dynamic contact force from the static force.

The sampling frequency of the sensors in the space domain depends on the train velocity. Increasing the train velocity decreases the space domain sampling frequency.

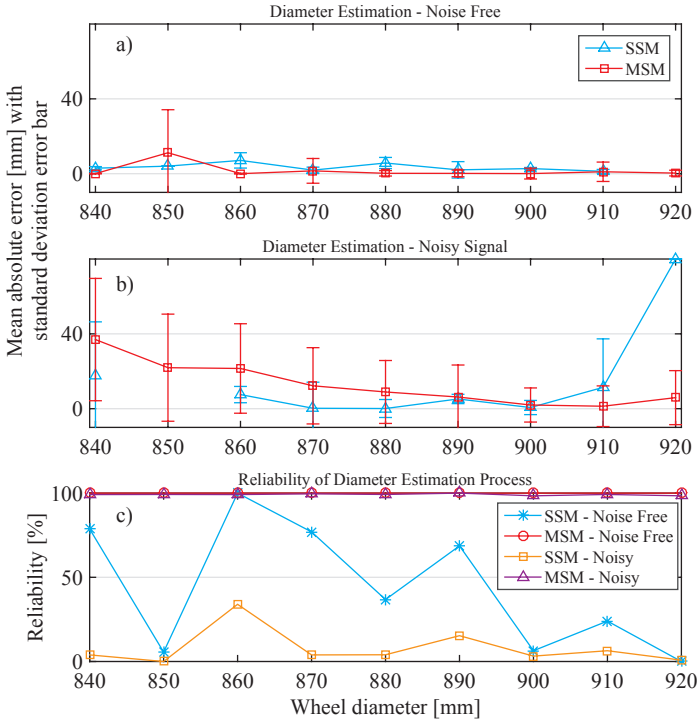

Figure 4.29: The results of the diameter estimation for different wheel diameters. a) Mean absolute error with standard deviation error bar for noise free signals, b) mean absolute error for noisy signals, and c) reliability.

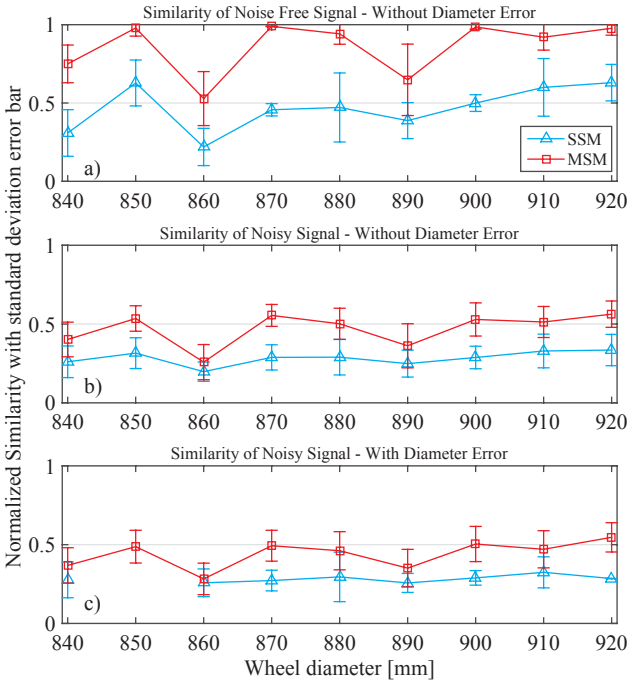

Figure 4.30: The results of the similarity for different wheel diameters. a) Normalized similarity with standard deviation error bar for noise free signals without diameter error, b) for noisy signals without diameter error, and c) for noisy signals with diameter error.

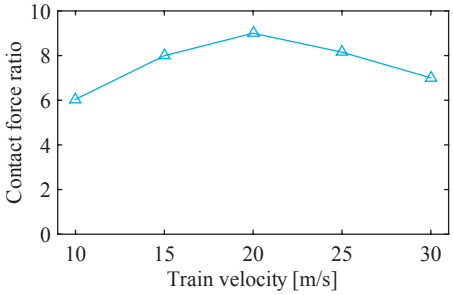

Figure 4.31: The contact force ratio for different train velocities.

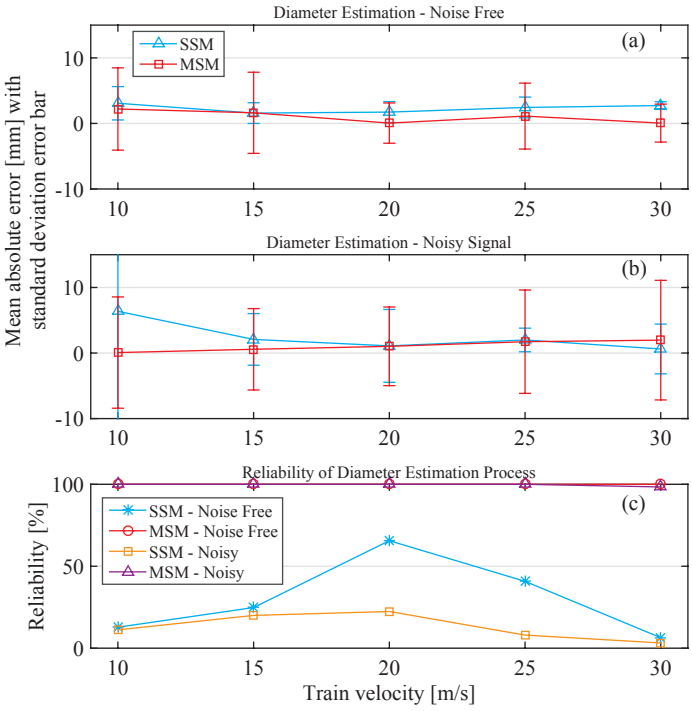

Figure 4.32: The comparison between the diameters estimated by SSM and MSM for different train velocities. a) Mean absolute error with standard deviation error bar for noise free signals, b) mean absolute error for noisy signals, and c) reliability.

Therefore, increasing the train velocity increases the space intervals between the samples (λ) while the samples are collected in the constant time interval. The contact force ratio has the same effect on the SSM and MSM, while the train velocity directly influences the MSM by changing the sampling frequency in the space domain. Lower train velocity gives higher sampling frequency in the space domain in which the MSM gives better performance. Figure 4.32 compares the results of the diameter estimation process using the SSM and MSM. For the velocity around 20 m/s, the process gives higher reliability. When the contact force ratio increases, the measurement noise has less influence on the process.

The velocity estimation process uses the cross-correlation to find the delay between the signals measured by two sensors. Generally, by increasing the train velocity, the space sampling frequency decreases. As a result, when the train velocity increases, the error of the estimated velocity will increase. On the other hand, the train velocity changes the contact force ratio that influences the cross-correlation and consequently the estimated velocity. For the noise free measurement, the contact force ratio has the dominant role, while for the noisy measurement, the signals are covered by the noise and the space

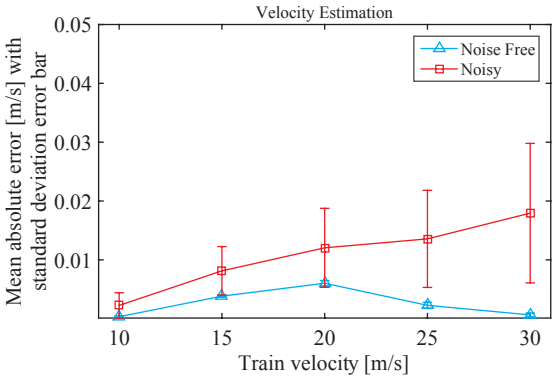

Figure 4.33: The results of the velocity estimation for different train velocities.

sampling frequency plays the major role. Figure 4.33 presents the error of the estimated velocity for different train velocities. According to Equation 3.21, higher sampling frequency of the sensors in the time domain can compensate the effect of high velocity on the space domain sampling frequency. Figure 4.34 presents the results of the velocity estimation process using the filtered signals for different velocities. The filter can exclude the effect of contact force and noises but the effect of decreasing the space sampling frequency remains. Therefore, increasing the velocity increases the error of the estimated velocities.

Figure 4.35 compares the similarity of the signals reconstructed by the SSM and MSM for different train velocities. Clearly, the MSM is performing better than the SSM especially for the lower velocities. As mentioned earlier, lower train velocity leads to higher space sampling frequency. Therefore, with constant length of the effective zone, higher samples are collected. For example, a sensor with 60 mm effective zone collects 60 samples with 1 mm distance from a train with 10 m/s velocity, while it collects 20 samples with 3 mm distance from a train with 30 m/s velocity.

4.3.7. DEFECT TYPE

The variation in the defect type and size changes the contact force and the contact force ratio and consequently changes the rail response. This subsection studies the wheel flat as the most severe defect and the wheel spalling as the most common defect. Figure 4.36 presents the contact force ratio for different defects. Increasing the defect size increases the contact force ratio.

The results of the diameter estimation process are presented in Figure 4.37. The contact force ratio shows the influence of the wheel defect on the contact force. Moreover, the higher contact force ratio gives the higher rail response ratio. Therefore, the measurement noise that is a function of the rail response, has less influence on the rail response that induced by wheel defect. As a result, increasing the defect size decreases the diameter estimation error and increases the reliability.

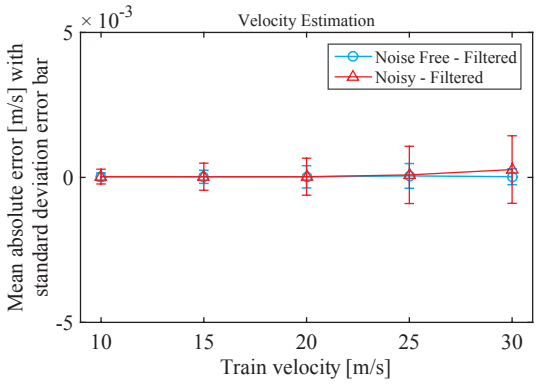

Figure 4.34: The results of the velocity estimation process using the filtered signals for different train velocities.

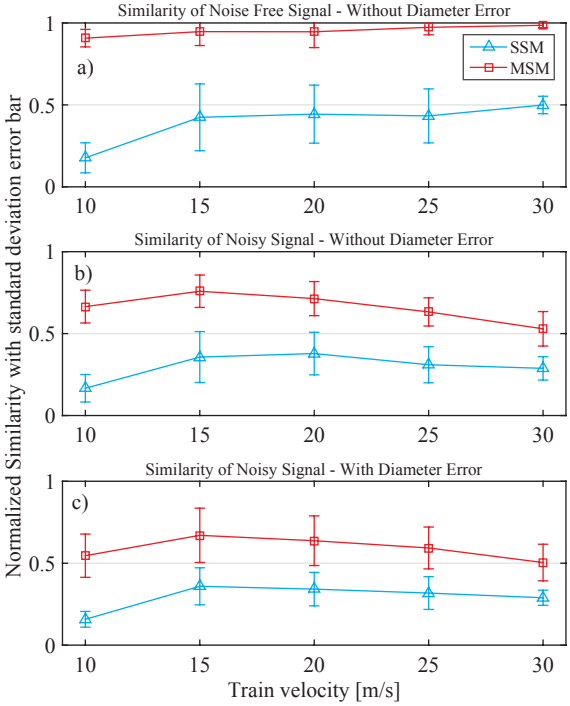

Figure 4.35: The similarity comparison between the signals reconstructed by the SSM and MSM for different train velocities. a) Normalized similarity with standard deviation error bar for noise free signals without diameter error, b) for noisy signals without diameter error, and c) for noisy signals with diameter error.

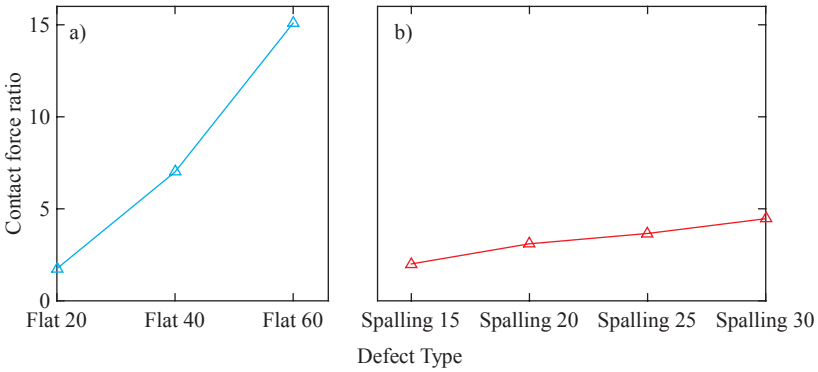

Figure 4.36: The contact force ratio for different defect types.

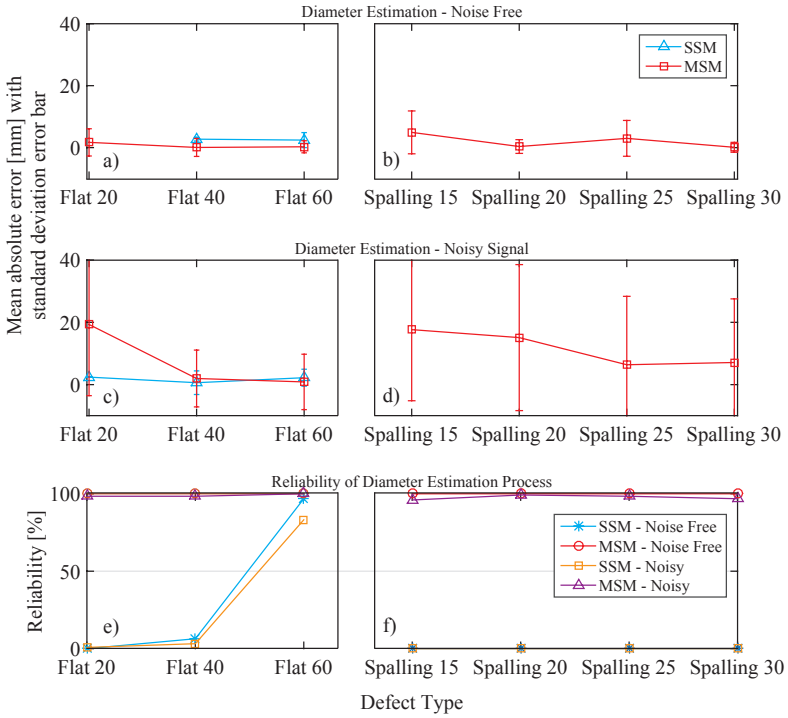

Figure 4.37: The results of the diameter estimation process for different defect types. a) and b) Mean absolute error with standard deviation error bar for noise free signals, c) and d) mean absolute error for noisy signals, and e) and f) reliability.

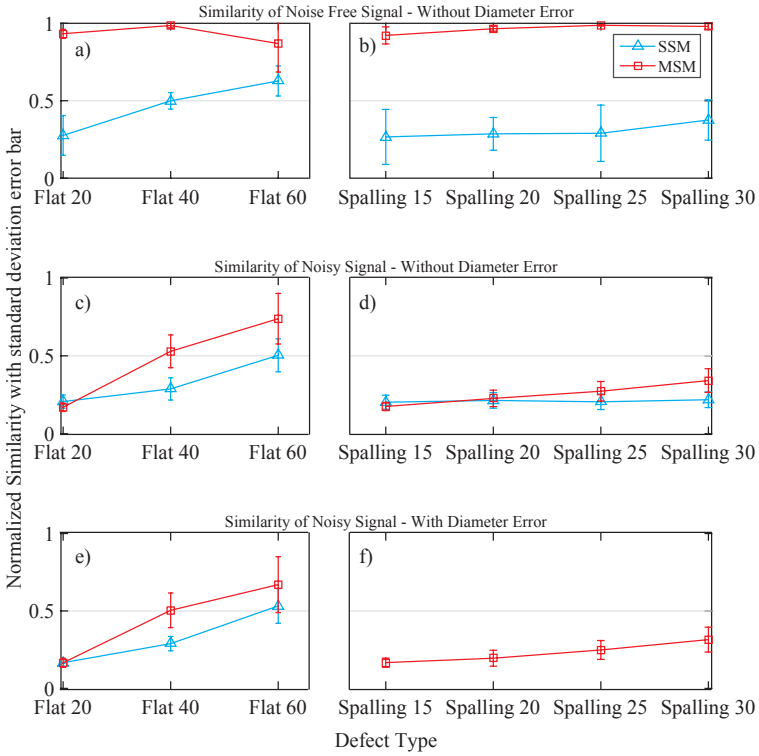

Figure 4.38: The results of the similarity assessment for different defect types. a) and b) Normalized similarity with standard deviation error bar for noise free signals without diameter error, c) and d) for noisy signals without diameter error, and e) and f) for noisy signals with diameter error.

In the same way, increasing the defect size increases the similarity. Figure 4.38 presents the results of the similarity assessment using the SSM and the MSM for different defect types and sizes. The MSM has better results than the SSM. For small defects, the measurement noise covers the defect signal and decreases the similarity. Therefore, using the sensors with high SNR is essential for reconstructing the defect signal for the small defects.

Figure 4.39 presents the results of the velocity estimation process for different defect types. The measurement noise increases the errors of the velocities estimated. In addition, the defect size changes the contact force ratio. Therefore, for the severe defects, the defect size is the dominant factor and causes the error. As mentioned earlier, the input signals can be filtered to suppress the negative effects of the noise and the defect signal on the velocity estimation process.

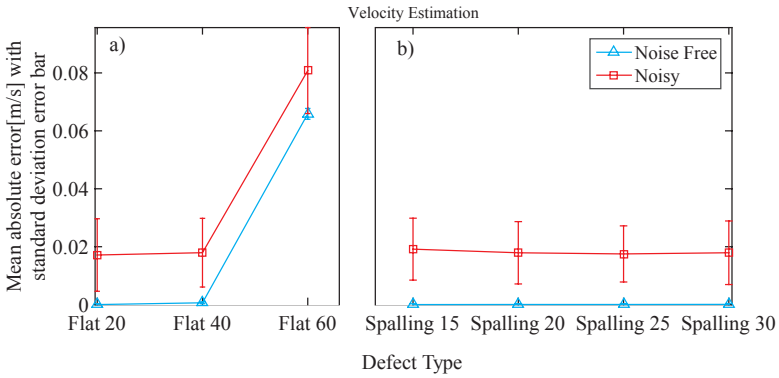

Figure 4.39: The results of the velocity estimation for different defect types.

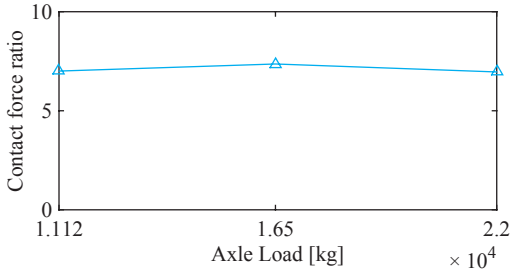

Figure 4.40: The contact force ratio for different axle loads.

4.3.8. AXLE LOAD

Table 4.2 presented the mass of car body, bogies and the wheelsets based on the Manchester benchmarks [77]. The total mass of a car body, two bogies and four wheelsets is 44482 kg and accordingly, the axle load is 11120 kg. To assess the effect of the axle load variation on the fusion process, two other axle loads, 16500 kg and 22000 kg are used.

Figure 4.40 presents the contact force ratio for different axle loads. According to this figure, the contact force ratio is almost constant for different axle loads. Therefore, different axle loads generate similar defect signals. As a result, axle load variations do not influence the fusion process directly. Figure 4.41 presents the results of the diameter estimation process for different axle loads. Increasing the axle load does not change the outputs of the process. The comparison between the SSM and the MSM shows that the MSM gives better performance by making smaller error and higher reliability.

The results of the similarity assessment and the velocity estimation process for different axle loads are presented in Figures 4.42 and 4.43. As we expected, the variations of the axle load have slightly changed the results. By increasing the axle load, the contact force ratio remains almost constant but the static load (average load) is increased.

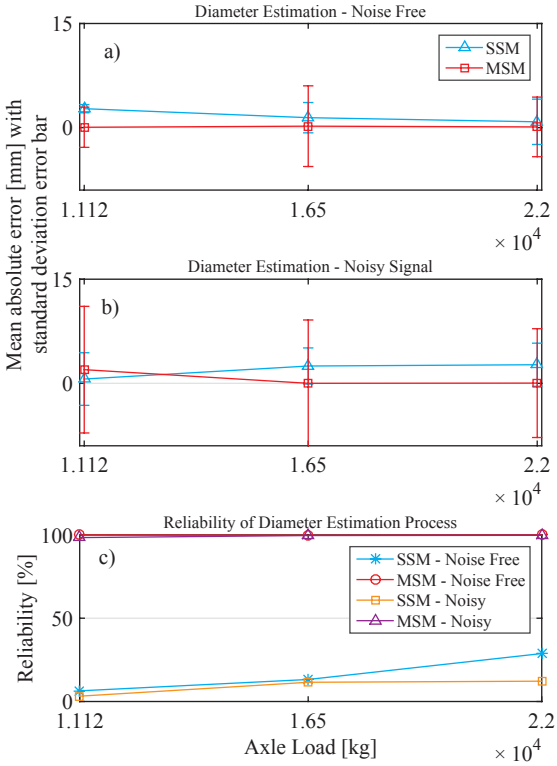

Figure 4.41: The results of the diameter estimation process for different axle loads. a) Mean absolute error with standard deviation error bar for noise free signals, b) mean absolute error for noisy signals, and c) reliability.

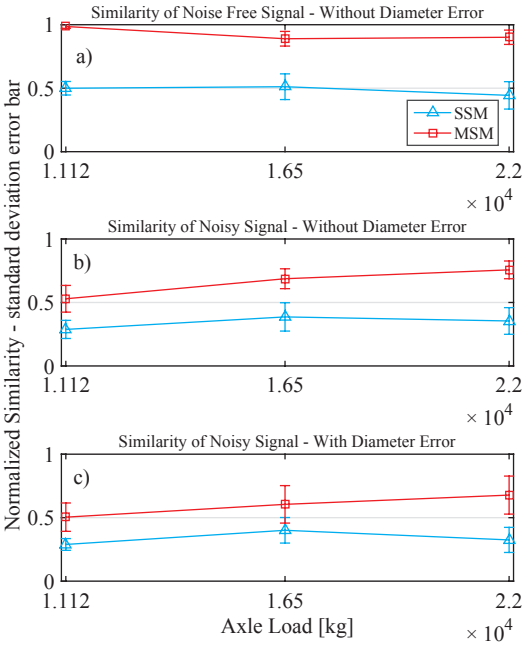

Figure 4.42: The results of the similarity assessment for different axle loads. a) Normalized similarity with standard deviation error bar for noise free signals without diameter error, b) for noisy signals without diameter error, and c) for noisy signals with diameter error.

Therefore, the ratio of the noise to the main signal decreases. As a result, increasing the axle load decreases the effect of the noise and improves the results. This consequence is visible in the similarity and in the velocities estimated of the noisy signals.

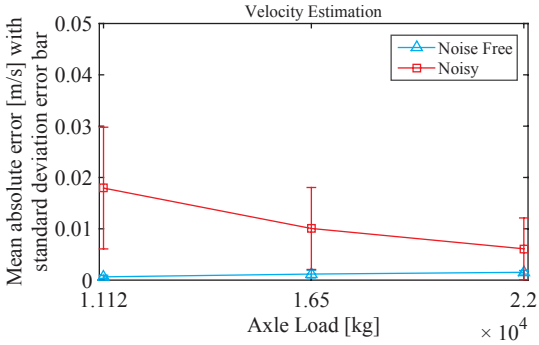

Figure 4.43: The results of the velocity estimation for different axle loads.

4.4. CONCLUSION

Chapter 3 proposed a fusion method to reconstruct a new signal from the data collected by multiple sensors. The output of the fusion process is influenced by several parameters. Some of them affect the input of the fusion process and some of them change the performance of the process. This chapter carried out a detail parametric study to investigate the influential factors to respond to the third key question that is: "*How do the influential factors affect the reconstructed signal?*".

The SSM picks only a single sample per sensor while the MSM exploits all collected samples (of the effective zone) to fill the gaps between the samples used by the SSM. The results showed the effectiveness of the MSM. When the contact force ratio is not relatively large, the rail response variation due to the wheel defect is comparable with the measurement noise magnitude. Therefore, the measurement noise covers the defect signal and decreases the similarity of the reconstructed signal to around 50% from 97%. It shows that the fusion method can give better performance when the SNR is high. As a result, for detecting the minor defects, using the sensors with high SNR are essential. A low pass filter can only be used in the velocity estimation process to cancel out the negative effect of the defect signal and the measurement noise.

Several parameters influence the distribution of the samples over the circumferential coordinate such as sensor interval, wheel diameter, train velocity, length of the effective zone, and number of sensors. In general, increasing the number of sensors improves the results of the fusion process. Therefore, a trade-off is required between the cost of the interrogator supporting high number of sensors, and the accuracy and reliability. In addition, using the sensors with longer effective zone reduces the number of sensors required. Furthermore, the sampling frequency of the sensors limits the maximum velocity of the wheel that can be monitored. In the next Chapter, the reconstructed signals are used to identify the defect type and severity.

5

DEFECT IDENTIFICATION AND CONDITION ESTIMATION[1]

Chapter 3 developed the fusion process to reconstruct an informative signal from the signals measured by multiple sensors. Chapter 4 investigated the influential parameters contributing to the fusion process. The next step is identifying the wheel defect to estimate the wheel condition by attributing the reconstructed signal to the wheel defect. Besides the wheel defect, several other parameters influence the reconstructed signals. The influential parameters can be categorized into two groups. In the first group, the parameters influence the fusion process, and make an imperfect measurement and corrupt the signals reconstructed. Measurement noise, lack of enough number of sensors, and error in estimating the wheel diameter can be mentioned as the parameters of the first group. In the second group, the operational parameters such as the train velocity, and axle load change the signals reconstructed. Variations in these parameters lead to variation in the signals reconstructed even when the defect is kept constant and the fusion process works perfectly. In spite of having perfect reconstruction, the variation in the operational parameters is unavoidable.

This chapter aims to classify the reconstructed signals into different classes of defect types and severities, but the reconstructed signals have out-of-control variations due to the operational conditions. This Chapter tackles the challenge of variation in the signals to attribute the reconstructed signals to the defects. To achieve this purpose, the pattern recognition tools are used to design the required classifier to deal with this classification problem. In supervised pattern recognition, the classifier is trained by available known data to be able to classify new unseen data. This Chapter is organized as follows: Section 5.1 provides an overview on the classification process. In section 5.2, a dataset is generated using VI-Rail for the training and testing steps. Then, section 5.3 explains the features extracted from the reconstructed signals. Section 5.4 investigates the possible classifiers and explains the training process. Finally, section 5.5 presents and discusses the results of the classification process.

[1] This Chapter is partially based on Alemi et al. [80], and [81].

5.1. PROCEDURE OF THE DEFECT IDENTIFICATION

The primary wheel condition monitoring system (WILD) was used to detect detrimental wheels [12]. When the force exceeds a threshold the wheel is classified into detrimental class. Therefore, WILDs are used to keep safe the train movement by classifying the wheels into safe and detrimental classes. Clearly, the detrimental wheels are defective while the safe wheels can be defective or healthy. From the wheel point of view, the classification problem can be presented as the wheel defect detection that classifies the wheels into two classes: healthy and defective wheels. The defective wheels should be classified into different classes containing different defect types and severities. Therefore, this classification is called here, the defect identification. This classification can be more complex by considering several defects with different severities.

The procedure of learning from data with known class labels to classify new unseen data is called supervised pattern recognition [82]. To build a classification problem from the wheel defect identification problem, the pattern recognition terminologies are adapted. In this case, the signals reconstructed from different defect types and severities are called objects (patterns). The objects generated by similar defect type and severity build a class. Therefore, each class refers to an individual defect type with a certain severity. For example, the signals reconstructed from a flat with 40 mm length build a class. These signals can be measured with different velocities or various loads, but all of them are assigned to the same class. Moreover, the signals reconstructed from a flat with 60 mm length, in spite of having similar defect type, have different severity and build another class. The objects from all classes build a dataset. These classes should be defined based on the needs of the potential users of the classification results. Therefore, this method can be generalized to more classes containing more defect types and severities.

An object with the class label is called the known data. When the class of an object is unknown, the object is called an unseen data. The classifier can be trained by learning from known data to classify unseen data. To train a classifier, the objects should be encoded by some features. For example, the signals can be represented by some statistical features such as average, peak, RMS, skewness, kurtosis, and crest factor. Figure 5.1 presents an example of a classification problem based on two features. Figure 5.1a illustrates the distribution of 21 objects based on average force as a feature (F_1). In this examples, among 20 known objects, 10 objects (stars) belong to class 1, and 10 objects (circles) belong to class 2, and one object has unknown class. In Figure 5.1b, the objects are represented by another feature, peak force (F_2). The purpose of the classification is to assign the unseen object to the right class using the known data. According to Figure 5.1a, and b, classifying the unseen object is difficult. Figure 5.1c presents a 2-dimension scatter plot using both features. By representing the objects using average force (F_1) and peak force (F_2) as the required features, a classifier can be trained by the known objects to make a separation line between two classes. Using this classifier, the unseen object can be classified to class 1. By increasing the number of features the classification performance can be improved, but selecting too many features leads to curse of dimensionality, and more objects are required to train the classifier. Therefore, making a trade-off between the feature size and the complexity is essential.

The classification process is generally a classifier training using the features of the known data, and classifying the objects with unknown class labels using the classifier

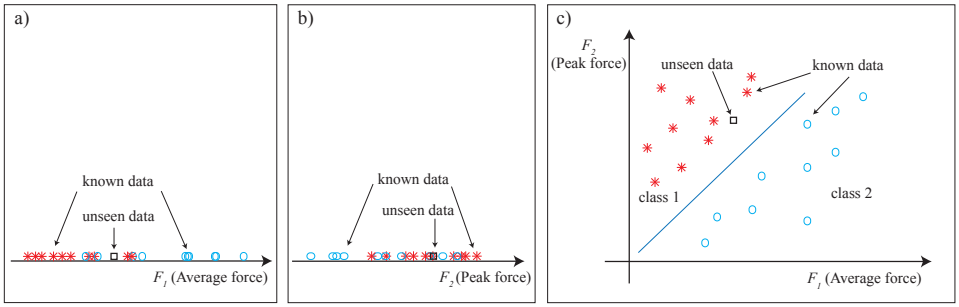

Figure 5.1: An illustration of two classes problem represented by two features. a) The plot of the classes by feature 1, b) by feature 2, and c) a scatter plot by both features.

trained. Defining the informative features to represent the objects is a crucial task. Chapter 3 developed the fusion model to generate a pattern to provide more informative features. The supervised pattern recognition can be used when a set of data from each class is available. Critical systems are not allowed to reach the failure. Therefore, there is no defect data to train classifiers for those systems. Since the measurement from the wheel defects such as flat, and out-of-roundness is possible, the supervised pattern recognition can be investigated for the wheel defect classification.

Figure 5.2 presents the procedure of the wheel defect classification. In Figure 5.2a, VI-Rail simulates the wheel-rail interaction, and then the fusion model reconstructs a signal from the multiple signals generated by multiple sensors (See Chapters 3, and 4). To provide a dataset, defects with different types and severities should be considered as different classes. These classes together with a healthy class, construct the possible classes for objects. Each class should have several objects to be used for training the classifier and testing the unseen data. The characteristic of defect in each class are fed to VI-Rail to model the wheel-rail interaction to give multiple signals. The fusion process reconstructs a new signal from the multiple signals. The reconstructed signals vary by variation in train velocity, and axle load. Therefore, the data generation process should be repeated for different velocities, and axle loads. The objects from all classes build a dataset. Therefore, for each class, several objects (signals) are generated that construct a dataset as the output of the data generation step.

The dataset generated is divided into two subsets to use for training and testing the classifiers. In Figure 5.2b, one subset of the dataset is used for training the classifiers. In the feature extraction step, the reconstructed signals (objects) are encoded by features. These features should represent the characteristics of the reconstructed signals to use as a specific view of the defects. The features are exploited to train the classifiers. The output of this step is a classifier. Finally, the trained classifiers should be able to classify the unseen subset of the dataset. Since the labels of the unseen subset are already known, the performance of the classifier can be evaluated.

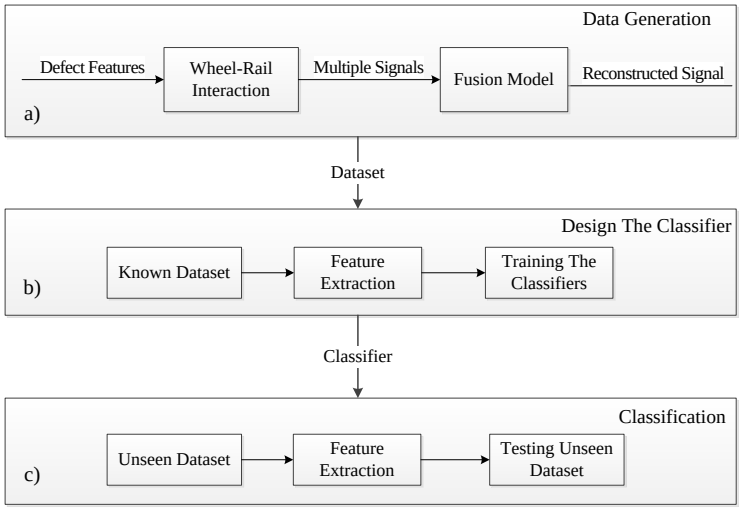

Figure 5.2: The procedure of the wheel defect classification.

5.2. DATASET GENERATION FOR TRAINING AND TESTING

Wheel-rail interaction is simulated by VI-Rail to generate the required data. The procedure of the data generation using VI-Rail has been presented in Figure 4.2. The same as the previous chapter, the simulations are carried out for a passenger vehicle based on the Manchester Benchmarks [77]. The parameters of the track and vehicle have been presented in Tables 4.2 and 4.3.

In the first step of the data generation procedure, the defect model generates the defect on the wheel. VI-Rail simulates the wheel-rail interaction and calculates the contact force and then the vertical rail to sleeper displacement signals. Therefore, as the output of the VI-Rail simulation. Table 5.1 presents the value of the parameters used in the data generation process.

Two types of defects are considered: flat and periodic out of roundness (OOR). The flat defect includes two severities, 40 and 60 mm length, and the periodic out of roundness is a 3rd order out-of-round wheel with 0.3 mm amplitude. These defects plus a healthy wheel construct four condition classes. Figure 4.13 presented the examples of each class. To generate the variation within the classes, two axle loads (11 and 13 tons) and seven velocities (10, 15, 20, 25, 30, 35, and 40 m/s) are considered. Therefore, each class has 14 signals (objects) and the dataset has 56 objects for four classes.

Figure 5.3 presents the signals generated by two defects, a 60 mm wheel flat and a 3rd order periodic out-of-round wheel, for different velocities and for two axle loads. The top row contains the signals generated by 11 tons axle load and the bottom row by 13 tons. Increasing the axle load from 11 to 13 tons, increased the rail to sleeper displacement

Table 5.1: The value of the parameters used in the data generation process.

Parameter	**Value**
Wheel diameter	850 mm
Defect type	40 and 60 mm flats 3rd order periodic out-of-round
Number of sensors	50
Sensor interval	600 mm
Train velocity	10-40 m/s
Train axle load	11120 and 13000 kg
Sensor sampling frequency	10 kHz
Length of effective zone	60 mm

for both defects (shift the signals). For the wheel flat, increasing the train velocity in this range generally reduces the effect of defect and the magnitude of the patterns, while for the periodic OOR wheel, increasing the train velocity increases the effect of defect and the magnitude of the patterns. Figure 5.3 demonstrates the variations of the signals due to the variations in the operational conditions such as load and velocity. The reconstructed signals presented in Figure 5.3a belong to the same condition class and build a class, and this is the case for Figure 5.3b as well. In each class, the objects have considerable variations in magnitude, but they have similar patterns in general. The objects should be encoded by defining good features to represent these similarities. The next Section explains the feature extraction method.

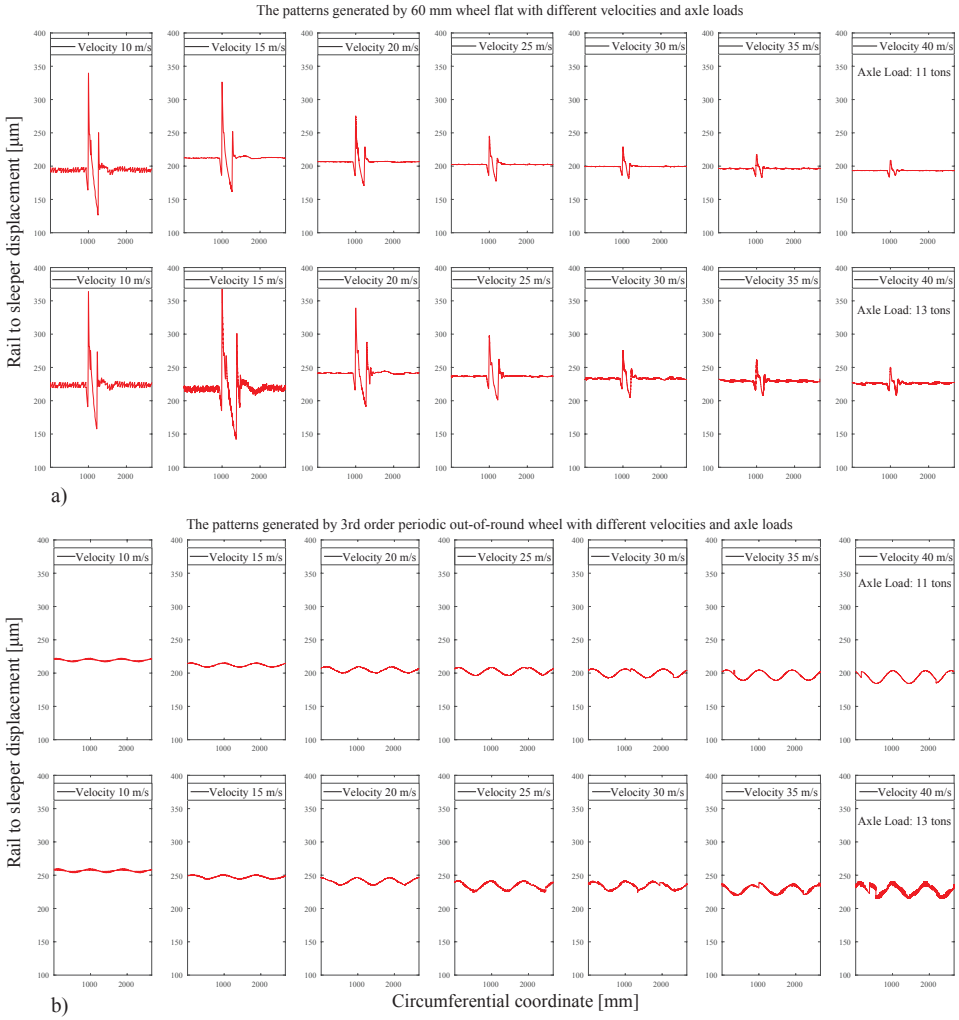

Figure 5.3: The main signals generated by a) a 60 mm flat b) a 3rd order periodic out-of-round wheel with different velocities from 10-40 m/s and for two axle loads, the top row 11 tons and the bottom row 13 tons.

5.3. FEATURE EXTRACTION FROM RECONSTRUCTED SIGNALS

Three common statistical features for estimating the wheel condition are the peak value, dynamic value, and the ratio of the peak to the average, that have been explained in section 2.3.5. Each of these features is an individual number that quantifies the wheel condition. As mentioned earlier, the train velocity and the axle load influence these numbers. Usually, these numbers are used with some thresholds to classify the wheels into two detrimental and safe classes [14]. In this research, these values are used as the statistical features to train the classifiers and to classify the wheels into different classes.

The fusion process makes a pattern from the samples and provides the possibility of extracting more features from the patterns than the simple statistical features. The features should be defined based on the characteristic of the reconstructed patterns (ψ_s) to allow the classifiers to distinguish the patterns. For example, the signals in Figure 5.3a have heart pulse patterns and the signals in Figure 5.3b have sinusoidal patterns. According to the shape of the patterns, different features can be extracted. In this Chapter, the data has been simulated by VI-Rail and can be varied from the field data, because the dynamic properties of the track and train determine the dynamic response of the track and consequently the signals measured. Therefore, the shape features are not investigated in this research.

Another general approach for representing the patterns is considering them as vectors. In this way, the samples of the reconstructed signals (ψ_s) are used as the required features. For example, consider the example presented in section 4.3, in which the data has been collected by $M = 59$ sensors for a wheel with 2670 mm circumference, and 30 m/s velocity. The length of effective zone was 60 mm and the sampling frequency of the sensors was 10 kHz. Therefore, the sensors collected $N = 20$ samples in their effective zones (See Equations 3.21 and 3.22). Accordingly, the reconstructed signal (ψ_s) has $N \times M = 1180$ samples that have been distributed non-uniformly over the circumference (See Section 3.4.2). The interpolation of the reconstructed signal with 1 mm interval gives a signal with 2670 samples with uniform distribution. The representation of the interpolated signal ($\psi_s^*(k)$) is a K-dimensional vector with $K = 2670$ features. A comparison between the results of the classification using the statistical features and the vector features, investigates the effectiveness of the reconstruction method.

When the interpolated signal is considered as the main signal, several other signals can be obtained to be investigated as the features to may lead to better results. To reduce the effect of axle loads, the *Dynamic Signal* and the *Ratio Signal* can be defined. The dynamic signal is generated by subtracting the average of the signal. The ratio signal is the ratio of the signal to its average. The dynamic signals of the 60 mm wheel flat and the periodic OOR wheel are presented in Figure 5.4. These signals have zero average and perfectly show the effect of defects and velocity. Another signal is *Normalized Signal* is generated by subtracting the average of the signal and dividing by the standard deviation of the signal that gives a dimensionless signal. Each of these signals has K features. Table 5.2 presents the formula of different features with the size of their feature vector. Figure 5.5 presents the normalized signals that reduced the effect of velocity in addition to the axle load.

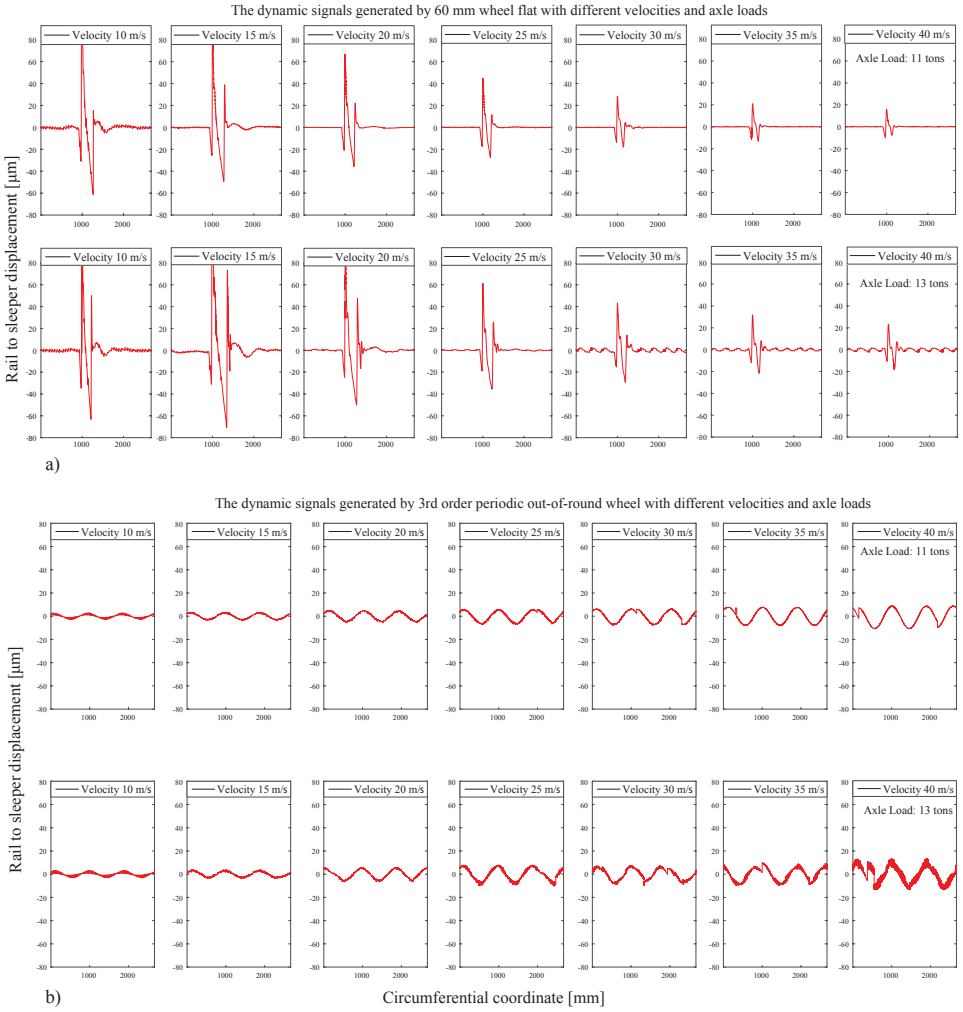

Figure 5.4: The dynamic signals generated by a) a 60 mm flat b) a 3rd order periodic out-of-round wheel with different velocities from 10-40 m/s and for two axle loads, the top row 11 tons and the bottom row 13 tons.

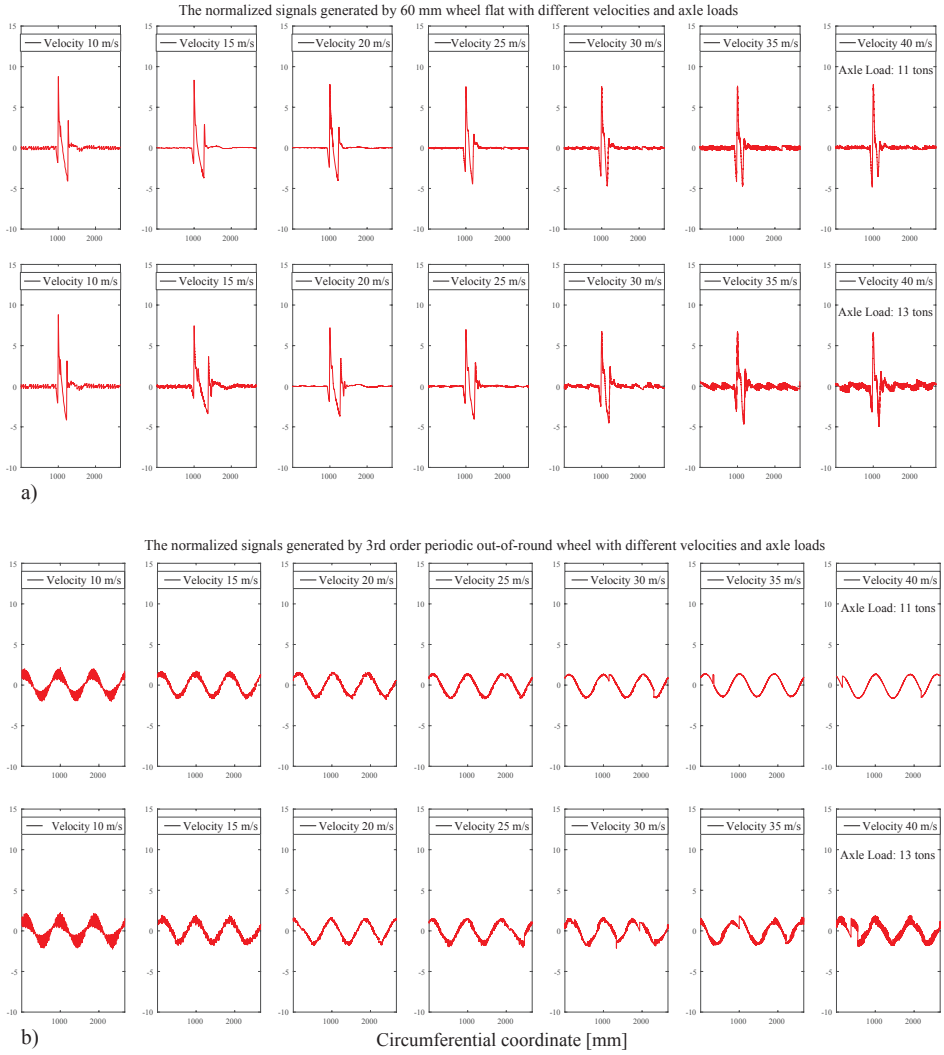

Figure 5.5: The normalized signals generated by a) a 60 mm flat b) a 3rd order periodic out-of-round wheel with different velocities from 10-40 m/s and for two axle loads, the top row 11 tons and the bottom row 13 tons.

Table 5.2: The definition and formula of different features.

Name	Formula	Size
Peak Value	$\arg\max_k \psi_s$	1
Dynamic Value	$\arg\max_k \psi_s - \mu_s$	1
Ratio Value	$\frac{\arg\max_k \psi_s}{\mu_s}$	1
Main Signal	$\psi_s^*(k)$	K
Dynamic Signal	$\psi_s^*(k) - \mu_s$	K
Ratio Signal	$\frac{\psi_s^*(k)}{\mu_s}$	K
Normalized Signal	$\frac{\psi_s^*(k) - \mu_s}{\sigma_s}$	K

5.3.1. PREPROCESSING AND DATA ALIGNMENT

As mentioned earlier, the first preprocessing step in the feature extraction procedure is the interpolation of the signals. In this step, the signals are interpolated in the same range of discrete points with an identical interval. This interpolation determines the number of features. To avoid the curse of dimensionality, the interval is defined 1 mm.

The position of the wheel defect with respect to the sensors is out of control. Therefore, the defective area can be positioned in different locations over the circumferential coordinate in different measurements. In the second step of the feature extraction procedure, the signals are rotated over the circumferential coordinate to be aligned with respect to each other. In this research that the wheel circumference is 2670 mm, the patterns are rotated to the extent that the maximum of each signal is positioned in the position 1000 mm. Figures 5.3, 5.4, and 5.5 have presented the signals after the interpolation and alignment.

5.4. TRAINING PROCESS AND CLASSIFIER SELECTION

This Chapter uses a dataset generated by the simulated data to train the classifiers. The simulated data can be extensive and the classifiers can be trained well, but from the practical point of view, collecting data from defective wheels is costly. Therefore, the training set should be small as much as possible. In addition, the signals have high dimensional feature spaces. As a result, a Support Vector Classifier (SVM) can be a good choice that works well on datasets containing low sample sizes with high dimensional feature spaces [83]. In addition, k-nearest neighbour classifier (kNN) can be another non-parametric method using the neighbours of an object to assign it to the most common class [84].

In the case of small training set, the overfitting is a considerable challenge. Figure 5.6 presents the averaged learning curves of the Dynamic Signal for SVM, 1-NN and 3-NN classifiers after 40 repetitions. As mentioned earlier, the dataset has 56 objects. In each repetition some objects are selected as the training set to train the classifier and

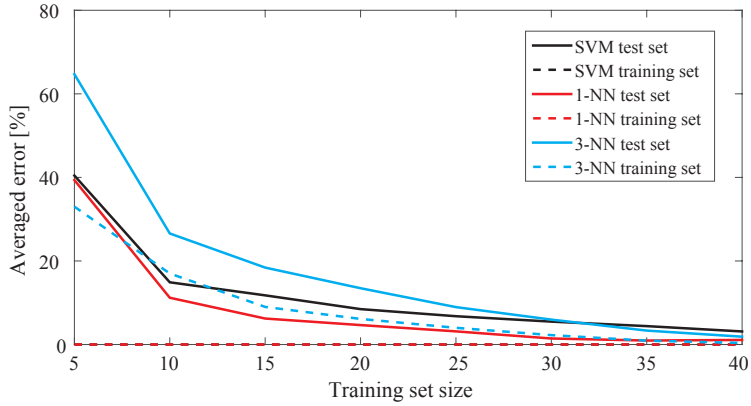

Figure 5.6: The average error of SVM, 1-NN, and 3-NN for different sizes of the training set after 40 experiments for the Dynamic Signal.

others are used for testing. In Figure 5.6, the horizontal axis shows the number of objects used for training. According to this Figure, by increasing the number of objects used for training the classifiers, the classification errors decrease. For example, by using 40 objects for training, the classifiers give less than 10% errors. Therefore, it is expected that these three classifiers can deal with this problem. The errors on the training set (apparent error) for SVM and 1-NN are zero (dashed lines). The distance between the solid and dashed lines is overfitting. For smaller training set, the 3-NN classifier performs with less overfitting. As a result, these three classifiers are selected to be tested in the next Section.

5.5. TESTING AND CLASSIFICATION RESULTS

Table 5.2 described seven different methods for representing the wheel condition. Three typical statistical feature extraction methods (the peak value, dynamic value, and the ratio of the peak to the average) provide an individual number and four new methods use the reconstructed signal to represent the condition state containing many features. A comparison between the statistical features and the new signal features demonstrates the effectiveness of the proposed methods. To investigate the classifiers a 10-fold cross validation is performed. Accordingly, the classifiers are trained on nine subsets and are tested on the remaining subset. The selection of the train set and test set is random. Therefore, the process is repeated 20 times and the average error and its standard deviation are presented. Table 5.3 presents the average errors and the standard deviation of the errors after 20 repetitions for three classifiers and for seven different feature extraction methods. The classification results demonstrate a considerable difference between the signal features, and value features. The classifiers trained by signal features classify the defects perfectly, while the classifiers based on the value features gives poor performance. For example, the 1-NN classifier using the dynamic signal classified the signals

Table 5.3: A comparison between different classifiers and feature methods by the average and the standard deviation of the classification errors. The horizontal bars represent the magnitude.

Feature	Classifier	Error [%]	Standard deviation of the error [%]
Peak value	SVM	74.98	0.03
	1-NN	79.2	3.31
	3-NN	77.09	3.35
Dynamic value	SVM	59.06	0.11
	1-NN	22.04	2.88
	3-NN	22.8	1.54
Ratio value	SVM	74.99	0.02
	1-NN	23.1	2.89
	3-NN	23.13	2.44
Main signal	SVM	3.93	1.82
	1-NN	65.04	2.99
	3-NN	61.39	4.26
Dynamic signal	SVM	2.15	0.95
	1-NN	0.25	0.64
	3-NN	2.18	0.63
Ratio signal	SVM	13.75	1.84
	1-NN	0.29	0.57
	3-NN	2.26	0.79
Normalized signal	SVM	1.57	1.03
	1-NN	0.93	0.82
	3-NN	0.55	0.63

with 99.75% performance (0.25% error).

Table 5.4 provides the detail information of the classification error of the SVM for the first cross validation of the Dynamic Signal. Based on the confusion matrix, a 60 mm flat defect was assigned to the class of 40 mm flat. More investigation revealed that the mistake is due to the 60 mm flat with 10 m/s velocity, in which, the dynamic force is not high enough and the 60 mm flat looks like a 40 mm flat.

As it has been discussed in Chapter 4, in addition to the wheel defect, several other parameters influence the reconstructed signals. The operational parameters such as the train velocity, and axle load vary the signals reconstructed, while the measurement noise, and error in estimating the wheel diameter make an imperfect measurement and corrupt the signals reconstructed. The classifiers perfectly responded to the variation of the signals due to the variation of the train velocity, and axle load. In Chapter 4, the influential parameter on the fusion process have been discussed. Two main parameters influenced the fusion results are the measurement noise, and error in estimating the wheel diameter. The following subsections investigate the performance deterioration of the classifiers due to the measurement noise, and error in estimating the wheel diameter.

Table 5.4: The confusion matrix of the SVM classifier for the Dynamic signal.

		Estimated Labels				
		Healthy	60 mm flat	3rd order OOR	40 mm flat	Totals
True Labels	Healthy	14	0	0	0	14
	60 mm flat	0	13	0	1	14
	3rd order OOR	0	0	14	0	14
	40 mm flat	0	0	0	14	14
Totals		14	13	14	15	56

5.5.1. CLASSIFICATION OF NOISY SIGNALS

In the previous section, the noise free data generated by VI-Rail has been directly fed to the fusion process (See Figure 5.2). To investigate the robustness of the classifiers performance with respect to imperfect measurements (reconstructions), a set of White Gaussian Noises, similar to the noise presented in section 4.3.2, is added to all signals generated by VI-Rail. Then, the fusion process reconstructs signals using the noisy data. As a result, a dataset from four condition classes is generated that has 56 noisy objects. The classifiers are trained by a subset of this dataset and are tested on the remaining subsets. Since the noise has a random nature, the process is repeated 9 times to evaluate the average effect of the noise. It means that in each repetition, a new set of noises is added to the generated signals and the fusion process reconstructs signals using them. In addition, each dataset is evaluated by 20 repetitions of a 10-fold cross validation.

To assess the performance degradation of the classifiers due to the presence of measurement noise, the process is repeated for different noises. Figure 5.7 presents the dynamic signals for different noises. Figure 5.8 depicts the variation of the classification error for different measurement noises using Main signal, Dynamic signal, Ratio signal, and Normalized signal for 1-NN, 3-NN, and SVM classifiers. The results are the average error of 9 time repetition with the corresponding standard deviation. Generally, the classifiers have presented a robust performance with respect to the measurement noise, since they have been trained by the noisy objects and tested on the noisy objects. When the Main signal is used, the NN classifiers made around 65% errors, and increasing the measurement noise had minor influence on that. The Normalized signal is sensitive to noise and the errors of the NN classifiers increased to 20% by increasing the noise. The classification by SVM contained around 15% errors with a consistent performance in presence of increasing noise. The Dynamic signal provided small errors and a satisfactory performance when was used by different classifiers.

5.5.2. CLASSIFICATION OF SIGNALS WITH DIAMETER ESTIMATION ERROR

Wheel diameter (circumference) is a fundamental value used in the fusion process, and the error of this value leads to imperfect reconstruction. Wheel diameters can be provided from different sources, but Chapter 3 proposed a method to estimate the wheel diameter using the data measured. Regardless of the method used for providing the wheel diameter, the error of this value influences the reconstruction process, and consequently the classification results. This section investigates the performance deterioration of the

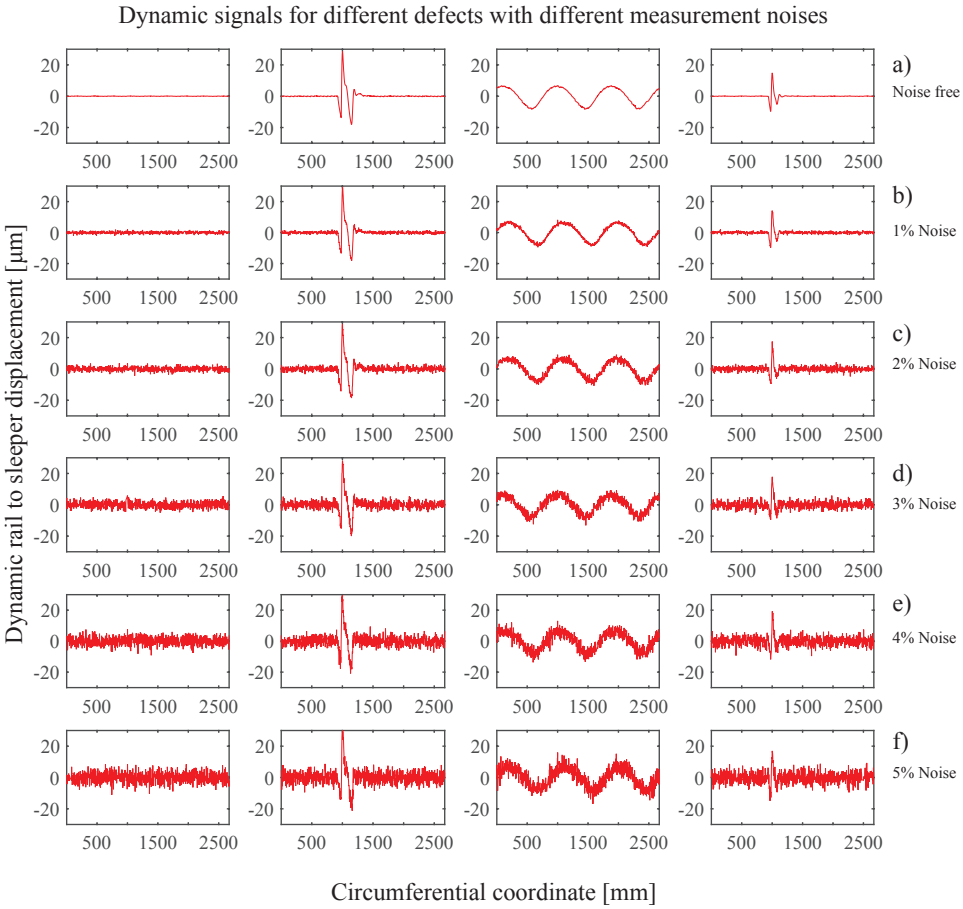

Figure 5.7: Dynamic signals for different defects with 30 m/s velocity and different measurement noises.

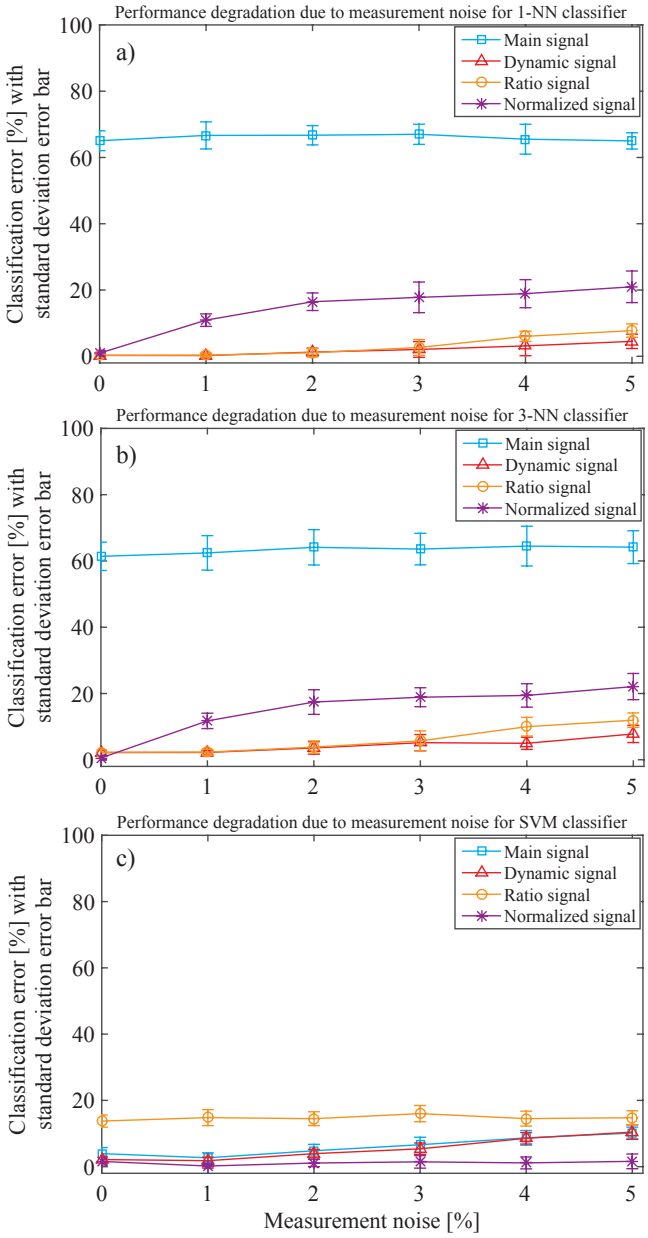

Figure 5.8: Classification error for different measurement noises using Main signal, Dynamic signal, Ratio signal, and Normalized signal for a) 1-NN, b) 3-NN, and c) SVM classifiers.

classifiers due to error in estimating the wheel diameter.

The fusion process reconstructs the signals with errors to generate the required dataset. Then, the dataset is evaluated by 20 repetitions of a 10-fold cross validation. Figure 5.9 presents the variation of the classification error for different diameter errors using Main signal, Dynamic signal, Ratio signal, and Normalized signal for 1-NN, 3-NN, and SVM classifiers. The results show that increasing the diameter error increases the classification error.

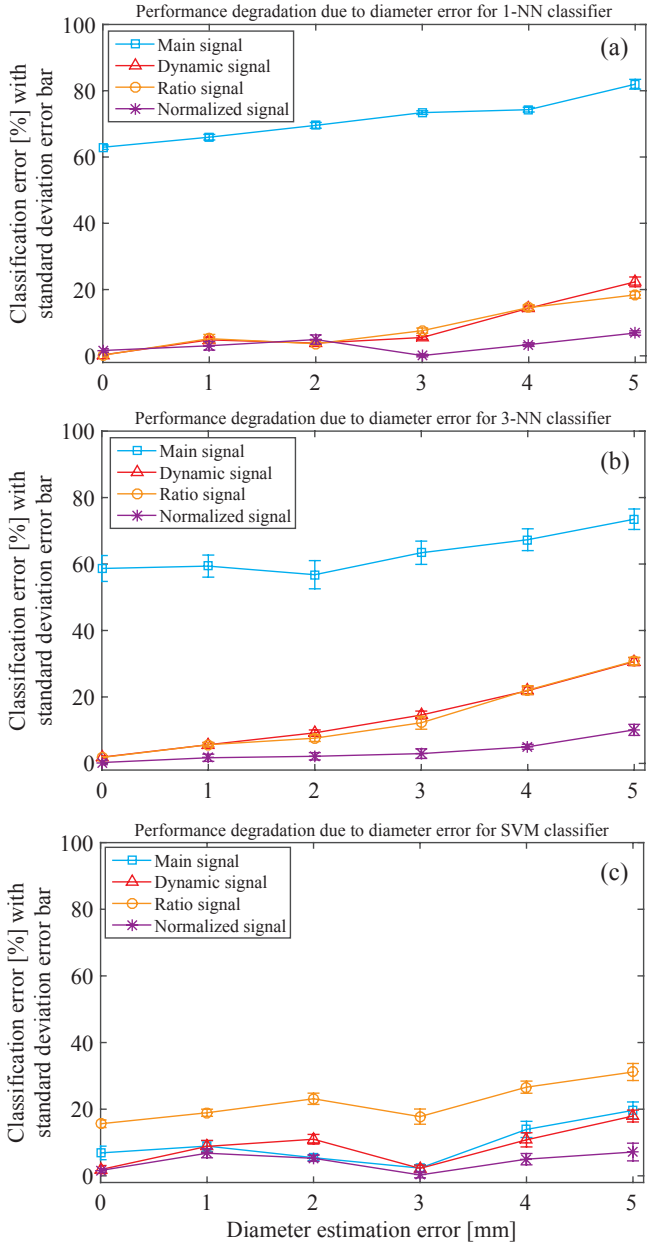

Figure 5.9: Classification error for different diameter errors using Main signal, Dynamic signal, Ratio signal, and Normalized signal for a) 1-NN, b) 3-NN, and c) SVM classifiers.

5.6. CONCLUSION

This Chapter answered to the corresponding research question: "*How can the defect types and their severity be detected?*". Train velocity, and axle load vary the signals reconstructed. In addition, some parameters such as measurement noise, and error in estimating the wheel diameter corrupt the signals reconstructed. Therefore, pattern recognition methods were used to train the classifiers and test the unseen data. This Chapter used a dataset containing 56 reconstructed signals to classify the wheels into four classes. The results showed that the wheels can be perfectly classified with more than 99% performance using dynamic signals. This demonstrates the effectiveness of the reconstruction method in generating the informative signals to use for classifying the defects. The comparison of results showed that the classification using the reconstructed signals give better performance than the classification using the statistical features such as peak force. The robustness of the process was also evaluated by considering the measurement noise and the diameter estimation error. The results indicated that the classifiers are robust enough to deal with these imperfections.

6

EXPERIMENTAL VALIDATION OF DATA FUSION MODEL AND DEFECT IDENTIFICATION[1]

Chapter 3 developed the fusion model to reconstruct an informative signal from the multiple signals measured by the multiple sensors. In chapter 4, the fusion model has been tested using the data simulated by VI-Rail. Chapter 5 developed a defect identification model using the pattern recognition methods to classify the defective wheels by estimating the defect type and severity. The defect identification model used the simulated data to generate the dataset and test the model. This chapter validates the fusion method and the defect identification model using the data generated by laboratory tests. Due to the lack of experimental facility, a new test rig has been designed and constructed to model the wheel-rail interaction and to generate the real data required for the data fusion model and the defect identification model.

This chapter, in section 6.1, explains the structure of the new test rig. In this test rig, a rotating arm moves a wheel over a circular rail that is supported by sleepers. According to this symmetric configuration, six strain sensors have been mounted under the rail with constant intervals to measure the rail bending strain. The strain sensors measure different portions of the wheel in discrete points. In section 6.2, the fusion model reconstructs patterns from the data collected by the multiple strain sensors for different wheel defects. By reconstructing the informative patterns correlated to the wheel defects, the fusion model is validated. In section 6.3, a dataset is generated using the data collected from a set of laboratory tests as the input of the defect identification model. This data is used in the training and testing steps in the classification process. Different wheel defects including the flat and out-of-round wheels with different loads and velocities are tested and the results validate the defect identification model by classifying the wheels into different classes of defects.

[1] This Chapter is partially based on Alemi et al. [85].

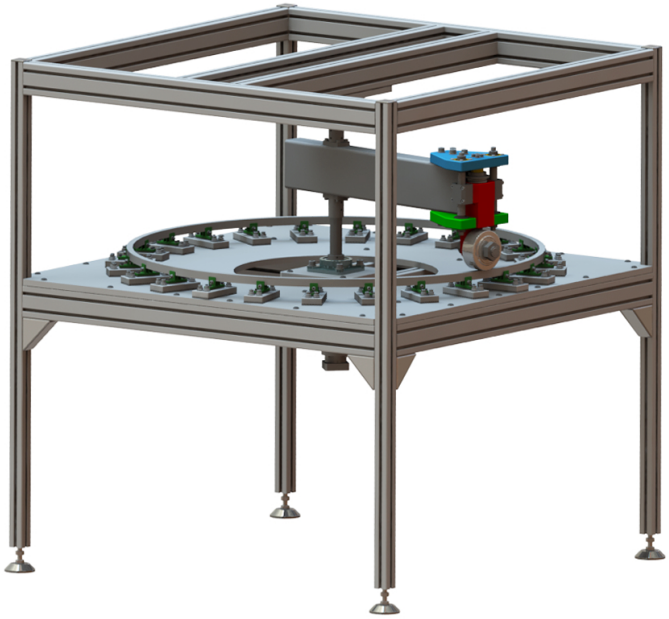

Figure 6.1: The schematic view of the test rig used for modelling the wheel-rail interaction.

6.1. TEST RIG DESIGN

Several test rigs such as described in [21], [86], [87], [88] have been constructed to model the wheel-rail interaction to provide variety of data for different purposes. For example, Armstrong and Thompson made a reduced scale circular model to investigate rolling noise [86]. Liang et al. [21] used a roller rig to model wheel-flat and rail surface defect. Since the access to these facilities were restricted or the nature of the test rigs were not fitted to the data fusion model, a new test rig has been designed. This section provides a detailed explanation about the new test rig constructed to generate real data by modelling the wheel-rail interaction. Figure 6.1 shows the schematic view of the test rig consisting of a rail, rotating arm, wheel hub, spring, wheel, motor, sleepers, clamps, and rubbers. The specifications of the test rig components are presented in Table 6.1.

The rail had a rectangular profile with 20 mm height and 15 mm width. The circular rail was connected by clamps to 24 sleepers to transfer the wheel load to the bottom plate. The clamps, sleepers, and the bottom plate were screwed with a piece of rubber in between. This structure and the motor were mounted on a frame with dimensions of about 120×120 mm. The rotating arm was connected to the motor through a shaft. The wheel velocity is adjustable by the motor drive. Another side of the rotating arm had the wheel hub to hold the wheel. Figure 6.2 shows the magnified view of the wheel hub and wheel-spring-arm connection. The load of the wheel on the track is adjustable using a spring connected to the wheel hub. Turning the nut above the spring pushes the wheel hub, and consequently the wheel down. Figure 6.3 shows final view of the test rig.

Table 6.1: The specifications of the test rig components.

Component	**Specification**
Rail	Aluminium, rectangular profile: 15×20 mm, inner diameter: 992.5 mm, outer diameter: 1022.5 mm
Wheel	Steel, 100 mm diameter,
Sleeper	PVC, 120×50×15 mm,
Rotating arm	Rectangular tube: 120×60×4 mm
Clamp	Aluminium, 60×20 mm
Hub spring	k = 119 N/mm
Hub screw	Pitch: 1.5 mm
Rubber pad	Styrene-butadiene(SBR)
bottom plate	Aluminium, 20 mm thickness

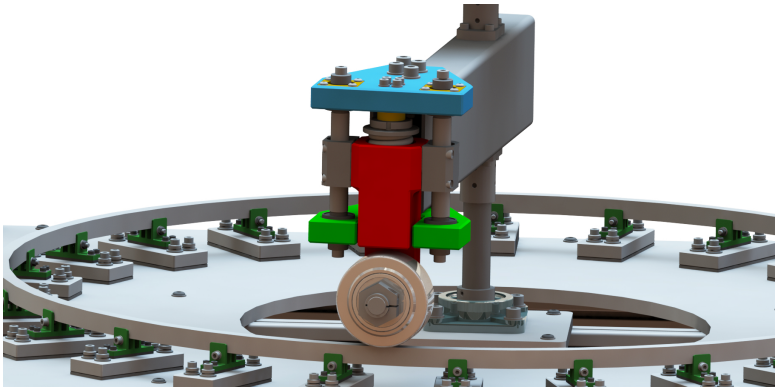

Figure 6.2: The magnified view of the wheel hub.

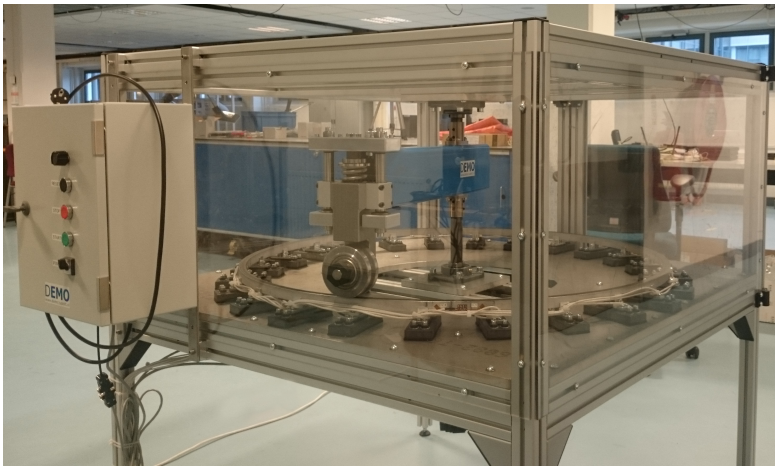

Figure 6.3: The photo of the test rig in laboratory.

6.1.1. SENSOR CONFIGURATION AND DATA ACQUISITION

The track has 24 sleepers with constant intervals. Six general-purpose strain gages were installed under the rail in the bay between the sleepers in the symmetric positions with 60° intervals. The rail was polished and the sensors were directly glued to the rail. The overall length of the sensors was 9.83 mm and gage length was 4.75 mm with linear pattern. These sensors measured the rail bending strain generated by the wheel-rail contact force by 3 kHz sampling frequency. Figure 6.4 presents the schematic top view of the sensors positions, wheel, rail, sleepers and rotating arm. According to this Figure, the sensors were configured with a constant distance. The sensors were connected through an amplifier, and a data acquisition device (DAQ) to a computer. Figure 6.5 presents the configuration of sensors, amplifier, DAQ, and the computer.

6.1.2. WHEEL DEFECT MODEL

Four wheels have been used to investigate the fusion model. Four wheels were tested including a healthy wheel, two flat wheels, and a wheel with periodic out-of-roundness (OOR). The wheels have 100 mm diameter and a convex profile. To make the defects on the wheels, first, three defective wheels were machined to have flat profiles. This process reduced the wheel diameter to 99.01 mm. Then, the defects were made on the wheels. One wheel had a big flat with 6.6 mm length and 0.11 mm depth. Another flat wheel had small flat with 4.4 mm length and 0.05 mm depth. The third defective wheel was a third order periodic OOR wheel with 98.92 mm diameter and 0.08 mm amplitude.

6.1.3. WHEEL LOAD AND VELOCITY

The strain sensors measure the rail bending signal as the response of the rail to the wheel-rail contact force. Since the rail response is influenced by the wheel load and velocity, the wheel load and velocity were kept constant during each measurement. The

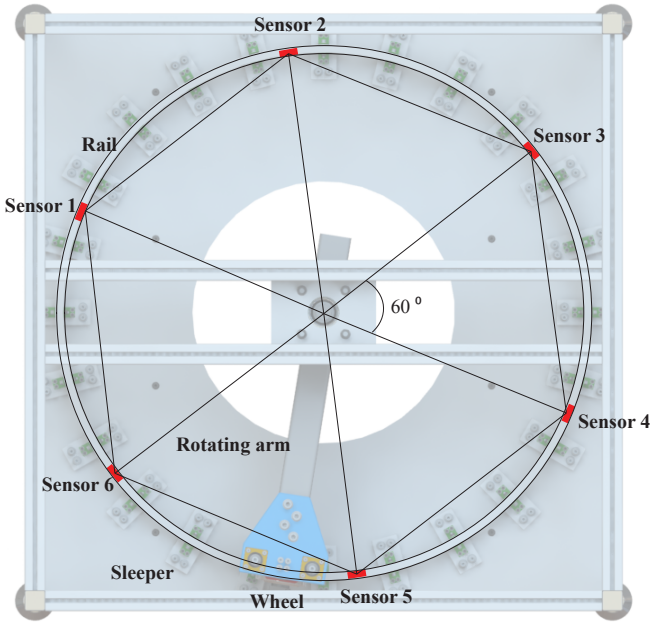

Figure 6.4: The top view of the configuration of six strain sensors installed under the rail.

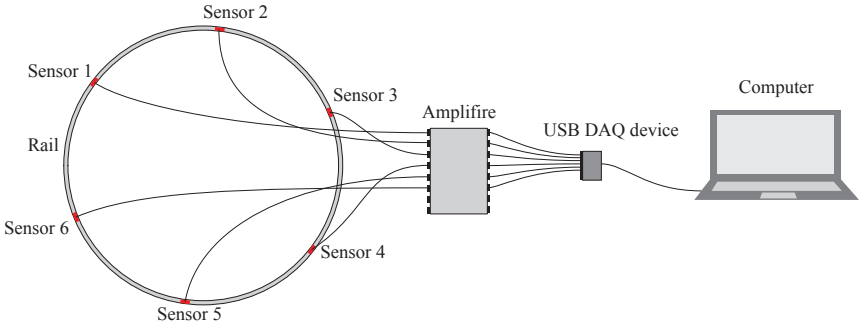

Figure 6.5: The configuration of sensors, amplifier, DAQ, and the computer for data acquisition.

motor drive controls the velocity of the motor and shows the actual velocity of the motor on a screen. A gearbox converts the motor rotation to the shaft rotation with 15:1 gear ratio. Therefore, the rotational velocity of the wheel can be estimated by recording the motor shaft velocity dividing by 15.

The wheel is pressed by the spring force by screwing on the nut above the spring to exert the required contact force. According to Table 6.1, the pitch of the screw is 1.5 mm and the spring constant is 119 N/mm. Therefore, by counting the rotations of the nut multiplying to the pitch of the screw, and the spring constant, the static load of the wheel can be estimated. Next sections investigates the data fusion model, and the wheel defect identification model using the data generated by the test rig.

6.2. EXPERIMENTAL VALIDATION OF THE MULTI-SENSOR DATA FUSION MODEL

The strain gage sensors measure the rail bending response as voltage signals. These signals are voltage variation over time due to the wheel passage. Normally the measured voltage signal is converted to the strain signal and then using a known force is converted to the force signal. The output of the data fusion model is a pattern. Therefore, the raw output of the sensors in voltage was directly used as the input of the data fusion model without converting to strain or force. Figure 6.6 presents the output of a sensor during the passage of the healthy wheel. In this signal, when the wheel is far from the sensor, the output of the sensor is zero. By approaching the wheel to the sensor, the output of the sensor changed. When the wheel is close to the sensor in a way that is not on top of the sensor, the rail goes up and compresses the sensor and provides negative output. When the wheel passes the sensor, the output of the sensor increases to a maximum that depends on the wheel-rail contact force. The shape of this signal depends on the dynamic parameters of the test rig but it is generally comparable to the signal measured from the field tests [48].

When the wheel is healthy and is moving with constant velocity, the signals measured by the multiple sensors will have nearly identical shapes, and magnitudes except having a delay. Figure 6.7 presents the outputs of the six sensors in the first round of the healthy wheel rotation over the sensors. Each sensor measures a portion of the wheel. The magnitude of the peaks in the signals measured by each sensor depends on the wheel-rail contact force and basically on the wheel portion that contacts with rail. When the wheel is healthy, the sensors measure signals with similar magnitude in the peaks.

In this circular test rig, more rotations of the wheel leads to the extension of the number of sensors. On each rotation, 6 sensors sample from the wheel. Therefore, for example, 10 rotations of the wheel equal to sampling with 60 sensors. Figure 6.8 presents the outputs of 60 sensors for the four wheels including healthy, OOR, big flat with 6.6 mm length, and small flat with 4.4 mm length. In this Figure, the sensors provided outputs with variations in the peaks depending the wheel portions contact the rail and sensors. In this test, the velocity of the motor was 300 RPM and the wheel had 20 RPM velocity. The nut was rotated 7 rounds to press the spring 10.5 mm. Therefore, the spring force was around 1.25 kN.

The signals presented in Figure 6.8 make a dataset according to Equation 3.11. Using

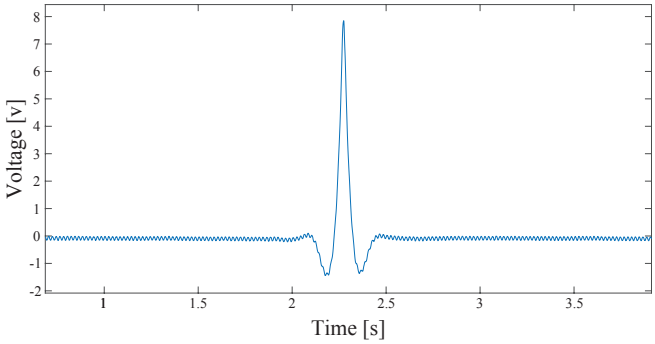

Figure 6.6: The raw output of a strain sensor during the passage of the healthy wheel.

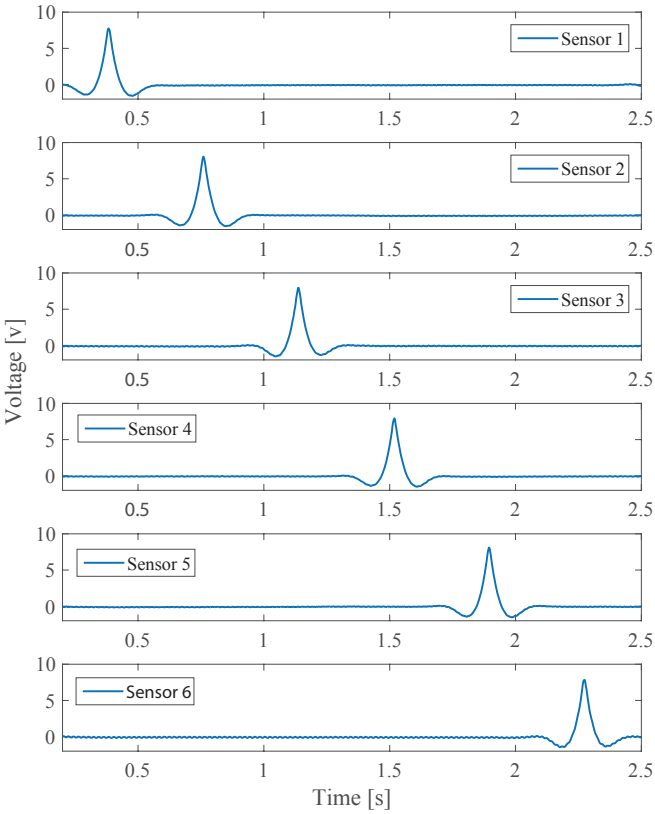

Figure 6.7: The outputs of the strain sensors during the first passage of the healthy wheel.

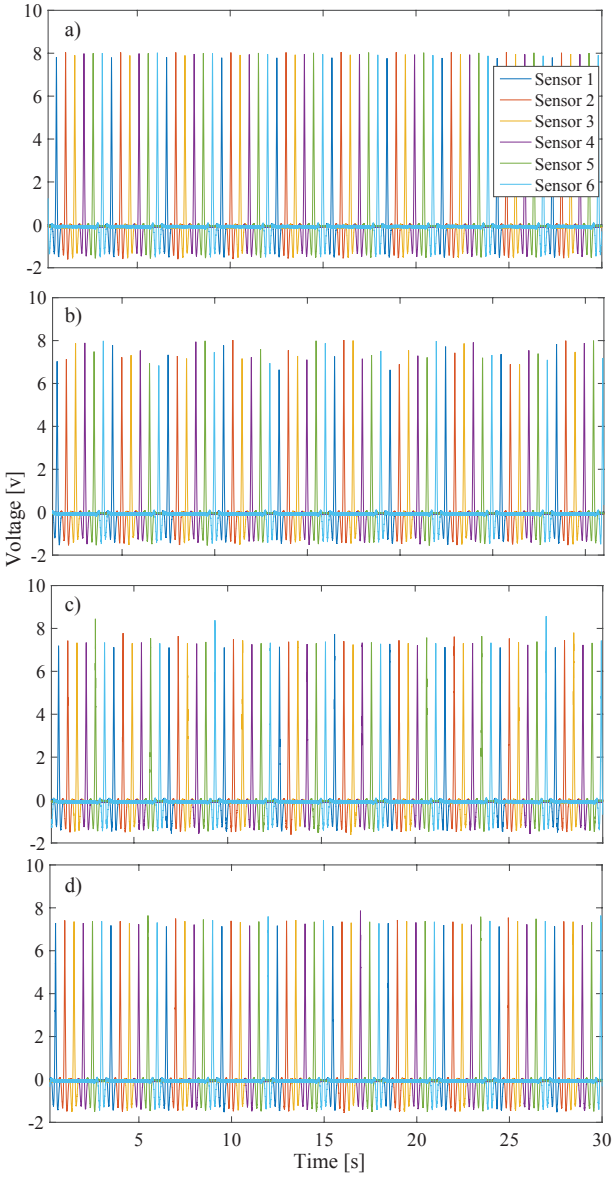

Figure 6.8: The outputs of the 60 sensors for the wheels: a) the healthy, b) OOR, c) big flat with 6.6 mm length, and d) small flat with 4.4 mm length with 20 RPM velocity and 1.25 kN load.

the *MSM* proposed in section 3.3, few samples from the peaks on each signal can be selected to generate a new dataset like presented in Equation 3.14. Figure 6.9 compares the samples measured by 60 sensors after selecting 11 samples per sensor using the *MSM* for different wheels. In Figure 6.9a, the wheel is healthy and the samples have very small deviation from their average. In Figure 6.9b, c, and d that correspond to the OOR and flat wheels, the samples have more deviations from their averages. These deviations acknowledge the existence of the wheel defects but fail in providing detailed insight about the wheel defects.

According to Equations 3.16 and 3.18, the positions of the sensors (X_m) and the wheel circumference (L_w) are required for fusing the collected data. The rail diameter is 1007.5 mm (the diameter of the rail in the middle point between the inner and outer side of the rail). The diameters of the wheels are 100, 99.01, and 98.92 mm. Using the Equations 3.18, and 3.19, the selected samples presented in Figure 6.9, have been fused and mapped over the circumferential coordinate to generate patterns. Figure 6.10 compares the results of the fusion model for four wheels. In this Figure, the length of the signals equals to the wheel circumference. Figure 6.10a shows an almost smooth pattern corresponding to the healthy wheel. Figure 6.10b displays a sinusoidal pattern corresponding to the 3rd order out of round wheel. Figure 6.10c demonstrates a pattern containing big peaks corresponding to the big flat. Figure 6.10d depicts a pattern containing small peaks corresponding to the small flat.

The comparison between the patterns reconstructed in Figure 6.10, and the defects explained in section 6.1.2 shows that the reconstructed patterns provide relevant information about the wheel defects. These results perfectly validate the fusion model and the possibility of generating informative signals from the samples collected by multiple sensors.

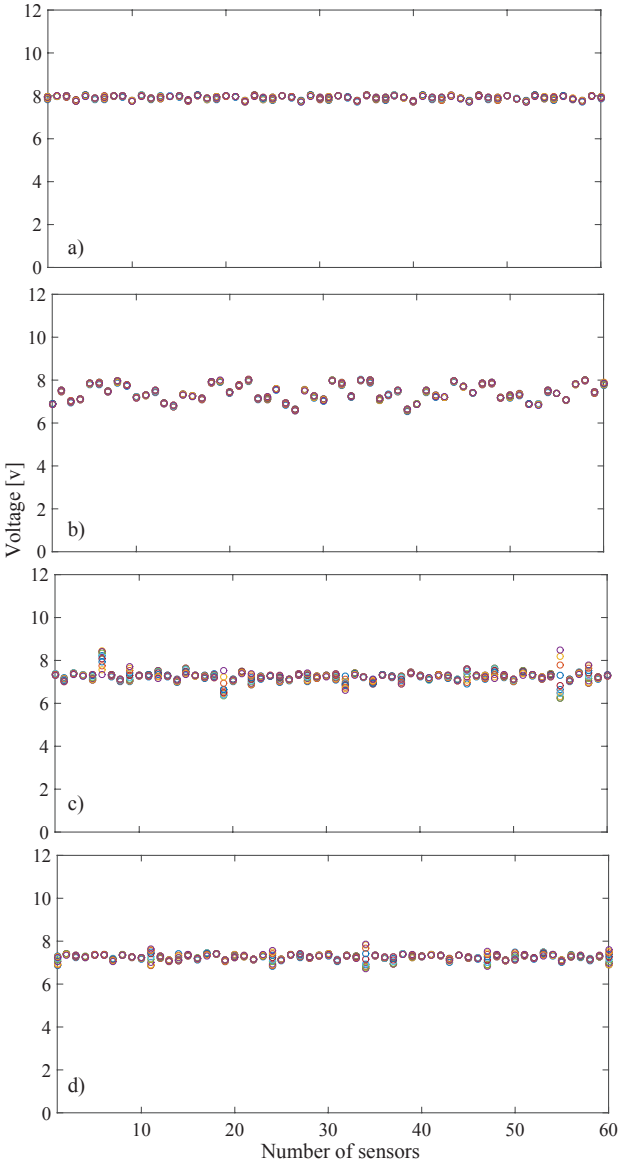

Figure 6.9: The comparison between the samples selected from 60 sensors for a) the healthy wheel. b) the OOR wheel, c) the wheel with big flat, and d) the wheel with small flat.

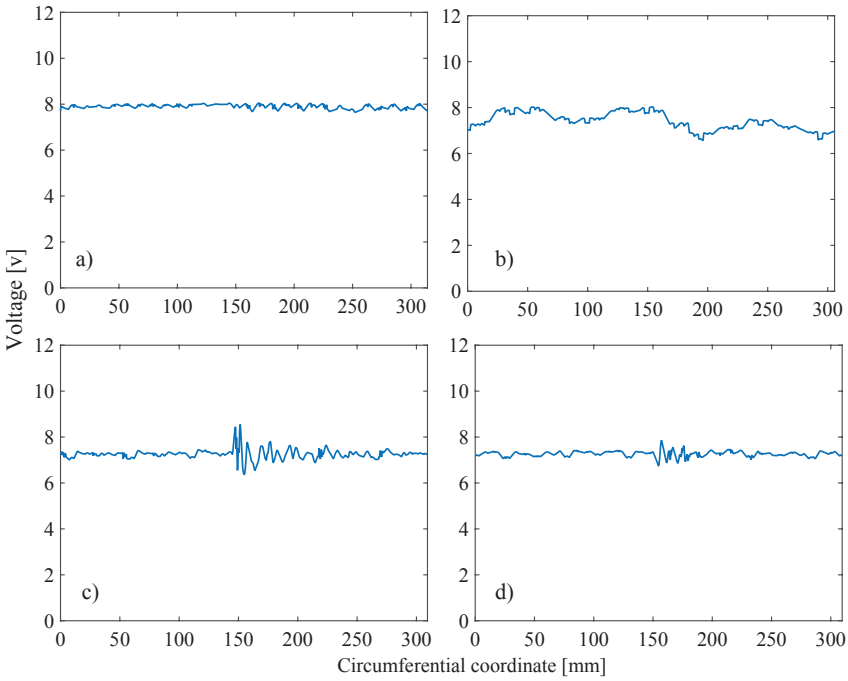

Figure 6.10: The comparison between the patterns reconstructed using the samples collected from 60 sensors for a) the healthy wheel. b) the OOR wheel, and c) the wheel with big flat, and d) the wheel with small flat.

6.3. EXPERIMENTAL VALIDATION OF THE WHEEL DEFECT IDENTIFICATION MODEL

This section follows the pattern recognition procedure used in Chapter 5 to validate the defect identification model. In this section the input of the defect identification model is the signals reconstructed from the real data measured by the test rig.

6.3.1. REAL DATA GENERATION FOR TRAINING AND TESTING

To generate a dataset for training and testing the classifiers, the four wheels with eight velocities and three loads are used. Therefore, the dataset has 96 objects (patterns). Following the previous section, wheel-rail interaction is modelled by the test rig to generate the required data. Three defective wheels with the healthy wheel construct the four classes. The wheel defects have explained in section 6.1.2. The motor velocities are 200, 300, 400, 500, 600, 700, 800, and 900 RPM. Therefore, the wheel velocities are 13.3, 20, 26.6, 33.3, 40, 46.6, 53.3, and 60 RPM. The wheel loads are 1.07, 1.25, and 1.6 kN.

Chapter 4 in section 4.3.5 discussed the influential parameters on the distribution of the samples over the circumferential coordinate. This distribution is determined by the different parameters such as the sensor interval, wheel diameter, length of the effective zone, number of sensors, and the wheel velocity. In these experimental tests, the length of the effective zone is 5 mm, and the wheel velocities and diameters are known. Since the test rig has a circular structure, any changes in the wheel-rail contact point change the passing curve of the wheel and consequently the sensor intervals. The middle point of rail has 1007.5 mm diameter. As it is expected, the measurements showed that the contact point varied between 1004.5 to 1008 mm depending on the wheel velocity and load, due to wheel slip on the circular rail. Therefore, the rail circumference varied between 3155.7 to 3166.7 mm and as a result, the sensor intervals varied between 525.9 to 527.7 mm. For this specific sensor configuration, the distribution of the samples collected by the sensors can be simulated to determine the required number of sensors to cover the wheels circumferences.

The parametric study in the section 4.3.5 showed that the maximum distance between the consecutive samples over the circumferential coordinate should be smaller than 5 mm for reconstructing the defect signal without any distortion. The required number of sensors can be determined by considering the wheel diameters, 100, 99.01, and 98.92 mm, and sensor intervals, 525.9 to 527.7 mm. Figure 6.11 presents the maximum distance between the consecutive samples for different number of sensors when sensor intervals varied between 525.9 to 527.7 mm. In Figure 6.11a, with 100 sensors the required samples can be collected to cover whole wheel circumference to the extend that the maximum distance between the consecutive samples reach to less that 5 mm. In Figure 6.11b that the wheel diameter is 99.01 mm, the required number of sensors is around 200 sensors. In Figure 6.11c, around 380 sensors are required to cover the whole wheel circumference with 5 mm maximum distance between the consecutive samples. As discussed in the section 4.3.5, the number of sensors required depends on the length of the effective zone of the sensors and can be reduced by increasing this length. As a result, 380 sensors are used collect samples from the wheels, and to generate a dataset from the reconstructed signals.

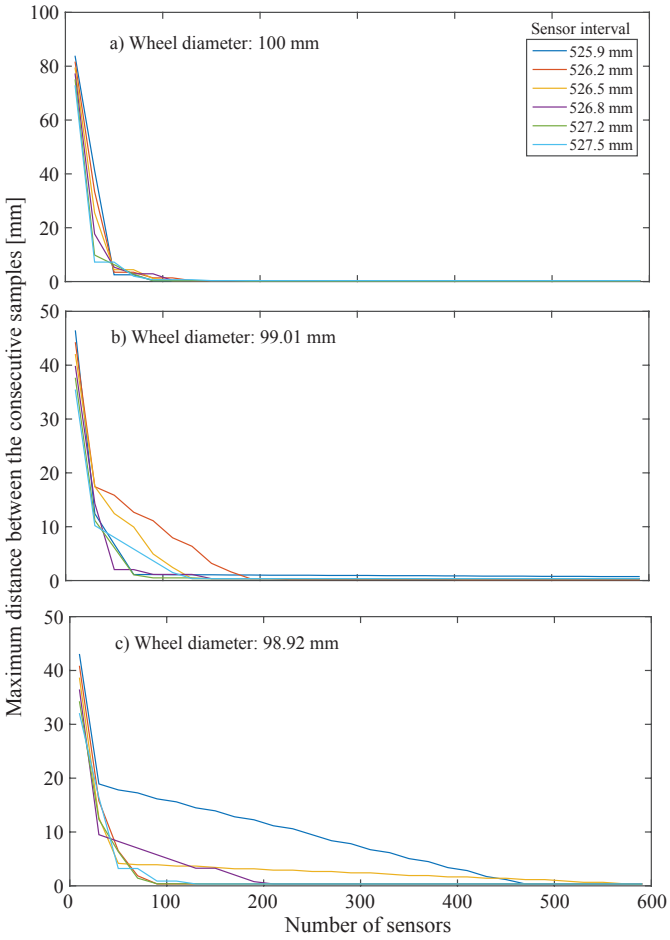

Figure 6.11: The maximum distance between the consecutive samples for different number of sensors and sensor intervals for the wheels with different diameters: a) 100 mm, b) 99.01 mm c) 98.92 mm.

Table 6.2: The definition and formula of different features used.

Name	**Formula**	**Size**
Peak Value	$\arg\max_k \psi_s$	1
Dynamic Value	$\arg\max_k \psi_s - \mu_s$	1
Ratio Value	$\frac{\arg\max_k \psi_s}{\mu_s}$	1
Main Signal	$\psi_s^*(k)$	K
Dynamic Signal	$\psi_s^*(k) - \mu_s$	K
Ratio Signal	$\frac{\psi_s^*(k)}{\mu_s}$	K
Normalized Signal	$\frac{\psi_s^*(k)-\mu_s}{\sigma_s}$	K
Fourier transform of Main Signal	$F(\psi_s^*(k))$	$K/2$
Fourier transform of Dynamic Signal	$F(\psi_s^*(k) - \mu_s)$	$K/2$
Fourier transform of Ratio Signal	$F(\frac{\psi_s^*(k)}{\mu_s})$	$K/2$
Fourier transform of Normalized Signal	$F(\frac{\psi_s^*(k)-\mu_s}{\sigma_s})$	$K/2$

Figure 6.12 presents the signals generated using 380 sensors by different wheels for different velocities and for 1.25 kN loads. This Figure shows 32 objects (signals) from 96 objects of the dataset. the other 64 objects generated by two other loads.

6.3.2. FEATURE EXTRACTION FROM RECONSTRUCTED SIGNALS

This Section follows the preprocessing, data alignment, and feature extraction procedure used in section 5.3. The reconstructed signals have been interpolated with 1 mm interval to give signals with uniform distribution of the samples over the circumferential coordinate. Then, the maximum of the signals is positioned in 100 mm to align the signals. Seven methods that used to represent the wheel condition are three statistical features include the peak value, dynamic value, and the ratio of the peak to the average, and four K-dimensional vectors include the reconstructed signal, dynamic signal, ratio signal, and the normalized signal. In addition to these methods, the frequency transform of these signals are used in this Chapter to represent the wheel condition. To transfer the signals into the frequency domain, the Fast Fourier transform is applied. Therefore, four other signals are generated by transferring the signals into the frequency domain. The amplitude of the transferred signals used as the feature required. Since the half of the transferred signals are used, the new signals have K/2 features. Table 6.2 presents the detailed definition and formula of different features.

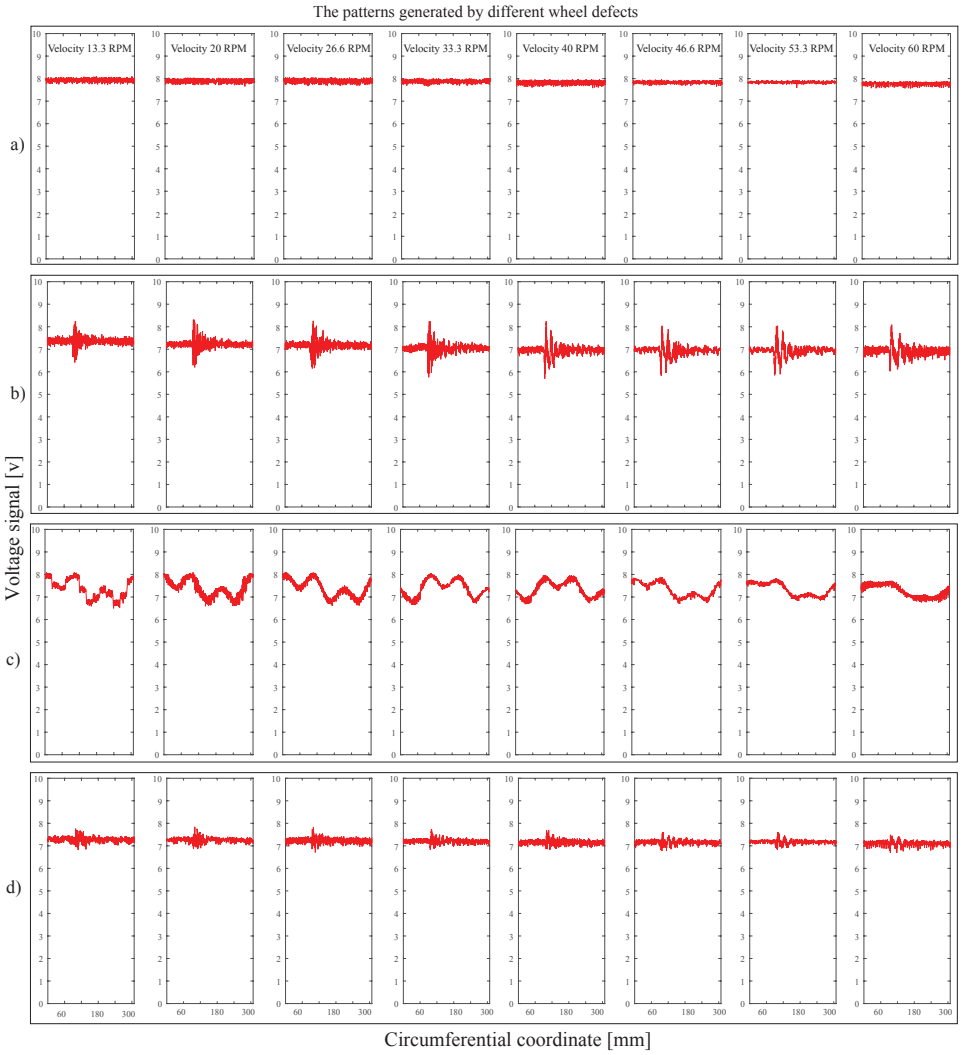

Figure 6.12: The main signals generated by a) the healthy wheel, b) the big flat with 6.6 mm length, c) the 3rd order periodic out-of-round wheel, and d) the small flat with 4.4 mm length for different velocities from 13.3-60 RPM, and for 1.25 kN loads.

6.4. WHEEL DEFECT IDENTIFICATION RESULTS

This Chapter made a dataset using the data generated by the test rig to train and test the classifiers used in Chapter 5. Three classifiers, SVM, 1-NN and 3-NN, are investigated using a 10-fold cross validation. To train the classifiers, the dataset is divided into 10 subsets. The classifiers are trained on nine subsets and are tested on the remaining subset. Since, the selection of the train set and test set is random, the process is repeated 20 times. Table 6.3 presents the average and the standard deviation of the errors after 20 repetitions for three classifiers and for 11 different feature extraction methods using the dataset generated by laboratory tests.

The results presented in Table 6.3 shows that the Frequency features provide much better performance. For example, 1-NN classifier using Fourier transform of reconstructed and dynamic signals classified the wheels with around 4% error. These results validates the wheel defect identification model.

In these tests four wheel with three different sizes have been used. Figure 6.11 showed that the maximum distances between the consecutive samples reduced to 5 mm for most sensor intervals by using around 50 sensors. This results indicates that the signals reconstructed by 50 sensors can provide useful information required. Therefore, the classification process is investigated by different datasets generated by different number of sensors. Figures 6.13, 6.14, and 6.15 present the variations of the classification errors by increasing the number of sensors used for collecting data and reconstructing the signals.

Figure 6.13 compares the classification errors of SVM, 1-NN, and 3-NN classifiers using the Peak value, dynamic value, and Ratio value when the number of sensor is increased. This Figure shows that the classification errors using 1-NN, and 3-NN classifiers decrease by increasing the number of sensors. In addition, the classification errors are too high when the number of sensors are too few. Figure 6.11 showed that with few number of sensors, the samples have large distance and could not cover the whole circumference. Therefore, using reasonable number of sensor or increasing the length of the effective zone to cover whole circumference is vital even when the reconstructed method is not used and only the statistical features are used.

Figure 6.14 shows that the 1-NN, and 3-NN classifiers using the main signal provided better performance than the dynamic signal, ratio signal, and the normalized signal. In addition, increasing the number of sensors more than around 30 sensors has no impact on the results. Figure 6.15 presents the results of the classifications using the frequency features. In Figures 6.15a, b, and c, the error reductions due to increasing the number of sensors are significant.

Table 6.3: A comparison between the results of different classifiers and feature methods by the average and the standard deviation of the classification errors. The horizontal bar represents the magnitude.

Feature	Classifier	Error [%]	Standard deviation of the error [%]
Peak value	SVM	75	0.33
	1-NN	48.33	1.03
	3-NN	39.42	1.66
Dynamic value	SVM	55.72	0.53
	1-NN	16.19	1.28
	3-NN	12.6	1.5
Ratio value	SVM	75	0
	1-NN	26.14	1.38
	3-NN	25.72	1.62
Main signal	SVM	26.04	2.48
	1-NN	16.77	1.34
	3-NN	18.43	0.96
Dynamic signal	SVM	34.94	2.09
	1-NN	47.6	0.68
	3-NN	48.38	0.71
Ratio signal	SVM	35.1	1.01
	1-NN	45	0.54
	3-NN	47.08	0.42
Normalized signal	SVM	28.59	2.47
	1-NN	33.64	1.12
	3-NN	34.47	1.58
Fourier transform of Main signal	SVM	14.06	1.73
	1-NN	4.06	0.46
	3-NN	6.3	0.92
Fourier transform of Dynamic signal	SVM	14.37	1.92
	1-NN	4.42	0.57
	3-NN	6.14	0.82
Fourier transform of Ratio signal	SVM	16.3	1.85
	1-NN	8.22	0.82
	3-NN	10.1	0.9
Fourier transform of Normalized signal	SVM	22.7	2.2
	1-NN	22.08	1.41
	3-NN	18.95	1.19

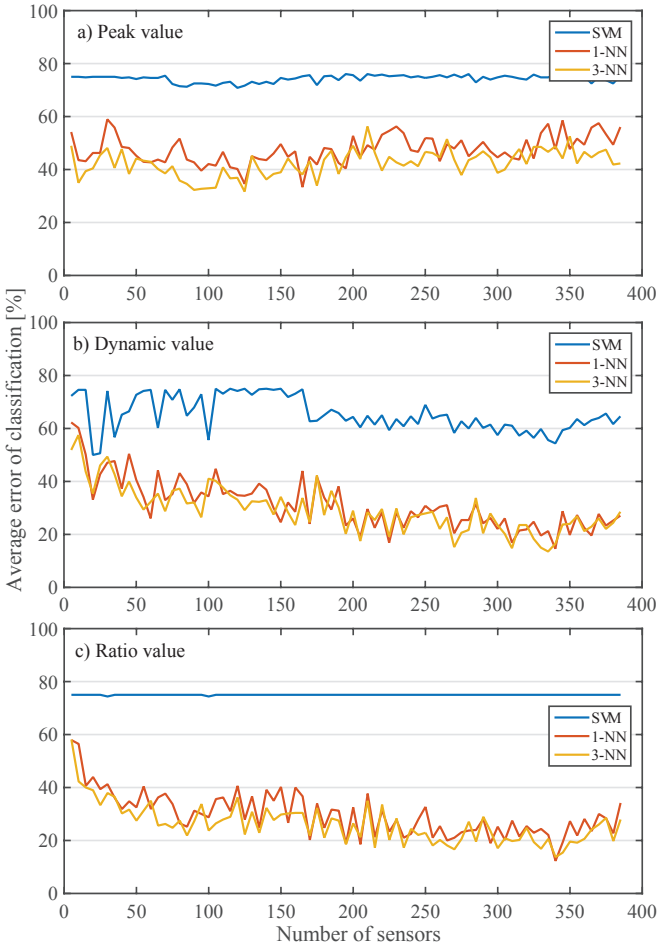

Figure 6.13: The comparison of the classification errors of 1-NN, and 3-NN classifiers by increasing the number of sensor for a) Peak value, b) dynamic value, and c) Ratio value.

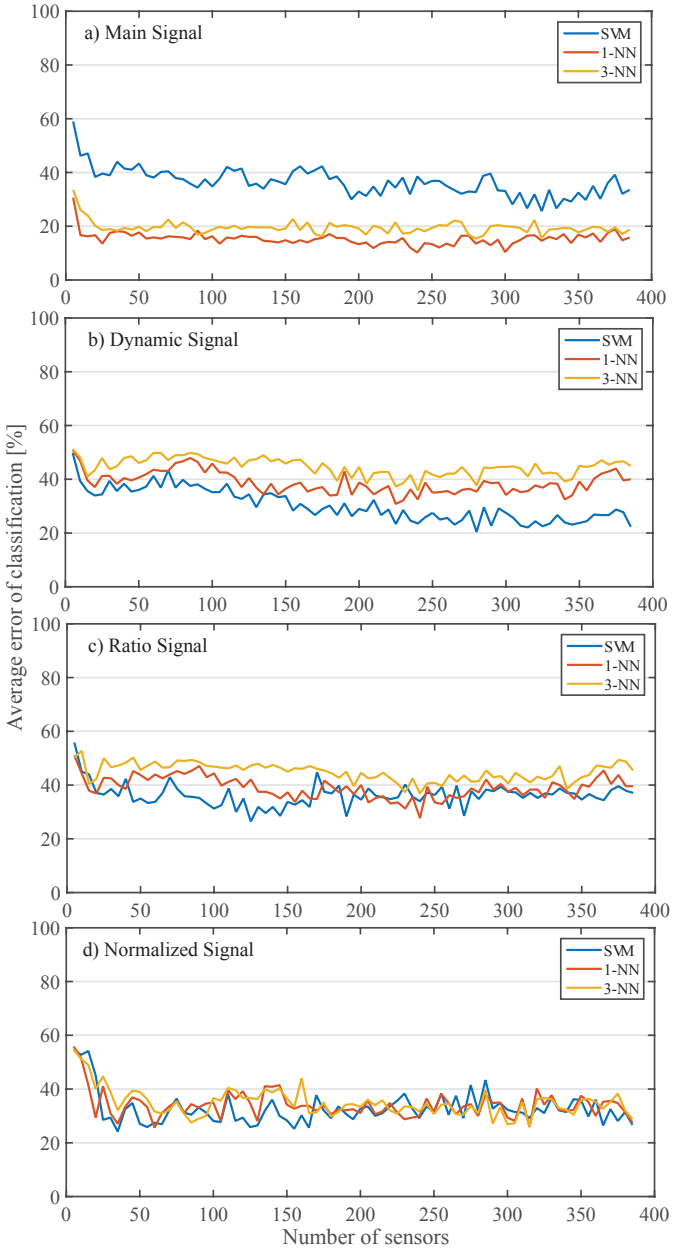

Figure 6.14: The comparison of the classification errors of 1-NN, and 3-NN classifiers by increasing the number of sensor for a) Peak value, b) dynamic value, and c) Ratio value.

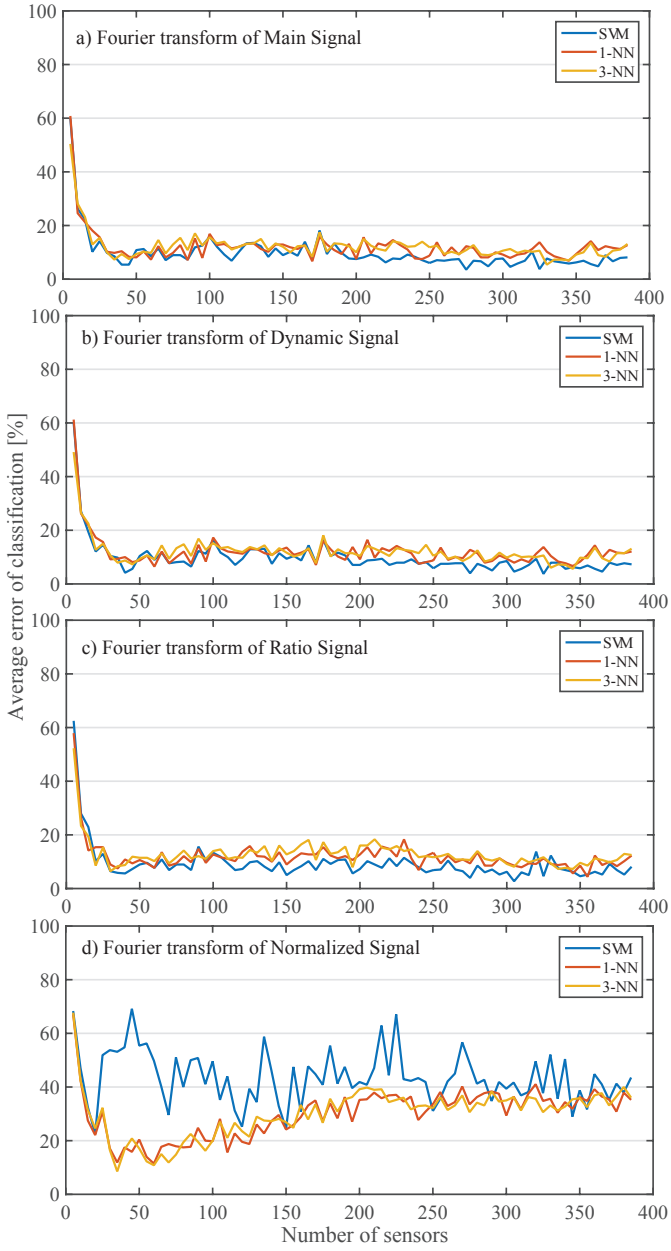

Figure 6.15: The comparison of the classification errors of 1-NN, and 3-NN classifiers by increasing the number of sensor for a) Peak value, b) dynamic value, and c) Ratio value.

6.5. CONCLUSION

This Chapter answered to the corresponding research question: "*How can the proposed method be tested and validated?*". This Chapter validated the data fusion, and the wheel defect identification models using the experimental data generated by a test rig. Four wheels with different conditions were tested by different loads and velocities to generate the required data. The data fusion model reconstruct signals from the collected samples and made a dataset. Pattern recognition methods were used to learn from the data to make classifiers. These classifiers were used to classify unseen data and validate the wheel defect identification model. The results obtained demonstrated the possibility of using the reconstructed signals to classify the wheels into different classes of defect types and severities.

Performance of the wheel defect identification model depends on two main parameters. First parameter is the classification method including preprocessing, feature extraction, and classifier used. The errors due to this parameter can be reduced by developing the preprocessing, and feature extraction procedures such as principal component analysis (PCA), and using classifiers with different specifications such as kernel function. The second parameter is the reconstructed signals used for training the classifiers. Chapter 4 investigated and discussed the influential parameters on the signals reconstructed. By considering these parameters, the errors of the defect identification model can be reduced.

7

CONCLUSIONS AND RECOMMENDATIONS

This dissertation proposed and investigated the performance of a data fusion method to reconstruct a new informative signal for estimating the wheel condition. This final Chapter draws the main conclusions in Section 7.1, and offers a set of recommendations for future research in Section 7.2.

7.1. CONCLUSIONS

This dissertation aimed to develop a wheel condition monitoring method to answer the following main research question: "*How can the extent of railway wheel defects be accurately estimated?*". To achieve this goal, Chapter 1 addressed five key research questions. This Section presents the answers of the key questions and summarizes their corresponding conclusions.

To present the state-of-the-art condition monitoring methods, Chapter 2 carried out a comprehensive literature study and answered the first key question: "*What are the state-of-the-art technologies for estimating the wheel condition?*". On-board and wayside are two methods for monitoring the wheel condition. On-board methods have several challenges to be implemented. Several wayside systems are commonly used to monitor the wheels. Since the wheel flat as a severe defect damage the track and train, many researches have been focused on detecting flats. These methods can be helpful for corrective maintenance by detecting the defective wheels. WILD is a commercial system invented few decades ago that is used for measuring the wheel load. WILD had no significant developments in the course of time. This system has great potential to be developed as a wheel condition monitoring system. The results obtained from different studies showed that the train velocity and axle load influence the WILD outputs. In addition, this system has difficulty in detecting minor defects and identifying the defect types. As a result, this research focused on developing the WILD system to estimate the wheel defect type and severity.

The sensor installed along the rail makes a partial observation of a moving wheel. Therefore, WILDs normally use multiple sensors to collect data from different portions of the wheels. The main idea that has been proposed and developed in this dissertation is combining the data collected by multiple sensors to reconstruct informative signals by mapping the samples over the circumferential coordinate in the space domain. Chapter 3 proposed a fusion method to answer the second key question: "*How can the data collected by multiple sensors mounted along the rail be fused to reconstruct a new informative signal?*". As we expected the reconstructed signal follows the contact force pattern that represents the wheel geometry. As a result, the proposed method can be considered as a generic method that can fuse different responses of track components such as rail and sleeper. As a proof, Chapter 4 used the rail to sleeper displacement signals, and Chapter 6 used the bending signals measured by strain sensors to reconstruct informative signals.

The output of the fusion process is influenced by several parameters. Chapter 4 carried out a detail parametric study to answer this question: "*How do the influential factors affect the reconstructed signal?*". The influential parameters can be categorized into two groups. The parameters influence the fusion process by making an imperfect reconstruction, and the parameters change the reconstructed signals by changing the wheel-rail contact force. Measurement noise is an example of the parameters of the first group that makes an imperfect measurement. When the defect is relatively small, the rail response variation due to the wheel defect is comparable with the measurement noise magnitude. Therefore, the measurement noise covers the defect signal in the reconstructed signal. Therefore, using sensors with high signal to noise ratio is essential for detecting the minor defects. Some other parameters influence the distribution of the samples over the circumferential coordinate such as sensor interval, wheel diameter, length of the effective zone, and number of sensors. These parameters should be determined in a way that the collected samples cover the whole wheel circumference. The most practical methods are increasing the number of sensors, and using the sensors with longer effective zones such as shear strain sensors presented in Figure 2.13. The parameters of the second group are the operational parameters such as the train velocity, and axle load that change the reconstructed signals. These parameters are out of control and have considerable effects on reconstructed signals.

Variations in the influential parameters such as train velocity, and axle load lead to variation in the signals reconstructed even when the defect is kept constant, and the fusion process works perfectly. In addition, some parameters such as measurement noise corrupt the signals reconstructed. The main purpose of this research is to estimate the wheel condition by identifying the defect type and severity. To attribute the reconstructed signals to specific class of defect type and severity, the pattern recognition methods have been exploited. To answer this question: "*How can the defect types and their severity be detected?*", Chapter 5 built a wheel defect identification model using Support Vector Machine (SVM), and k-nearest neighbour classifier (k-NN) to classify the signals into different classes. In this method, the classifiers are trained by a set of data to be able to classify new unseen data. Therefore, this method needs sufficient data from different classes of defect types and severities. The results obtained in Chapter 5 showed that the classification using the reconstructed signals gives convincing perfor-

mance with minor errors.

To validate the data fusion, and the wheel defect identification models a test rig has been designed and constructed in Chapter 6. To reconstruct signal, the data fusion model used the experimental data generated by the test rig. Then, the classifiers have been trained by the reconstructed signals to classify unseen data and to validate the wheel defect identification model. The results obtained validated the data fusion model by reconstructing informative signals. The wheel defect identification model as the main aim of this dissertation has been validated by classifying the wheels into different classes of defect types and severities using the classifiers trained by the reconstructed signals. The laboratory results showed that the extent of wheel defects be accurately estimated by classifying the wheels into different classes with less than 5% error. This means that the technology developed in this dissertation has a great potential for real field implementation.

7.2. RECOMMENDATIONS

Railway is a conservative, old, mostly government-owned, and complex industry. Each country has its own railway structure with different stakeholders. For example, in the Netherlands, ProRail is the infrastructure company and several train operators use the infrastructure, while in Switzerland, SBB is the infrastructure and operator company. To take the next step, some challenges regarding the technical development, and implementation should be tackled as follows:

- The available commercial WILDs in the market normally use 6 to 12 sensors per rail. These number of sensors are not enough to cover whole wheel circumference. Therefore, the first step is increasing the number of sensors to the extent that the collected samples provide required sampling frequency in the space domain to reconstruct the signals.
- To collect reliable data from the sensors, the measurement segments of the track should be maintained more than other segments. In addition, the sensors with higher signal to noise ratio such as FBG sensors can provide better outputs.
- The defect identification model exploited supervised pattern recognition methods that need a dataset to train the classifiers. In this dissertation, we considered limited classes of defects. To implement this model in practice, all possible defects with the corresponding range of severities should be considered to generate the required dataset for training the classifiers. As a result, a test campaign should be carried out to collect the required data.
- The defect identification model uses the reconstructed signals to train the classifiers. The reconstructed signals are the responses of the track to the contact force. Since the patterns of the reconstructed signals depend on the dynamic properties of track and vehicle, the training dataset should be localized by considering the variations in these properties.
- Following the dataset generation, the feature extraction methods should be tested and in case of poor performance, new features should be extracted.

- WILDs are being used to detect the detrimental wheels by measuring the high impact forces when they exceed a threshold. In this case, the WILDs are used as a safety and alarming system. When a wheel exceeds the threshold, it has to be stopped in the next station and the operator incurs a penalty. Therefore, the freight operators have to be conservative to be within the safety range. The outputs of the defect identification model can be used to avoid these consequences, and to maximize the train loads.

- The defect information can be used to optimize the maintenance plan of the wheels. Therefore, to monitor all wheels, the WILDs should be distributed over the network to give full coverage.

- The wheel-rail contact force (wheel condition), is required for the track degradation modelling and its lifetime prediction. The wheel condition estimated by the new method can be used to improve the track degradation model, lifetime prediction model, and the track maintenance plan.

- WILDs usually are used to calculate the track access charges by measuring the wheel load. The infrastructure company calculates the track access charges for train operators that use the infrastructure. These charges are normally calculated for each train based on the kilometres and loads. According to the Commission Implementing Regulation 909/2015 of the European Union [89], wheel defect such as flats can be taken into account for calculating the direct cost of trains. Therefore, the technology developed in this dissertation can be used for track access charge calculation by considering the wheel defect type and severity.

REFERENCES

[1] J C O Nielsen and A Johansson. Out-of-round railway wheels-a literature survey. *Proceedings of the Institution of Mechanical Engineers, Part F: Journal of Rail and Rapid Transit*, 214(2):79–91, jan 2000.

[2] See Yenn Chong, Jung-Ryul Lee, and Hye-Jin Shin. A review of health and operation monitoring technologies for trains. *Smart Structures and Systems*, 6(9):1079–1105, dec 2010.

[3] Tiedo Tinga. Application of physical failure models to enable usage and load based maintenance. *Reliability Engineering & System Safety*, 95(10):1061–1075, oct 2010.

[4] A Johansson and Jc O Nielsen. Out-of-round railway wheels—wheel—rail contact forces and track response derived from field tests and numerical simulations. *Proceedings of the Institution of Mechanical Engineers, Part F: Journal of Rail and Rapid Transit*, 217(2):135–146, jan 2003.

[5] Brant Stratman, Yongming Liu, and Sankaran Mahadevan. Structural health monitoring of railroad wheels using wheel impact load detectors. *Journal of Failure Analysis and Prevention*, 7(3):218–225, jul 2007.

[6] Maarten de Vries. *Just in time delivery of wheel sets*. Msc thesis, tel.7798, Master's Thesis, TEL.7798, Delft University of Technology, The Netherlands, 2013.

[7] I Vermeij, T Bontekoe, G Liefting, and J Peen. Optimisation of Rolling Stock Wheelset Life through Better Understanding of Wheel Tyre Degradation. *International Journal of Railway*, 1(3):83–88, 2008.

[8] Jing Lin, Matthias Asplund, and Aditya Parida. Reliability analysis for degradation of locomotive wheels using parametric Bayesian approach. *Quality and Reliability Engineering International*, 30(5):657–667, jul 2014.

[9] M Palo, H Schunnesson, U Kumar, P-O Larsson-Kråik, and D Galar. Rolling stock condition monitoring using wheel/rail forces. *Insight - Non-Destructive Testing and Condition Monitoring*, 54(8):451–455, aug 2012.

[10] Jasper Veldman, Hans Wortmann, and Warse Klingenberg. Typology of condition based maintenance. *Journal of Quality in Maintenance Engineering*, 17(2):183–202, may 2011.

[11] Vittorio Belotti, Francesco Crenna, Rinaldo C. Michelini, and Giovanni B. Rossi. Wheel-flat diagnostic tool via wavelet transform. *Mechanical Systems and Signal Processing*, 20(8):1953–1966, nov 2006.

[12] W Partington. Wheel impact load monitoring. *Proceedings of the ICE - Transport*, 100(4):243–245, jan 1993.

[13] B Brickle, R Morgan, E Smith, J Brosseau, and C Pinney. Identification of existing and new technologies for wheelset condition monitoring. Technical report, Rail Safety and Standards Board (RSSB), Report for the Rail Safety and Standards Board (RSSB). Report no. T607, 2008.

[14] M. Asplund, M. Palo, S. Famurewa, and M. Rantatalo. A study of railway wheel profile parameters used as indicators of an increased risk of wheel defects. *Proceedings of the Institution of Mechanical Engineers, Part F: Journal of Rail and Rapid Transit*, 230(2):323–334, feb 2016.

[15] Andrew K.S. Jardine, Daming Lin, and Dragan Banjevic. A review on machinery diagnostics and prognostics implementing condition-based maintenance. *Mechanical Systems and Signal Processing*, 20(7):1483–1510, oct 2006.

[16] DL Hall and James Llinas. An introduction to multisensor data fusion. *Proceedings of the IEEE*, 85(1):6–23, 1997.

[17] Alireza Alemi, Francesco Corman, and Gabriel Lodewijks. Condition monitoring approaches for the detection of railway wheel defects. *Proceedings of the Institution of Mechanical Engineers, Part F: Journal of Rail and Rapid Transit*, 231(8):961–981, sep 2017.

[18] C P Ward, P F Weston, E J C Stewart, H Li, R M Goodall, C Roberts, T X Mei, G Charles, and R Dixon. Condition monitoring opportunities using vehicle-based sensors. *Proceedings of the Institution of Mechanical Engineers, Part F: Journal of Rail and Rapid Transit*, 225(2):202–218, mar 2011.

[19] Jie ZHANG and Xue-song JIN. Influence of wheel polygonal wear on interior noise of high-speed trains. *Journal of Zhejiang University Science A*, 15(12):1002–1018, dec 2014.

[20] H.M. Tournay and J.M. Mulder. The transition from the wear to the stress regime. *Wear*, 191(1-2):107–112, jan 1996.

[21] B. Liang, S. D. Iwnicki, Y. Zhao, and D. Crosbee. Railway wheel-flat and rail surface defect modelling and analysis by time–frequency techniques. *Vehicle System Dynamics*, 51(9):1403–1421, sep 2013.

[22] B. Liang, S. Iwnicki, A. Ball, and A.E. Young. Adaptive noise cancelling and time–frequency techniques for rail surface defect detection. *Mechanical Systems and Signal Processing*, 54-55:41–51, mar 2015.

[23] S. Jia and M. Dhanasekar. Detection of rail wheel flats using wavelet approaches. *Structural Health Monitoring*, 6(2):121–131, jun 2007.

[24] Yifan Li, Jianxin Liu, and Yan Wang. Railway Wheel Flat Detection Based on Improved Empirical Mode Decomposition. *Shock and Vibration*, 2016:1–14, 2016.

[25] Yifan Li, Ming J Zuo, Jianhui Lin, and Jianxin Liu. Fault detection method for railway wheel flat using an adaptive multiscale morphological filter. *Mechanical Systems and Signal Processing*, 84:642–658, feb 2017.

[26] R. S. Dwyer-Joyce, C. Yao, R. Lewis, and H. Brunskill. An ultrasonic sensor for monitoring wheel flange/rail gauge corner contact. *Proceedings of the Institution of Mechanical Engineers, Part F: Journal of Rail and Rapid Transit*, 227(2):188–195, mar 2013.

[27] B. Frankenstein, D. Hentschel, E. Pridoehl, and F. Schubert. Hollow shaft integrated health monitoring system for railroad wheels. In Norbert Meyendorf, George Y. Baaklini, and Bernd Michel, editors, *Proceedings of SPIE - The International Society for Optical Engineering*, page 46, San Diego, CA | March 06, 2005, may 2005.

[28] Akira Matsumoto, Yasuhiro Sato, Hiroyuki Ohno, Masao Tomeoka, Kosuke Mat-

sumoto, Jun Kurihara, Tomohisa Ogino, Masuhisa Tanimoto, Yasushi Kishimoto, Yoshi Sato, and Takuji Nakai. A new measuring method of wheel–rail contact forces and related considerations. *Wear*, 265(9-10):1518–1525, oct 2008.

[29] Akira Matsumoto, Yasuhiro Sato, Hiroyuki Ohno, Makoto Shimizu, Jun Kurihara, Takuya Saitou, Yohei Michitsuji, Ryo Matsui, Masuhisa Tanimoto, and Masa-aki Mizuno. Actual states of wheel/rail contact forces and friction on sharp curves – Continuous monitoring from in-service trains and numerical simulations. *Wear*, 314(1-2):189–197, jun 2014.

[30] H J Salzburger, M Schuppmann, Wang Li, and Gao Xiaorong. In-motion ultrasonic testing of the tread of high-speed railway wheels using the inspection system AUROPA III. *Insight - Non-Destructive Testing and Condition Monitoring*, 51(7):370–372, jul 2009.

[31] Jose Brizuela, Alberto Ibanez, Patricia Nevado, and Carlos Fritsch. Railway wheels flat detector using Doppler effect. *Physics Procedia*, 3(1):811–817, jan 2010.

[32] J. Brizuela, C. Fritsch, and A. Ibanez. Railway wheel-flat detection and measurement by ultrasound. *Transportation Research Part C: Emerging Technologies*, 19(6):975–984, dec 2011.

[33] S Kenderian, B B Djordjevic, D Cerniglia, and G Garcia. Dynamic railroad inspection using the laser-air hybrid ultrasonic technique. *Insight - Non-Destructive Testing and Condition Monitoring*, 48(6):336–341, jun 2006.

[34] N.a. Thakkar, John a. Steel, R.L. Reuben, G. Knabe, D. Dixon, and R.L. Shanks. Monitoring of Rail-Wheel Interaction Using Acoustic Emission (AE). *Advanced Materials Research*, 13-14:161–168, 2006.

[35] N. a. Thakkar, J. a. Steel, and R. L. Reuben. Rail-wheel contact stress assessment using acoustic emission: a laboratory study of the effects of wheel flats. *Proceedings of the Institution of Mechanical Engineers, Part F: Journal of Rail and Rapid Transit*, 226(1):3–13, jan 2012.

[36] K. Bollas, D. Papasalouros, D. Kourousis, and A. Anastasopoulos. Acoustic emission monitoring of wheel sets on moving trains. *Construction and Building Materials*, 48:1266–1272, nov 2013.

[37] Kai Yang, Li Ma, Xiaorong Gao, and Li Wang. Profile parameters of wheelset detection for high speed freight train. In Mohamed Othman, Sukumar Senthilkumar, and Xie Yi, editors, *Fourth International Conference on Digital Image Processing*, volume 8334, pages 83341W–83341W–6, Kuala Lumpur, Malaysia | April 7, 2012, may 2012.

[38] A Bracciali and G Cascini. Detection of corrugation and wheelflats of railway wheels using energy and cepstrum analysis of rail acceleration. *Proceedings of the Institution of Mechanical Engineers, Part F: Journal of Rail and Rapid Transit*, 211(2):109–116, mar 1997.

[39] Dimitris Skarlatos, Kleomenis Karakasis, and Athanassios Trochidis. Railway wheel fault diagnosis using a fuzzy-logic method. *Applied Acoustics*, 65(10):951–966, oct 2004.

[40] M. L. Lee and W. K. Chiu. Determination of railway vertical wheel impact magnitudes: field trials. *Structural Health Monitoring*, 6(1):49–65, mar 2007.

[41] M. Palo, D. Galar, T. Nordmark, M. Asplund, and D. Larsson. Condition monitoring

at the wheel/rail interface for decision-making support. *Proceedings of the Institution of Mechanical Engineers, Part F: Journal of Rail and Rapid Transit*, 228(6):705–715, aug 2014.

[42] C. C. Lai, Jacob C. P. Kam, David C. C. Leung, Tony K. Y. Lee, Aiken Y. M. Tam, S. L. Ho, H. Y. Tam, and Michael S. Y. Liu. Development of a Fiber-Optic Sensing System for Train Vibration and Train Weight Measurements in Hong Kong. *Journal of Sensors*, 2012:1–7, 2012.

[43] Chuliang Wei, Qin Xin, W. H. Chung, Shun-yee Liu, Hwa-yaw Tam, and S. L. Ho. Real-time train wheel condition monitoring by Fiber Bragg Grating sensors. *International Journal of Distributed Sensor Networks*, 2012:1–7, 2012.

[44] H. Y. Tam, S. Y. Liu, B. O. Guan, W. H. Chung, T. H. Chan, and L. K. Cheng. Fiber Bragg Grating sensors for structural and railway applications. In Yun-Jiang Rao, Osuk Y. Kwon, and Gang-Ding Peng, editors, *Proceedings of SPIE - The International Society for Optical Engineering*, volume 5634, pages 85–97, Beijing, China | November 8, 2004, feb 2005.

[45] KY Lee, KK Lee, and SL Ho. Exploration of using FBG sensor for derailment detector. *WSEAS Transactions Topics Systems*, 3(6):2433–2439, 2004.

[46] Chu-liang Wei, Chun-cheung Lai, Shun-yee Liu, W H Chung, T K Ho, Hwa-yaw Tam, S L Ho, A McCusker, J Kam, and K Y Lee. A Fiber Bragg Grating sensor system for train axle counting. *IEEE Sensors Journal*, 10(12):1905–1912, dec 2010.

[47] Massimo Leonardo Filograno, P. Corredera Guillen, A. Rodriguez-Barrios, S. Martin-Lopez, M. Rodriguez-Plaza, Alvaro Andres-Alguacil, and M. Gonzalez-Herraez. Real-Time Monitoring of Railway Traffic Using Fiber Bragg Grating Sensors. *IEEE Sensors Journal*, 12(1):85–92, jan 2012.

[48] Massimo Leonardo Filograno, Pedro Corredera, Miguel Rodriguez-Plaza, Alvaro Andres-Alguacil, and Miguel Gonzalez-Herraez. Wheel Flat Detection in High-Speed Railway Systems Using Fiber Bragg Gratings. *IEEE Sensors Journal*, 13(12):4808–4816, dec 2013.

[49] Jianjun Pan, Weilai Li, and Xin Dai. Train overload and unbalanced load detection based on FBG gauge. In Minghong Yang, Dongning Wang, and Yun-Jiang Rao, editors, *Proceedings of SPIE - The International Society for Optical Engineering*, volume 8924, page 89242D, Wuhan, China | October 15, 2013, oct 2013.

[50] S.L. Ho, K.K. Lee, K.Y. Lee, H.Y. Tam, W.H. Chung, S.Y. Liu, C.M. Yip, and T.K. Ho. A comprehensive condition monitoring of modern railway. In *IET International Conference on Railway Condition Monitoring*, volume 2006, pages 125–129, Birmingham,. IEE.

[51] Ying Song, Yan Liang Du, and Bao Chen Sun. Study on wheel/rail interaction force real-time monitoring method based on piezoelectric sensing technology. *Advanced Materials Research*, 79-82:7–10, aug 2009.

[52] S Iwnicki. *Handbook of Railway Vehicle Dynamics*. CRC Press, may 2006.

[53] Alireza Alemi, Francesco Corman, Yusong Pang, and Gabriel Lodewijks. Reconstruction of an informative railway wheel defect signal from wheel–rail contact signals measured by multiple wayside sensors. *Proceedings of the Institution of Mechanical Engineers, Part F: Journal of Rail and Rapid Transit*, page

095440971878436, jul 2018.

[54] P.C. Dings and M.G. Dittrich. ROUGHNESS ON DUTCH RAILWAY WHEELS AND RAILS. *Journal of Sound and Vibration*, 193(1):103–112, may 1996.

[55] K J Sawley. Calculation of temperatures in a sliding wheel/rail system and implications for wheel steel development. *Proceedings of the Institution of Mechanical Engineers, Part F: Journal of Rail and Rapid Transit*, 221(4):455–464, jan 2007.

[56] U Olofsson and K Sundvall. Influence of leaf, humidity and applied lubrication on friction in the wheel-rail contact: Pin-on-disc experiments. *Proceedings of the Institution of Mechanical Engineers, Part F: Journal of Rail and Rapid Transit*, 218(3):235–242, may 2004.

[57] J. Piotrowski and H. Chollet. Wheel–rail contact models for vehicle system dynamics including multi-point contact. *Vehicle System Dynamics*, 43(6-7):455–483, jun 2005.

[58] M Fermer and J Nielsen. Wheel/Rail Contact Forces for Flexible versus Solid Wheels due to Tread Irregularities. *Vehicle System Dynamics*, 23(sup1):142–157, jan 1994.

[59] M Fermer and J C O Nielsen. Vertical Interaction between Train and Track with Soft and Stiff Railpads—Full-Scale Experiments and Theory. *Proceedings of the Institution of Mechanical Engineers, Part F: Journal of Rail and Rapid Transit*, 209(1):39–47, jan 1995.

[60] J. Nielsen. Out-of-round railway wheels. In *Wheel–Rail Interface Handbook*, pages 245–279. Elsevier, 2009.

[61] A.J. Jerri. The Shannon sampling theorem - Its various extensions and applications: A tutorial review. *Proceedings of the IEEE*, 65(11):1565–1596, 1977.

[62] C. Knapp and G. Carter. The generalized correlation method for estimation of time delay. *IEEE Transactions on Acoustics, Speech, and Signal Processing*, 24(4):320–327, aug 1976.

[63] UIC Leaflet. UIC 510-2 OR, Trailing Stock: Wheel and Wheel Sets Conditions Concerning the use of Wheels of Various Diameters. Technical Report May, 2004.

[64] A Alemi, F Corman, and G Lodewijks. Monitoring of Railway Wheel Diameters by means of a Wheel Impact Load Detector. In *Proceedings of the Third International Conference on Railway Technology: Research, Development and Maintenance*, pages 1–19, Cagliari, 2016.

[65] D W Barke and W K Chiu. A Review of the Effects of Out-Of-Round Wheels on Track and Vehicle Components. *Proceedings of the Institution of Mechanical Engineers, Part F: Journal of Rail and Rapid Transit*, 219(3):151–175, jun 2005.

[66] C.J.M. van Ruiten. A new method for the measurement of wheel/rail roughness. *Journal of Sound and Vibration*, 120(2):287–295, jan 1988.

[67] S G Newton and R A Clark. An investigation into the dynamic effects on the track of wheelflats on railway vehicles. *ARCHIVE: Journal of Mechanical Engineering Science 1959-1982 (vols 1-23)*, 21(4):287–297, jun 1979.

[68] A. Pieringer, W. Kropp, and J.C.O. Nielsen. The influence of contact modelling on simulated wheel/rail interaction due to wheel flats. *Wear*, 314(1-2):273–281, jun 2014.

[69] Johan Ahlström and Birger Karlsson. Microstructural evaluation and interpretation

of the mechanically and thermally affected zone under railway wheel flats. *Wear*, 232(1):1–14, sep 1999.

[70] D.H. Stone, S.F. Kalay, and A. Tajaddini. Statistical Behaviour of Wheel Impact Load Detectors to Various Wheel Defects. In *International Wheelset Congress*, number August 1991, pages 9–13, Sydney, N.S.W, 1992.

[71] Rolling Stock and Wheel Defect. CRN RS 011 Roling stock wheel defect limits - Engineering Standard. Technical report, 2012.

[72] Sergey M. Zakharov and Irina G. Goryacheva. Rolling contact fatigue defects in freight car wheels. *Wear*, 258(7-8):1142–1147, mar 2005.

[73] G.J. Moyar and D.H. Stone. An analysis of the thermal contributions to railway wheel shelling. *Wear*, 144(1-2):117–138, apr 1991.

[74] Jongwoo Jun, Myoungki Choi, Jinyi Lee, Jungwon Seo, and Kisu Shin. Nondestructive testing of express train wheel using the linearly integrated Hall sensors array on a curved surface. *NDT & E International*, 44(5):449–455, sep 2011.

[75] P.J. Mutton, C.J. Epp, and J. Dudek. Rolling contact fatigue in railway wheels under high axle loads. *Wear*, 144(1-2):139–152, apr 1991.

[76] Mauro Cavalletti. Personal interview, Wheel defect modelling, VI-GRADE Support, 2016.

[77] Simon Iwnicki. Manchester Benchmarks for Rail Vehicle Simulation. *Vehicle System Dynamics*, 30(3-4):295–313, sep 1998.

[78] VI-grade engineering software & services. VI-Rail 16.0 Documentation. Technical report, 2014.

[79] HY Tam, T Lee, SL Ho, and T Haber. Utilization of fiber optic Bragg Grating sensing systems for health monitoring in railway applications. *Structural Health Monitoring*, 2:1824–1831, 2007.

[80] Alireza Alemi, Yusong Pang, Francesco Corman, and Gabriel Lodewijks. Railway Wheel Defect Identification Using the Signals Reconstructed from Impact Load Data. In Fu-Kuo Chang and Fotis Kopsaftopoulos, editors, *11th International Workshop on Structural Health Monitoring*, pages 1511–1518, Stanford, 2017.

[81] Alireza Alemi, Yusong Pang, and Gabriel Lodewijks. In-Service Detection of Defective Railway Wheels with Periodic out-of-Roundness. In *11th International Conference on Contact Mechanics and Wear of Rail/Wheel Systems*, pages 11–12, 2018.

[82] Sergios Theodoridis and Konstantinos Koutroumbas. *Pattern Recognition (Fourth Edition)*. Elsevier, 4th edition, sep 2009.

[83] Corinna Cortes and Vladimir Vapnik. Support-vector networks. *Machine Learning*, 20(3):273–297, sep 1995.

[84] T. Cover and P. Hart. Nearest neighbor pattern classification. *IEEE Transactions on Information Theory*, 13(1):21–27, jan 1967.

[85] Alireza Alemi, Yusong Pang, and Gabriel Lodewijks. Experimental Validation of Multi-Sensor Data Fusion Model for Railway Wheel Defect Identification. In *4th European Conference of the Prognostics and Health Management Society*, pages 2–7, 2018.

[86] T D Armstrong and D J Thompson. Use of a reduced scale model for the study of wheel/rail interaction. *Proceedings of the Institution of Mechanical Engineers, Part*

F: Journal of Rail and Rapid Transit, 220(3):235–246, 2006.

[87] N. a. Thakkar, J. a. Steel, and R. L. Reuben. A laboratory study of rail-wheel interaction monitoring using acoustic emission: Effect of rolling conditions with and without lateral rattling. *Proceedings of the Institution of Mechanical Engineers, Part F: Journal of Rail and Rapid Transit*, 227(2):161–175, sep 2012.

[88] Meysam Naeimi, Zili Li, Roumen H. Petrov, Jilt Sietsma, and Rolf Dollevoet. Development of a New Downscale Setup for Wheel-Rail Contact Experiments under Impact Loading Conditions. *Experimental Techniques*, 42(1):1–17, feb 2018.

[89] European Commission. Commission Implementing Regulation (EU) 2015/909. *Official Journal of the European Union*, 2015(June):17–22, 2015.

GLOSSARY

List of symbols and notations

The following Table presents a list of the symbols and notations used in this Dissertation.

a_t	acceleration in the time domain
A_ω	acceleration in the frequency domain
b_G	width of the section in rail neutral line
C_I	condition index
C_f	filter coefficient
C	number of filter coefficients
e_{max}	maximum of strain signal
e_{min}	minimum of strain signal
f_t	sensor sampling frequency in the time domain
f_s	sensor sampling frequency in the space domain
f_{max}	highest frequency contained in signal
f_{U_d}	shifted frequency
f_U	frequency of signal propagated
F_t	force in the time domain
F_ω	force in the frequency domain
F_{max}	maximum force
$\bar{F}$	average force
F_D	dynamic force
F_{w_r}	vertical force of the right wheel
F_{w_l}	vertical force of the left wheel
F_{w_1}	vertical force of the first wheel
F_{w_2}	vertical force of the second wheel
F_{xz}	vertical force calculated by shear strain
F_1	first feature
F_2	second feature
G	tangential elasticity module
$g(t)$	wheel defect signal in the time domain
$g_j(t)$	windowed defect signal measured by sensor in the time domain

$g(x)$	wheel defect signal in the space domain
$g_j(x)$	windowed defect signal measured by sensor in the space domain
$g(i)$	dimensionless wheel defect signal
$g_j(i)$	dimensionless windowed defect signal measured by sensor
h_t	system response in the time domain
H_ω	system response in the frequency domain
I_y	inertial momentum of the rail section
I	total number of samples of the signal
k_c	calibration coefficient
L_w	wheel circumference length
L_e	length of the effective zone
M	total number of sensors
N	total number of samples in the effective zone of the sensors
N^t	total number of samples from defective area
N^s	number of defective area samples that mapped in the sequential order
n_e	refractive index of the core of FBG sensor
$n_j(t)$	uncorrelated noise in the time domain
$n_j(x)$	uncorrelated noise in the space domain
$n_j(i)$	dimensionless uncorrelated noise
P_i	sensor position
R_w	wheel radius
R_F	force ratio
R_l	off-loading ratio
$r_{k,c}$	ratio of the number of defective area samples that mapped in the sequential order to the total number of the defective area samples
$R_{z_1 z_2}(\gamma)$	cross-correlation between the signals measured by two sensors
$R_{\hat{\psi}_r^*,\hat{\psi}_s^*}$	cross-correlation between interpolated normalized reconstructed and reference signals
$R_{\hat{\psi}_r^*,\hat{\psi}_r^*}$	auto-correlation of the interpolated normalized reference signal
S_y	static momentum of the lower part of rail
$S_{m,n}$	dataset from the collected samples
$S^1_{m,n}$	samples from the defective area
$S^2_{m,n}$	samples from the healthy area
$\tilde{S}_{\psi_r,\psi_s}$	similarity between the reference signal and the reconstructed signal
T	measurement time
T_L	lower threshold
T_U	upper threshold
V_U	velocity of the ultrasonic wave
V	train velocity

$w(t)$	wheel signal in the time domain
$w(x)$	wheel signal in the space domain
$w(i)$	dimensionless wheel signal
X_m	space position of the sensors
Y_m	position of the sensors over the circumferential coordinate
$z_j(t)$	signal measured by sensor in the time domain
$z_j(x)$	signal measured by sensor in the space domain
$z_j(i)$	dimensionless signal measured by sensor
$Z_{m,i}$	dataset of all signals measured by all sensors
α_c	scaling factor
γ	lag in the cross-correlation function
δ	sample delay between signals
$\Delta\lambda_B$	alteration of reflected wavelength
ε	strain
$\bar{\varepsilon}$	average of strain changes
ε_{xz}	shear strain
Λ	grating period of FBG sensor
λ_{max}	maximum distance between the consecutive samples
λ_B	reflected back wavelength
μ_s	average of the samples
μ_r	average of the reference signal
μ_s	average of the reconstructed signal
ρ	space delay between signals
σ_s	standard deviation of the samples
σ_s	standard deviation of the reconstructed signal
σ_r	standard deviation of the reference signal
τ	time delay between signals
ψ_s	reconstructed signal
ψ_r	reference signal
$\hat{\psi}_r$	normalized reference signal
$\hat{\psi}_s$	normalized reconstructed signal
$\hat{\psi}_r^*$	interpolated normalized reference signal
$\hat{\psi}_s^*$	interpolated normalized reconstructed signal
ω	angular velocity
$\lfloor \rfloor$	round operator toward the nearest integer less than or equal to the element

List of abbreviations

The following Table presents a list of abbreviations used in this Dissertation.

CMS	Condition Monitoring System
WILD	Wheel Impact Load Detectors
RCF	Rolling Contact Fatigue
RMS	Root Mean Square
EMD	Empirical Mode Decomposition
EEMD	Ensemble Empirical Mode Decomposition
AMMF	Adaptive Multiscale Morphological Filtering
FBG	Fibre Bragg Grating
SNR	Signal to Noise Ratio
SSM	Single Sampling Method
MSM	Multiple Sampling Method
OOR	Periodic Out Of Roundness
FFT	Fast Fourier transform
SVM	Support Vector Classifier
kNN	k-Nearest Neighbour classifier
PCA	Principal Component Analysis

ACKNOWLEDGEMENTS

Here, I would like to express my gratitude to all people fully supported me since when I was thinking to carry out PhD to the defence ceremony. In 2008, when I started working in Iran Nanotechnology Initiative Council, I was in Public Awareness Department responsible for nano technology news. In the early days, I heard a news about the achievement of an Iranian PhD researcher in Delft University of Technology that created my first impression to find more about TU Delft. Later, when I decided to apply for PhD positions in abroad, I chose TU Delft.

I am deeply grateful to ministry of science, research and technology, I.R. Iran for providing me with the scholarship to work on this PhD research. I owe a very important debt to people backing me during the period that the imposition of unfair sanctions made enormous difficulty.

I would like to show my greatest appreciation to my promoter Gabriel Lodewijks for providing me the opportunity to join his research group, Transport Engineering and Logistics. He offered me very practical guidance. I have had the support and encouragement of Gabriel specially for building the test rig and carrying out the laboratory tests.

I would like to offer my special thanks to my co-promotors Francesco Corman, and Yusong Pang. I was always eager to receive Francesco's critical comments on my papers. The weekly meetings with Francesco were sufficiently challenging for making my thoughts coherent. He has been greatly tolerant and supportive. After Francesco left TU Delft in September 2016, I missed a great supervisor. Hopefully, Yusong perfectly filled that huge gap. I received generous support from Yusong in the most difficult phase of my research, the course of the laboratory experiments.

Jilt Sietsma gave me constructive comments and warm encouragement. As my mentor, he always asked beyond my research about my life and family. I would also like to express my gratitude to Davood Younesian as my Iranian supervisor for his support and suggestions. I would like to express my gratitude to my PhD defence committee members, who read my thesis and improved that by their insightful comments and suggestions. Special thanks to Jens Nielsen, Shaohua Dong, Rinze Benedictus, and Rolf Dollevoet.

I am particularly grateful for the assistance given by Perry Posthoorn, and Steve van Herk from DEMO for designing and manufacturing the test rig, right on schedule with effective collaboration. I would particularly like to thank Ed Stok and Freek Brakel for their loyal technical support, from ordering the sensors and accessories, to installing the sensors, providing the space in the lab, setting the tools, and all other requirements to conduct the experiments.

I have greatly benefited from David tax during the pattern recognition course and later by giving insightful comments and suggestions on my paper. Advice and comments given by Sundeep Chepuri has been a great help in signal processing. Special thanks to

Chen Shen for detailed guidance about installing and using VI-Rail. I thank Zili li for permission to use the VI-Rail licence to run the simulation experiment.

Within Maritime and Transport Technology Department, thanks to my office-mate, Huarong Zheng, Fan Feng, Wenjing Guo, and Ioana Georgescu. It is a pleasure to thank Dineke, Patty, Monique, Anouk, Pauline, and Jozephina for their support. I am deeply grateful to Johan Los for translating the English summary of my thesis into Dutch and to Marc Fransen for revising that. Special thanks to my colleague and friend, Sayed Ebrahim, who helped me a lot when I arrived the Netherlands. My deepest appreciation goes to all MTT staffs who I cannot mention them altogether here.

I want to thank my TU Delft colleagues who arranged the events and offered me the opportunity to give a talk and receive constructive feedbacks. Thanks to Zhen Yang for Railway Colloquium in CiTG Faculty, Seyran Khademi for Signal Processing Seminar in EWI Faculty, and Xiangwei Liu for Maritime and Transport Technology PhD Event in 3mE Faculty.

Special thanks to John van Haare from Valorisation Centre and Dap Hartmann from Delft Center of Entrepreneurship for recommending my patented technology as a relevant case to students for study in the Masterclass Turning Your Thesis into Business. I have found my co-founder, Nicola Croce, in that class. I am deeply grateful to Robert Jan van Vugt, Ruben Kranendonk, and Rutger Schouten for Validation Program in YesDelft incubator.

This thesis would not have been possible without persistent help and great encouragement of my friends and family. I want to thank the Iranian community in the Netherlands, specially our weekly gathering, Jalaseh Quran, and Hey'at Mohebban Al-Mahdi. I am indebt to my parent for their spiritual support, Maman Sedigheh and Baba Abolfazl, who pray for me every day. I would like to thank my wife's family, particularly her parent, Maman Razieh and Baba Morteza, who their emotional support for my wife was the key solution for dealing with the sense of loneliness. I would also like to express my gratitude for the assistance given by them, before, during, and after my second child, Mohammad Amin, was born.

I owe my deepest gratitude to my lovely wife, Madiheh, who is my best friend. She embraced moving with me to the other continent with a 2 years old child, leaving her family and friends and experiencing loneliness, delay in her education, and challenge of living with a PhD researcher with intolerable pressure, excessive stress, and continuing uncertainty. She spent most of her time to train our two children, Salman, and Mohammad Amin. My deepest heartfelt appreciation goes to Dear Madiheh.

Alireza Alemi
Delft, December 2018

LIST OF PUBLICATIONS

JOURNAL PAPERS

1. **A. Alemi**, F. Corman, and G. Lodewijks, "Condition monitoring approaches for the detection of railway wheel defects", Proc. Inst. Mech. Eng. Part F J. Rail Rapid Transit. **Review paper**, 2017, vol 231, Page 961–981. (Editor's Choice paper for September 2017- One of the top 10 most downloaded papers of the Journal in 2017.)

2. **A. Alemi**, F. Corman, Y. Pang, and G. Lodewijks, "Reconstruction of an informative railway wheel defect signal from wheel–rail contact signals measured by multiple wayside sensors," Proc. Inst. Mech. Eng. Part F J. Rail Rapid Transit, vol. 233, no. 1, pp. 49–62, 2019. (SAGE Choice to be open access)

3. **A. Alemi**, F. Corman, Y. Pang, and G. Lodewijks, "Evaluation of influential parameters contributing to reconstruction of railway wheel defect signal," under review in Proc. Inst. Mech. Eng. Part F J. Rail Rapid Transit, 2019.

4. **A. Alemi**, Y. Pang, F. Corman, and G. Lodewijks, "Laboratory validation of in-service railway wheel defect identification using the defect signal reconstructed by the multi-sensor data fusion model," under review in Journal of Mechanical Systems and Signal Processing, 2019.

CONFERENCE PROCEEDINGS

1. **A. Alemi**, Y. Pang, and G. Lodewijks, "In-Service Detection of Defective Railway Wheels with Periodic Out-Of-Roundness," in 11th International Conference on Contact Mechanics and Wear of Rail/Wheel Systems, 2018, Delft, The Netherlands.

2. **A. Alemi**, Y. Pang, and G. Lodewijks, "Experimental Validation of Multi-Sensor Data Fusion Model for Railway Wheel Defect Identification," in 4th European conference of the prognostics and health management society, 2018, Utrecht, The Netherlands.

3. **A. Alemi**, Y. Pang, F. Corman, and G. Lodewijks, "Railway Wheel Defect Identification Using the Signals Reconstructed from Impact Load Data," in 11th International Workshop on Structural Health Monitoring, 2017, Stanford University, The United States.

4. **A. Alemi**, F. Corman, and G. Lodewijks, "Monitoring of Railway Wheel Diameters by means of a Wheel Impact Load Detector," in Proceedings of the Third International Conference on Railway Technology: Research, Development and Maintenance, 2016, pp. 1–19, Cagliari, Italy.

5. **A. Alemi**, F. Corman, G. Lodewijks, "Maintenance planning of multiple wheels of rolling stock based on intelligent condition monitoring system" TRAIL Congress 2014, Delft, The Netherlands.

PATENTS AND PATENT APPLICATIONS

1. **Alireza Alemi**, "Wheel Condition Monitoring", US PATENT /62/512,081, PCT /IB2018 /053558, 2017.

ABOUT THE AUTHOR

Alireza Alemi was born on 1985 in Damghan, Iran. In 2008, he obtained his BSc degree in Mechanical Engineering from Semnan University, Iran. He followed Mechanical Engineering to achieve MSc degree from Imam Hosein university, Tehran, Iran in 2011. He was working in Iran Nanotechnology Initiative Council (INIC) between 2008 to 2013 in Public Awareness department. In November 2013, he moved to the Netherlands to return to the academic world and started his PhD at Transport Engineering and Logistics Section in Mechanical, Maritime and Materials Engineering Faculty, Delft University of Technology. His research interest includes Structural Health Monitoring, Lifetime Prediction, and Maintenance Planning. In 2018, he joined YesDelft tech incubator to turn his Railway Wheel Monitoring Technology into business by running a StartUp.

E-mail: alemi.ar@gmail.com